

Institut de Physique de l'Université de Neuchâtel (Suisse)



Photoemission from transition metal dichalcogenides

Quasi-two dimensional systems with charge density waves

Thèse

Présentée à la Faculté des Sciences
de l'Université de Neuchâtel

Pour l'obtention du grade de docteur ès sciences

Par

Florian Clerc

Soutenue le 30 mai 2006

En présence du directeur de thèse
Prof. Philipp Aebi

et des rapporteurs

Dr. Luc Patthey
Prof. Hans Beck et Prof. Daniel Malterre

Neuchâtel, 2006

IMPRIMATUR POUR LA THESE

**Photoemission from transition metal
dichalcogenides**

Quasi-two dimensional systems with
charge density waves

Florian CLERC

UNIVERSITE DE NEUCHATEL

FACULTE DES SCIENCES

La Faculté des sciences de l'Université de Neuchâtel,
sur le rapport des membres du jury

MM. P. Aebi (directeur de thèse),
H. Beck, D. Malterre (Nancy, F)
et L. Patthey (PSI, Villigen)

autorise l'impression de la présente thèse.

Neuchâtel, le 25 juillet 2006

Le doyen :

J.-P. Derendinger

Contents

Preface	7
List of abbreviations	8
1 Introduction	9
2 ARPES - spectral function - self-energy	11
2.1 Introduction	11
2.2 ARPES method and theory	12
2.3 Many body concepts used in ARPES	16
2.3.1 Introduction to Green's functions	16
2.3.2 A simple example	17
2.3.3 The Lehmann representation	18
2.3.4 The self-energy Σ	19
2.4 Simulated example of the extraction of Σ from ARPES data	20
References for chapter 2	23
3 TMDCs quasi-two dimensional systems	25
3.1 Introduction	25
3.2 Fermi surface of layered compounds and bulk charge density wave systems	26
3.2.1 Introduction	26
3.2.2 Aspects of photoemission	29
3.2.3 Experiments and calculations	30
3.2.4 Results and discussion	30
3.2.5 Conclusion and outlook	39
References for chapter 3	41
4 On the search for the CDW origin in $1T$-TaS₂	45
4.1 Introduction	45
4.2 CDW theory in a one-dimensional metal	46
4.2.1 Peierls transition and energy balance	46
4.2.2 Linear response theory and generalized susceptibility	48
4.2.3 Electron-phonon interaction and Kohn anomaly	50
4.3 CDW in $1T$ -TaS ₂ : An angle-resolved photoemission study	54
4.4 Lattice-distortion enhanced electron-phonon coupling and Fermi surface nesting in $1T$ -TaS ₂	58
4.4.1 Introduction	58

4.4.2	Experimental and computational details	59
4.4.3	Results and discussion	60
4.4.4	Summary and conclusion	67
4.5	Complement	69
4.5.1	Coexisting periodicities in $1T$ -TaS ₂	69
4.5.2	Polaron	72
4.6	Summary	76
	References for chapter 4	77
5	$1T$-TiSe₂, an excitonic insulator?	81
5.1	Introduction	81
5.2	Excitons and spectral function	82
5.2.1	The electron-hole system	82
5.2.2	Exciton physics	84
5.2.3	Condensate phase	85
5.2.4	Fluctuating excitons	87
5.3	Experimental results and confrontation with the exciton model	91
5.4	Summary	94
	References for chapter 5	96
6	Spin-orbit coupling in $1T$-TaS₂ and $1T$-TaSe₂, a group theory study	97
6.1	Introduction	97
6.2	Spin-orbit splitting in the valence bands of $1T$ -TaS ₂ and $1T$ -TaSe ₂	98
6.2.1	Introduction	98
6.2.2	Experiment and calculation	99
6.2.3	Results and discussion	99
6.2.4	Conclusion	104
6.3	Complement	105
	References for chapter 6	107
7	Conclusion	109
	Acknowledgements	111
	Curriculum vitae	113

Preface

This thesis is based on research carried out at the *Institut de Physique, Université de Neuchâtel, Neuchâtel, Switzerland* during the period 2002 - 2006. It consists of seven chapters: an introduction, a presentation of the photoemission process, an introduction of transition metal dichalcogenides, two chapters with a discussion on the driving forces for charge density waves formation in quasi-2D systems, an example of band mapping using synchrotron light and a conclusion.

The chapters 3, 4 and 6 contain several sections with articles published (or submitted) during this work. Therefore, each section stands completely on its own with an abstract, introduction, and an experimental section. This allows the reader to study these sections independently and in any order, with no loss of continuity, depending on the personal interest. For sequential reading, this leads to some redundancy concerning the introductions and the descriptions of experimental procedures. These parts may therefore be skipped.

The articles included in this thesis are:

Fermi surface of layered compounds and bulk charge density wave systems F. Clerc, C. Battaglia, C. Monney, H. Berger, L. Despont, M. G. Garnier and P. Aebi <i>Submitted to J. Phys. C (2006)</i>	26
Charge density waves in 1T-TaS ₂ : An angle-resolved photoemission study F. Clerc, M. Bovet, H. Berger, L. Despont, C. Koitzsch, M. G. Garnier and P. Aebi <i>Physica B</i> 351 , 245-249 (2004)	54
Lattice-distortion enhanced electron-phonon coupling and Fermi surface nesting in 1T-TaS ₂ F. Clerc, C. Battaglia, M. Bovet, L. Despont, c. Monney, H. Cercellier, M. G. Garnier, H. Berger, L. Forró and P. Aebi <i>Submitted to Phys. Rev. B (2006)</i>	58
Spin-orbit splitting in the valence bands of 1T-TaS ₂ and 1T-TaSe ₂ F. Clerc, M. Bovet, H. Berger, L. Despont, C. Koitzsch, O. Gallus, L. Patthey, M. Shi, J. Krempasky, M. G. Garnier and P. Aebi <i>J. Phys. C</i> 16 , 3271-3278 (2004)	98

List of acronyms

1D,2D,3D	one-, two-, three-dimensional	XPD	x-ray photoelectron diffraction
ADC	angular distribution curves	XPS	x-ray photoelectron spectroscopy
APW	augmented plane wave		
ARPES	angle-resolved photoelectron spectroscopy		
BZ	Brillouin zone		
C	commensurate		
CB	conduction band		
CDW	charge density waves		
DFPT	density functional perturbation theory		
DFT	density functional theory		
DOS	density of states		
EDC	energy distribution curves		
E_F	Fermi level		
FL	Fermi liquid		
FLAPW	full potential linearized augmented plane wave		
FS	Fermi surface		
FSM	Fermi surface mapping		
GGA	generalized gradient approximation		
HTCs	high temperature superconductors		
IC	incommensurate		
IPES	inverse photoemission spectroscopy		
LDA	local density approximation		
LEED	low energy electron diffraction		
LHB	lower Hubbard band		
MDC	momentum distribution curves		
PES	photoemission spectroscopy		
QC	quasi-commensurate		
QP	quasiparticle		
SBZ	surface Brillouin zone		
SO	spin-orbit		
SOC	spin-orbit coupling		
STM	scanning tunneling microscope		
TMDCs	transition metal dichalcogenides		
UV	ultra-violet		
VB	valence band		

Chapter 1

Introduction

The study of the electronic structure is a central topic in material science. Most properties of solids are directly related to the manner how electrons occupy the disponible states and how they interact with the various degrees of freedom. One of the first successes of the quantum theory of solid was the prediction of the electronic band structure, which, in the non-interacting electron theory is only due to the periodic lattice structure of the crystal. This band picture allowed the classification of crystals into metals, semiconductors and insulators depending on the occupation of the highest filled band. This major step towards the comprehension of materials was the precursor of the today widespread use of semiconductors and other novel materials in the nowadays life.

Although the numerous successes of band theory, many properties of transition metal oxides are in total disagreement with predictions of band structure calculations. For example, some of these oxydes, although having a partially filled d-band, present poor conductor or even insulator behaviour. In 1937, Mott and Peierls pointed out for the first time the importance of electron-electron correlations and marked the beginning of the rich and still very actual field of strongly correlated electrons. A conventional treatment of systems with interacting electrons is the Landau's Fermi liquid theory, where a one to one correspondence between excitations of the interacting and the non-interacting system (due to the adiabatic switching on of the interactions) allows to describe the Fermi liquid material only through a renormalization of parameters such as the electron mass or the spectral weight of the quasiparticle. However the Fermi liquid description fails when dimensionality is reduced to 1D and new theoretical models are therefore demanded.

Low-dimensional systems and particularly quasi-2D compounds have gained strong interest since the discovery, in the 1986 of high temperature superconductors (HTCs). These materials, having a strong potential for promising applications, present new challenges to the solid state physicists. Their extraordinary properties are related to complicated and still not fully understood physics, where complex correlations play a central role. The transition metal dichalcogenides (TMDCs), which are studied in this thesis, are layered materials with quasi-2D character presenting some similarities with HTCs and being therefore alternative materials to study the correlations induced behaviour.

Angle resolved photoemission spectroscopy (ARPES) is the most suitable tool to investigate electronic structure and has early contributed to give a physical meaning to the theoretical concept of band structure. Then, thanks to various technological developments, that have led to a huge improvement of both the energy and angular resolutions of modern analysers, ARPES has been a major experimental probe of the electronic excitations in the vicinity of the Fermi level. In 2D case, the identification of the ARPES signal with the spectral function provides insight into many-body theory concepts such as the single particle self-energy, which reflects the interactions of the systems.

The aim of the present thesis is to take advantage of the ARPES facilities to investigate a series of TMDCs presenting instabilities due to the occurrence of charge density waves (CDW). Although

the mechanism of CDW formation in 1D systems is since long well explained thanks to the Peierls pioneering work, CDW in quasi-2D compounds still present, in our sense, incompatibilities with the 1D Peierls scenario.

Chapter 2 of this thesis is devoted to the basic principle of photoemission process with particular insight into its ability to give direct access to the spectral function. Many-body concepts will also be presented in this chapter, whose aim is not to give a complete and rigorous development of this theory, but rather to present the useful tools which are at our disposal to compare models with ARPES measurements. Chapter 3 stands as an introduction to the properties of some TMDCs, as well as to their problematic structural instabilities. Chapter 4 and 5 are devoted to a more detailed investigation of the origin of CDW in 1T-type TMDCs, namely the 1*T*-TaS₂ (chapter 4) and 1*T*-TiSe₂ (chapter 5). In chapter 4, after a description of the theory of Peierls instability in 1D systems, we generalize this mechanism to 2D case and try to demonstrate the existence of a more complex scenario for the occurrence of CDW in the 1*T*-TaS₂. Although the generally believed Fermi surface nesting cannot be ruled out as the origin of CDW in the 1*T*-TaS₂, we find unusual spectral features in ARPES data indicating the non-negligible influence of complex correlations. CDW in the 1*T*-TiSe₂ is presented in chapter 5. The mechanism of the CDW formation in this compound is generally accepted to be more exotic. We focus our attention to the so-called excitonic scenario and detail the theory of excitons formation to determine what traces would reflect the existence of excitons, and compare this with our ARPES data. Finally, chapter 6 is an example of the power of ARPES as a band structure probe. By means of synchrotron light, we investigate the dispersion of the highest occupied band of the isostructural 1*T*-TaS₂ and 1*T*-TaSe₂ along a direction perpendicular to the layers. Comparison with band calculations allows us to identify a spin-orbit coupling, this assumption being further confirmed by an analysis based on group theory.

Chapter 2

ARPES - spectral function - self-energy

2.1 Introduction

Angle-resolved photoemission spectroscopy is based on the photoelectric effect that was originally observed in 1887 by Hertz [1]. In 1905 Einstein brought the theoretical explanation of this phenomenon as a manifestation of the quantum nature of light [2]. Since then, ARPES has emerged as a leading tool to investigate the electronic structure of materials. Its great success is due to the unique momentum resolved information it provides which allows the direct measurements of the electronic states dispersion in a crystal [3]. This momentum selectivity has opened the opportunity to obtain physical quantities related to electronic structure of solid such as Fermi surface [4], superconducting gap [5–7] or pseudogap [8–10].

ARPES has also largely contributed to the validation of various theoretical models or concepts. As under certain assumptions the photocurrent measured by ARPES is directly related to the spectral function of the studied material, ARPES line shapes can provide insight into the fundamental interactions taking place inside a many-body system. The first success of ARPES as probe of many body interaction on an electron in a solid was certainly the excellent agreement found by Claessen et al. [11] between the ARPES weight distribution measured on $1T$ - TiTe_2 and the theoretical line shape derived from Fermi liquid behaviour. Since then, this ARPES ability to reveal the nature of interacting electrons system has been widely used [12]. Recent improvements in the energy and momentum resolution of modern ARPES analysers permit to reveal fine details of the photoemission line shapes and thus make the researchers going further into analysis by refining their models with use of modern many body theory techniques. Most of these developments took place simultaneously with a growing interest for strongly correlated materials such as high temperature superconductors, colossal magnetic resistance compounds or low dimensional materials. The new possibilities of ARPES allow a description of unusual spectral features in low binding energy region in term of strong electron-phonon, electron-electron or electron-collective modes coupling [13–15]. Such systematic studies seem to be very promising for understanding the physical phenomena taking place in complex materials.

In this chapter we present the basic description of the ARPES method, the goal being to understand what ARPES measures and particularly under which assumptions it can be related to the single-particle spectral function. For a more complete and rigorous discussion of ARPES we refer the reader to the rich literature existing on the subject [16–18]. As ARPES has evolved from a basic band mapping technique to a sophisticated many body spectroscopy, we present in the second part basic notions of many body theory tools such as Green functions, spectral functions and self-energy. Then we conclude with a simulation illustrating a method commonly used to extract the self-energy from ARPES line shapes.

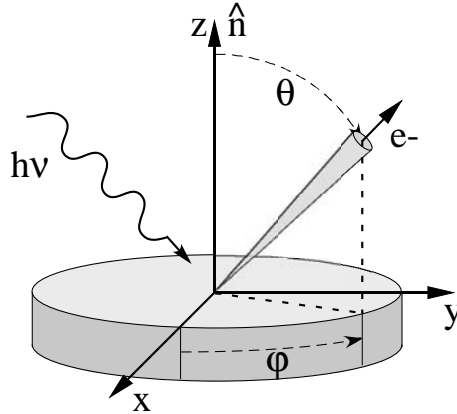


Figure 2.1: Scheme of a photoemission experiment. Light with energy $h\nu$ and polarization vector \mathbf{A} illuminates the sample. Due to the photoelectric effect electrons are ejected and can be captured in the detector, and analysed as a function of their kinetic energy and their polar and azimuthal angles θ, φ , respectively.

2.2 ARPES method and theory

The typical geometry of an ARPES experiment is sketched in Fig. 2.1. A beam of monochromatic photons of energy $h\nu$ hits the sample whose electrons can absorb photons and thus be excited under strict momentum conservation into previously unoccupied higher energy final states. If their final state energy is higher than the potential barrier, they can escape in the vacuum and be detected in the photoelectron spectrometer as a function of their kinetic energy, angle of emission and sometimes their spin. The energy of the incoming light is among the parameters which can be varied in the experiment. One usually distinguishes between two energy regimes, the soft x-rays regime where the photon energy lies typically between 50 eV and 2000 eV and the ultra-violet (UV) regime where the photon energy is comprised between 5 eV and 50 eV. Light in the UV energy range is generally supplied either by gas-discharge lamp or a synchrotron beamline. In some instruments it is also possible to rotate the polarization vector of the light which allows to play with selection rules and thus with transition matrix elements.*

To help in the interpretation of the photoemission experiment, the semiclassical three step model is commonly used [19,20]. In this approach the photoemission event is broken up into three distinct and independent processes, as sketched in Fig. 2.2:

- (1) The optical transition of the electron between an occupied initial state to an unoccupied final state of the crystal (intrinsic effects)
- (2) The travel of the photoelectron through the sample to the surface
- (3) The escape of the photoelectron into the vacuum after transmission through the surface potential barrier.

(1) Thus the first step to derive a formal description of the photoemission process is to calculate the transition probability ω_{if} for the optical transition. This excitation takes place between the N -electron ground state Ψ_i^N with energy E_i^N and one of the possible N -electron final states Ψ_f^N of energy E_f^N . The optical transition due to the absorption of a photon of energy $h\nu$ in a crystal can be described by the Fermi's golden rule:

$$\omega_{if} = \frac{2\pi}{\hbar} |\langle \Psi_f^N | H_{int} | \Psi_i^N \rangle|^2 \delta(E_f^N - E_i^N - h\nu) \delta(\mathbf{k}_f - \mathbf{k}_i - \mathbf{G}) \quad (2.1)$$

H_{int} is the Hamiltonian representing the interaction of the electron with the electromagnetic

*A last parameter which is largely used to investigate materials with ARPES is evidently the temperature of the sample.

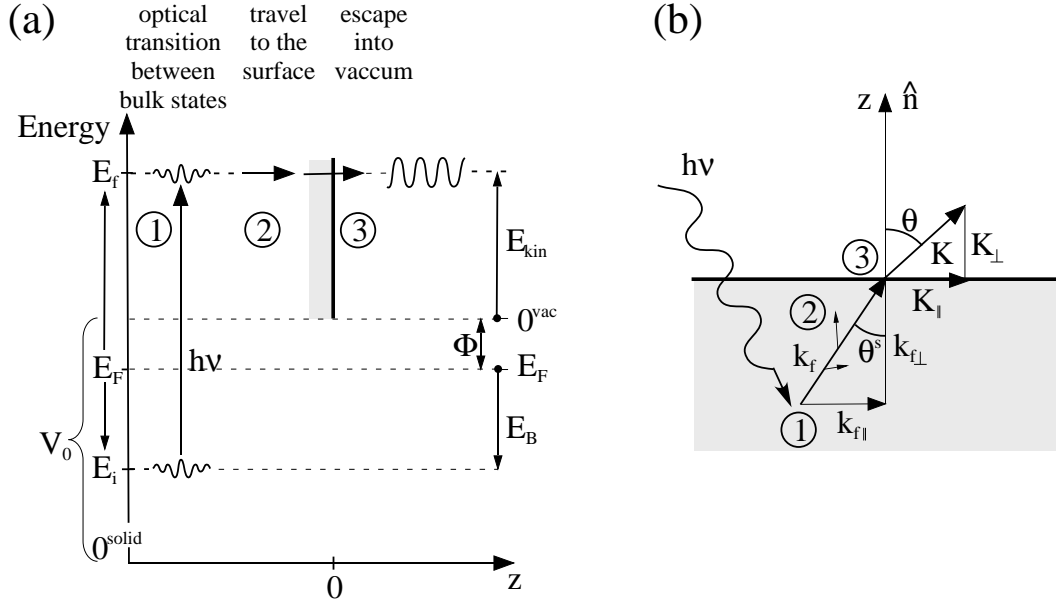


Figure 2.2: Illustration of the three steps model of the photoemission process (from ref. [17]). The three steps are: (1) the optical excitation, (2) the travel to the surface and (3) the transmission through the surface. (a) Energy level diagram for one-electron states. Two energy scales are depicted, the energy levels referenced to the solid on the left and the ones referenced to the vacuum potential on the right. The shift between the zero of these two energy scales is given by the crystal potential V_0 . (b) Momentum vectors with refraction of the photoelectron at the surface of the solid.

field of the incoming light. It can be treated as a perturbation and has the following form:

$$H_{int} = \frac{e}{2mc} (\mathbf{A}(\mathbf{r}, t) \cdot \mathbf{p} + \mathbf{p} \cdot \mathbf{A}(\mathbf{r}, t)) \quad (2.2)$$

where \mathbf{A} is the electromagnetic vector potential and \mathbf{p} the electronic momentum operator. In case where the wavelength of the spatial variation of \mathbf{A} is large compared to the atomic displacement (i.e. $\nabla \cdot \mathbf{A} \approx 0$) H_{int} simplifies to $H_{int} = \frac{e}{2mc} \mathbf{A} \cdot \mathbf{p}$. This last assumption is reasonably correct for ultra-violet light and in the bulk of the solid, but no more near the surface because of the rapid change in the dielectric response. Therefore H_{int} has to be treated more correctly at the surface [21]. In (2.1) the delta functions ensure the energy and momentum conservation during the photoexcitation process (the photon momentum is neglected). \mathbf{k}_f and \mathbf{k}_i are the momentum of the photoelectron, and of the electron before the absorption of a photon, respectively, and \mathbf{G} corresponds to a reciprocal lattice vector. We note that in an extended zone scheme (scheme which repeats the Brillouin zone periodically in space) the momentum in the optical transition is conserved modulo a reciprocal lattice vector. This additional source of momentum is indeed essential to allow transitions under strict momentum conservation.

In order to simplify the expression (2.1) we make use of a crucial assumption of the photoemission theory, namely the sudden approximation. It assumes that the photoelectron $\phi_f^{\mathbf{k}}$ is instantaneously decoupled from the remaining $(N-1)$ -electrons system after the excitation, meaning that there is no interaction between the photoelectron and the photohole. This assumption allows the factorization of the final state into a photoelectron and a $(N-1)$ -electron system left in one of the possible excited states m :

$$\Psi_f^N = c_{\mathbf{k}}^+ \Psi_m^{N-1} \quad (2.3)$$

where $c_{\mathbf{k}}^+$ is the creation operator for the photoelectron state $\phi_f^{\mathbf{k}}$. The faster the photoelectron escapes from the excitation region, the better the sudden approximation is. With use of this

factorization of the final state the transition matrix element in (2.1) becomes

$$\langle \Psi_f^N | H_{int} | \Psi_i^N \rangle = \langle \phi_f^{\mathbf{k}} | H_{int} | \phi_i^{\mathbf{k}} \rangle \langle \Psi_m^{N-1} | c_{\mathbf{k}} | \Psi_i^N \rangle \quad (2.4)$$

where $\phi_i^{\mathbf{k}}$ represents the wavefunction of the electron before excitation by the optical process. Therefore $M_{if} = \langle \phi_f^{\mathbf{k}} | H_{int} | \phi_i^{\mathbf{k}} \rangle$ is a one-electron matrix element and $\langle \Psi_m^{N-1} | c_{\mathbf{k}} | \Psi_i^N \rangle$ represents a (N-1)-electron overlap integral. As the remaining (N-1)-electron system relaxes after the excitation of an electron from orbital $\phi_i^{\mathbf{k}}$ we have to include the many possible relaxed states Ψ_m^{N-1} of energy E_m^{N-1} . Thus at this stage the total photocurrent can be written as:

$$I \sim \sum_{if} | M_{if} |^2 \sum_m \langle \Psi_m^{N-1} | c_{\mathbf{k}} | \Psi_i^N \rangle|^2 \delta(E_{kin}^{solid} + E_m^{N-1} - E_i^N - h\nu) \delta(\mathbf{k}_f - \mathbf{k}_i - \mathbf{G}) \quad (2.5)$$

Here the final energy is decomposed into the kinetic energy of the photoelectron in the solid E_{kin}^{solid} plus the energy of the system left behind the photoelectron E_m^{N-1} . A further simplification is possible by considering the independent particle point of view and thus using the Hartree-Fock formalism where the many electron wavefunction is represented by a single Slater determinant. The (N-1)-electron overlap integral of (2.5) becomes $\sum_m | a_m |^2 = \sum_m | \langle \Psi_m^{N-1} | \Psi_i^{N-1} \rangle |^2$. It represents the probability that the removal of an electron from the orbital $\phi_i^{\mathbf{k}}$ of the N-electrons ground state leaves the (N-1)-particle system in the excited state m. For a weakly correlated system $\Psi_m^{N-1} \simeq \Psi_i^{N-1}$, therefore $| a_m |^2$ is unity for a particular m and zero otherwise, which is reflected in the photoemission spectrum by a single peak. On the contrary for strongly correlated systems many of the $| a_m |^2$ are non zero and therefore the ARPES spectrum shows a main line followed by several satellites according to the number of excited states m created in the process.

(2) During its travel to the surface the electrons suffer scattering which limits the number of electrons reaching the surface. These scattering events lead to an inelastic background in the spectrum which can be subtracted or even ignored.

(3) The last step displayed in Fig. 2.2 is the passage of the photoelectron through the surface. The condition that a photoelectron has to satisfy to escape into the vacuum is that the component of its wavevector perpendicular to the surface has to be large enough, $\frac{\hbar^2}{2m} k_{f\perp}^2 \geq V_0$.

The presence of a surface potential barrier induces a fundamental difference between the momentum components parallel and perpendicular to the surface. Indeed, while the wavevector component parallel to the surface is conserved modulo a surface reciprocal lattice vector, $\mathbf{K}_{\parallel} = \mathbf{k}_{f\parallel} + \mathbf{G}_{\parallel}$, the conservation of the perpendicular component is broken. Regarding energy, it is conserved during the process of electron transmission through the surface.

All this put together leads to the following expression for the photocurrent calculated via the three step model:

$$\begin{aligned} I(\mathbf{K}, E) &= \sum_{if} | M_{if} |^2 \sum_m \langle \Psi_m^{N-1} | c_{\mathbf{k}} | \Psi_i^N \rangle|^2 \\ &\quad \times \delta(E_{kin}^{solid} + E_m^{N-1} - E_i^N - h\nu) \delta(\mathbf{k}_f - \mathbf{k}_i - \mathbf{G}) \\ &\quad \times \delta(E - (E_f - \phi)) \delta(\mathbf{K}_{\parallel} - \mathbf{k}_{\parallel} - \mathbf{G}_{\parallel}) \end{aligned} \quad (2.6)$$

The two first delta functions describe energy and momentum conservation for the optical transition while the two last ones describe energy and momentum conservation during the surface transmission process. E_f is the final energy of the photoelectron with respect to the Fermi energy (see Fig. 2.2 (a)).

Under special conditions or a priori assumption, expression (2.6) allows the determination of the initial state band dispersion. Indeed with the knowledge of the kinetic energy of the electron outside the sample E_{kin}^{vac} , the emission angles (ϑ , φ) and the photon energy, it is possible to calculate

the magnitude of the parallel component of the wavevector $\mathbf{k}_{i\parallel}$ and the energy E_i of the initial state

$$\begin{aligned} E_i &= E_{kin}^{vac} - (h\nu - \phi) \\ k_{i\parallel} &= \sqrt{\frac{2m}{\hbar^2}} \sin\vartheta \end{aligned} \quad (2.7)$$

For a complete band mapping one still needs to determine $\mathbf{k}_{i\perp}$, which is often not a trivial matter. To overcome this problem, the most usual and economic approach is to make an assumption about the final state. The simplest way is to assume a free electron final state, which gives $k_{i\perp} = \sqrt{\frac{2mE_{kin}^{vac} \cos^2\vartheta_{vac} - V_0}{\hbar^2}}$. A more accurate method is to work with the final state derived from band calculation [22]. Finally, more elaborate methods allow absolute determination of the crystal momentum without any *a priori* assumption but with the drawback of being more time consuming and requiring many experimental spectra to determine a single position in k-space [23–25].

Fortunately, for the case of low-dimensional materials like the ones studied in this thesis, the $k_{i\perp}$ dispersion can be neglected and only $\mathbf{k}_{i\parallel}$ has to be determined. This is reflected by the large amount of ARPES works performed on low-dimensional systems [26].

Unfortunately there are failures in the three step approach of photoemission. First let us consider the idealized case where electrons possess an infinite mean free path and thus do not feel the presence of the surface. In such a situation the photoemission process involves a transition between two perfect Bloch states and this situation is correctly represented by the three steps model. But in reality the electrons interact strongly with their environment (electron-electron, electron-phonon, electron-plasmon scattering). Therefore electrons have a finite mean free path and the photoemission experiment becomes sensible to the surface. The initial and final electronic states are only Bloch states in the plane parallel to the surface. The price to pay to keep working with 3D Bloch states which are not stationary states of the problem anymore is to include an imaginary part to the component of the wavevector perpendicular to the surface of the crystal. This leads to a smearing of the momentum conservation and loss of the k_{\perp} conservation. With these considerations the photocurrent is now expressed by:

$$\begin{aligned} I(\mathbf{K}, E) &= \sum_{if} |M_{if}|^2 \sum_m \langle \Psi_m^{N-1} | c_{\mathbf{k}} | \Psi_i^N \rangle|^2 \\ &\times \delta(E_{kin}^{solid} + E_m^{N-1} - E_i^N - h\nu) \delta(E - E_f) \\ &\times \frac{(k_{i\perp}^I - k_{f\perp}^I)}{(k_{i\perp}^R - k_{f\perp}^R)^2 + (k_{i\perp}^I - k_{f\perp}^I)^2} \delta(\mathbf{K}_{\parallel} - \mathbf{k}_{\parallel} - \mathbf{G}_{\parallel}) \end{aligned} \quad (2.8)$$

Although the three step model is useful to give a comprehensive view of the photoemission process, it does not treat the problem correctly from the point of view of quantum mechanics.

A correct description of the photoemission process is given by the one-step model (Fig. 2.3) which treats photoemission as a single coherent process [27, 28] with the correct boundary conditions, i.e by considering a semi-infinite crystal. The photocurrent is again given by Fermi's golden rule but now the optical transition takes place between two inverse LEED states.

In this approach the k_{\perp} is conceptually not a good quantum number, as the stationary states of the problem are written as linear combinations of 3D waves with various k_{\perp} (but same k_{\parallel}). It is not necessary to artificially add an imaginary part to the wavevector as in the three step model. However to account for the many body interactions which make finite the photoelectron mean free path as well the photohole life time, the energy now possesses an imaginary part. This corresponds to assuming a complex wavevector $\mathbf{k} = \mathbf{k}^R + i\mathbf{k}^I$. It is important to note the fundamental difference between the two approaches: in the one-step model the fact that k_{\perp} is

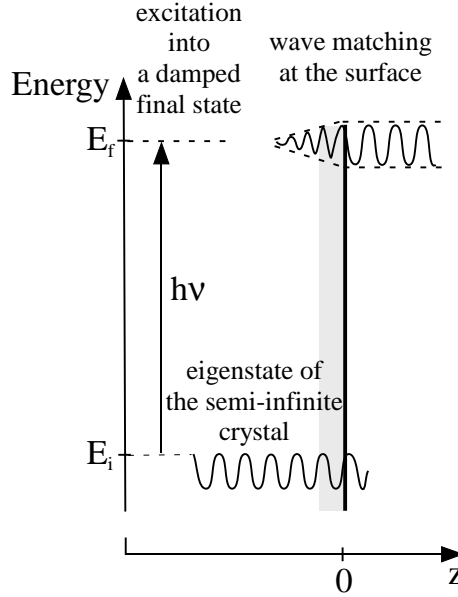


Figure 2.3: Illustration of the one step model of the photoemission process (from ref. [17]).

not a good quantum number to describe photoemission follows naturally from the use of correct boundary conditions, and the addition of an imaginary part to the momentum vector of the initial and final states is only a consequence of many body interactions. In the three step model, the addition of an imaginary part to the perpendicular component of the wavevector of the initial and final state is a consequence of both, k_{\perp} not being a good quantum number, and many body effects. This is not fully general as electrons undergo also scattering in plane, i.e. parallel to the surface.

2.3 Many body concepts used in ARPES

Thanks to the improvement in momentum and energy resolutions, photoemission has become sensitive to the influence of many body interactions [29]. In this context we introduce here some notions of many body theory. The aim is not to give a complete and rigorous description of this theory but to define and give a feeling of some concepts used in the following chapters of this thesis. For further reading the reader is referred to the large existing literature [30–33]

2.3.1 Introduction to Green's functions

Among the methods used to treat interacting particle systems the Green's function formalism, developed within quantum field theory, is certainly the most successful in the photoemission community. Indeed this method is not only extremely helpful for solving certain many body problems but also contains all the relevant information of the system, especially when dealing with the spectral function measured by ARPES.

To introduce Green's function, let us consider a many body system described by an Hamiltonian H where $|\Psi_0\rangle$ is the unknown exact ground state of N -particles. At zero temperature the time ordered single particle Green's function is defined as:

$$G(\mathbf{r}_1, t_1; \mathbf{r}_2, t_2) = -i \langle \Psi_0 | T \Psi(\mathbf{r}_1, t_1) \Psi^+(\mathbf{r}_2, t_2) | \Psi_0 \rangle \quad (2.9)$$

T denotes the time ordering operator defined as:

$$T \Psi(\mathbf{r}_1, t_1) \Psi^+(\mathbf{r}_2, t_2) = \begin{cases} \Psi(\mathbf{r}_1, t_1) \Psi^+(\mathbf{r}_2, t_2) & t_1 > t_2 \\ \pm \Psi^+(\mathbf{r}_2, t_2) \Psi(\mathbf{r}_1, t_1) & t_1 < t_2 \end{cases} \quad (2.10)$$

where the plus and minus sign stands for bosons and fermions, respectively. Ψ and Ψ^+ are the second quantized annihilation and creation field operators which can be expressed either in a position representation or in the basis of single particle states:

$$\Psi(\mathbf{r}, t) = \sum_{\mathbf{k}} c_{\mathbf{k}} \phi_{\mathbf{k}}(\mathbf{r}, t) \quad (2.11)$$

$\phi_{\mathbf{k}}$ are first quantized wave single particle wave functions and $c_{\mathbf{k}}$ are destruction operators of a particle with quantum number \mathbf{k} . If the Hamiltonian H is time independent and the system is translationally invariant, $G(\mathbf{r}_1, t_1; \mathbf{r}_2, t_2)$ depends only on $t = t_1 - t_2$ and $\mathbf{r} = \mathbf{r}_1 - \mathbf{r}_2$. So we can introduce the position Fourier transform which is:

$$\begin{aligned} G(\mathbf{k}, t) &= \ll c_{\mathbf{k}}(t); c_{\mathbf{k}}^{\dagger}(0) \gg = \int d^3\mathbf{r} e^{-i\mathbf{k}\mathbf{r}} G(\mathbf{r}, t) \\ &= -i \langle \Psi_0 | T c_{\mathbf{k}}(t) c_{\mathbf{k}}^{\dagger}(0) | \Psi_0 \rangle \end{aligned} \quad (2.12)$$

where for clarity we introduce the new notation with $\ll \gg$ to represent Green's functions. With this last expression the Green's function can be interpreted as the probability amplitude that an electron added to the system in a Bloch state of momentum number \mathbf{k} is found at time $t > 0$ in the same state. For that reason Green's functions are also called propagators. We note that if the electron suffers interaction during the time t , some amplitude will be lost and thus provide information on the many body physics.

2.3.2 A simple example

A simple example with free fermions illustrates well the possibility of deriving an expression for a Green's function. Evidently it is not necessary to use this method for this exactly solvable case but it is a didactic first approach of the Green's function formalism. The Hamiltonian for a free fermions system may be written in second quantification as

$$H_0 = \sum_k (\epsilon_k - \mu) c_k^{\dagger} c_k \quad (2.13)$$

with $\epsilon_k = \frac{\hbar^2 k^2}{2m}$ and μ the chemical potential. We make use of the equation of motion to find the analytical form of the Green's function of a free fermions system. The time evolution of a Green's function is found by differentiating the expression (2.12):

$$\begin{aligned} i \frac{\partial}{\partial t} G(k, t) &= i \frac{\partial}{\partial t} \ll c_k(t); c_k^{\dagger}(0) \gg \\ &= \delta(t) \langle \Psi_0 | \{c_k(t) c_k^{\dagger}(0)\} | \Psi_0 \rangle + \langle \Psi_0 | T \frac{\partial}{\partial t} c_k(t) c_k^{\dagger}(0) | \Psi_0 \rangle \end{aligned} \quad (2.14)$$

With use of the anticommutation rule for fermions and by noting that the Heisenberg equation of motion for the operator c_k is $\frac{\partial c_k(t)}{\partial t} = [c_k(t), H_0] = -(\epsilon_k - \mu) c_k(t)$, (2.14) can be written :

$$i \frac{\partial}{\partial t} G(k, t) = \delta(t) + (\epsilon_k - \mu) G(k, t) \quad (2.15)$$

and therefore :

$$(i \frac{\partial}{\partial t} - (\epsilon_k - \mu)) G(k, t) = \delta(t) \quad (2.16)$$

So we refind the mathematical sense of Green's function as a method for solving differential equations. (2.16) can be solved by Fourier transformation. This leads to an expression for the so called unperturbed Green's function [†]

$$G^0(k, \omega) = \ll c_k; c_k^+ \gg_{\omega}^0 = \int dt G^0(k, t) e^{i\omega t} = \frac{1}{\omega - (\epsilon_k - \mu) + i\delta_k}. \quad (2.17)$$

G has a pole at $\omega = (\epsilon_k - \mu) - i\delta_k$ which corresponds to the energy of the quasiparticle, i.e. the elementary excitation spectrum. This method to derive Green's function is very convenient for this simple example because the time dependence of the operator c_k is well known. It is not always the case and finding information about the dynamics of the many-particle system can be a very hard task.

2.3.3 The Lehmann representation

Let us introduce now the Lehmann representation of the Green's function, which will be useful to introduce concepts related to ARPES such as spectral function or advanced and retarded Green's function.

To obtain the Lehmann representation in frequency space one starts with (2.12) and uses the completeness relation of the exact eigenstate $|\Psi_n^N\rangle$ of the Hamiltonian, $\mathcal{I} = \sum_{n,N} |\Psi_n^N\rangle\langle\Psi_n^N|$. After introducing this identity in (2.12) and a subsequent Fourier transformation we find for the Lehmann representation of the Green's function:

$$\begin{aligned} G(\mathbf{k}, \omega) &= G^+(\mathbf{k}, \omega) + G^-(\mathbf{k}, \omega) \\ &= \int_0^{\infty} d\omega' \left(\frac{A^+(\mathbf{k}, \omega')}{\omega - \omega' - \mu + i\delta} + \frac{A^-(\mathbf{k}, \omega')}{\omega + \omega' - \mu - i\delta} \right). \end{aligned} \quad (2.18)$$

G^+ and G^- are the one electron addition and removal Green's functions. The one particle spectral function is defined as $A = A^+ + A^-$ with

$$A^+(\mathbf{k}, \omega) = \sum_n |\langle \Psi_n^{N+1} | c_{\mathbf{k}}^+ | \Psi_0 \rangle|^2 \delta(\omega - E_n^{N+1} + E_0^N) \quad (2.19)$$

and

$$A^-(\mathbf{k}, \omega) = \sum_n |\langle \Psi_n^{N-1} | c_{\mathbf{k}} | \Psi_0 \rangle|^2 \delta(\omega - E_n^{N-1} + E_0^N). \quad (2.20)$$

Note that A^- and A^+ define the one electron removal and addition spectra which can be probed by means of direct and inverse photoemission, respectively [‡]. Thus the ARPES intensity can be written as :

$$I(\mathbf{k}, \omega) = I_0 f(\omega) A(\mathbf{k}, \omega) \quad (2.21)$$

where I_0 contains the transition matrix elements and $f(\omega)$ is the Fermi function which ensures transition only from the occupied states. With use of the following identity:

$$\lim_{\delta \rightarrow 0} \int dx \frac{f(x)}{x \pm i\delta} = \mathcal{P} \int dx \frac{f(x)}{x} \mp \pi i \int dx f(x) \delta(x)$$

A is related to the Green function by

$$A = -\frac{1}{\pi} \text{Im} G^{\text{ret}} = \frac{1}{\pi} \text{Im} G^{\text{adv}}. \quad (2.22)$$

[†]Here a mathematical trick is used: to ensure that the time integral converges we add an infinitesimal quantity $\delta_k = \delta \text{sign}(\epsilon_k - \mu)$ and consider the Fourier transform of $e^{-\delta|t|} G(k, t)$.

[‡]For A^- it can be easily seen by comparison with the expression (2.6) derived for the photocurrent.

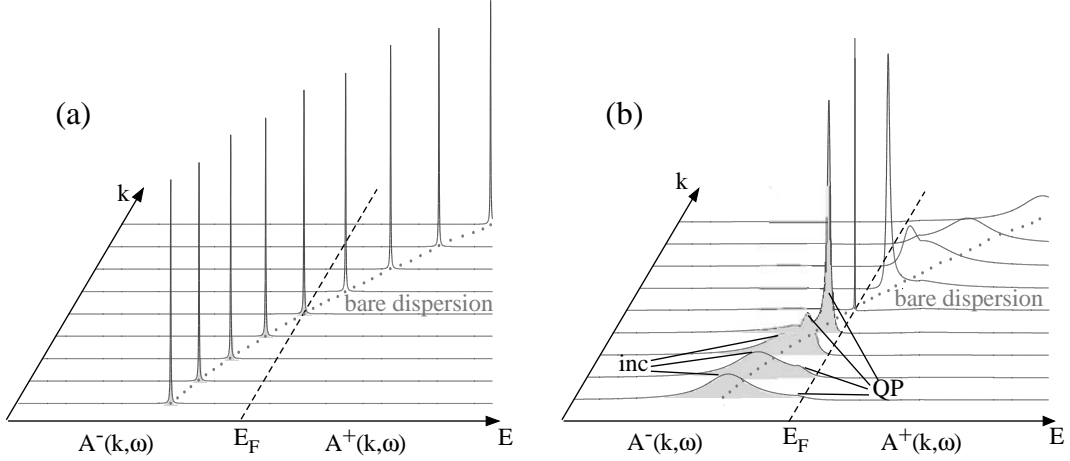


Figure 2.4: Illustration of the spectral function derived for the non-interacting electron case (a) and for the interacting one (b). (a) The spectrum consists of delta functions located at the bare energies. (b) The line shape reveals a complex structure composed of a quasiparticle peak and a broad incoherent part.

Here we have introduced the retarded and advanced Green's functions, G^{ret} and G^{adv} , which are the analytic continuations of G at $\omega = \mu$:

$$\begin{aligned} G^{ret}(\mathbf{k}, \omega) &= G^+(\mathbf{k}, \omega) + G^{-*}(\mathbf{k}, \omega) \\ &= \ll c_{\mathbf{k}}; c_{\mathbf{k}}^+ \gg_{\omega}^{ret} = \int dt e^{i\omega t} \int d^3\mathbf{r} e^{-i\mathbf{k}\mathbf{r}} G^{ret}(\mathbf{r}, t) \end{aligned} \quad (2.23)$$

and

$$\begin{aligned} G^{adv}(\mathbf{k}, \omega) &= G^{ret*}(\mathbf{k}, \omega) \\ &= \ll c_{\mathbf{k}}; c_{\mathbf{k}}^+ \gg_{\omega}^{adv} = \int dt e^{i\omega t} \int d^3\mathbf{r} e^{-i\mathbf{k}\mathbf{r}} G^{adv}(\mathbf{r}, t) \end{aligned} \quad (2.24)$$

where $G^{ret}(\mathbf{r}, t)$ and $G^{adv}(\mathbf{r}, t)$ are defined as

$$\begin{aligned} G^{ret}(\mathbf{r}_1, t_1; \mathbf{r}_2, t_2) &= -i\theta(t_1 - t_2) \langle \Psi_0 | \{ \Psi(\mathbf{r}_1, t_1) \Psi^+(\mathbf{r}_2, t_2) \} | \Psi_0 \rangle \\ G^{adv}(\mathbf{r}_1, t_1; \mathbf{r}_2, t_2) &= i\theta(t_2 - t_1) \langle \Psi_0 | \{ \Psi(\mathbf{r}_1, t_1) \Psi^+(\mathbf{r}_2, t_2) \} | \Psi_0 \rangle. \end{aligned} \quad (2.25)$$

2.3.4 The self-energy Σ

The utility of Green's functions is now apparent. Indeed, with knowledge of the analytical form of the Green's function of a given system, one can get its ARPES spectral shape (apart from matrix element effects). For example, the spectral function for the noninteracting Green's function derived previously (2.17) is $A^0(\mathbf{k}, \omega) = \frac{1}{\pi} \text{Im} G^{adv} = \delta(\omega - \epsilon_{\mathbf{k}} + \mu)$ which corresponds to infinitely sharp ARPES peaks at band energies as drawn in Fig. 2.4 (a).

The central interest is to know how the spectral function, and thus the ARPES peak, is modified when switching on the interactions. This resumes to the calculation of the single particle Green's function, which is in general not an easy task for cases more general than the one described above. One manner to calculate Green's function is a perturbative approach in which the Green's functions are expanded into an infinite series and then evaluated approximately. All the effects of many body interactions on an electron in a solid are encapsulated into a fundamental function Σ called the irreducible self-energy. This term as we will see entirely determines the Green's function.

It contains every possible type of interaction that the electron can suffer such as electron-electron scattering, electron-phonon scattering with one, two... phonon processes. This self-energy is elegantly represented by the following Feynman diagram:

$$\Sigma = \text{[Diagram 1]} + \text{[Diagram 2]} + \text{[Diagram 3]} + \dots$$

where the dash and wavy lines correspond to the Coulomb and electron-phonon interaction, respectively.

We remark that the irreducible self-energy contains only terms which cannot be separated in two pieces by cutting a single propagator line. The Green's function can then be obtained from the following so-called Dyson equation:

$$G(\mathbf{k}, \omega) = G^0(\mathbf{k}, \omega) + G^0(\mathbf{k}, \omega)\Sigma(\mathbf{k}, \omega)G(\mathbf{k}, \omega). \quad (2.26)$$

Iterating this yields to

$$G(\mathbf{k}, \omega) = G^0 + G^0\Sigma G^0 + G^0\Sigma G^0\Sigma G^0 + \dots \quad (2.27)$$

(2.26) and (2.27) translated in Feynman diagram leads to

$$\begin{aligned} \text{---} &= \text{---} + \text{---} \circlearrowleft \Sigma \text{---} \\ \text{---} &= \text{---} + \text{---} \circlearrowleft \Sigma \text{---} + \text{---} \circlearrowleft \Sigma \text{---} \circlearrowleft \Sigma \text{---} + \dots \end{aligned}$$

Thanks to the Dyson equation the Green's function and the spectral function of an interacting system can be expressed in terms of the self-energy:

$$G(\mathbf{k}, \omega) = \frac{1}{G^{0-1}(\mathbf{k}, \omega) - \Sigma(\mathbf{k}, \omega)} = \frac{1}{\omega - \epsilon_{\mathbf{k}} + \mu - \Sigma(\mathbf{k}, \omega)} \quad (2.28)$$

and

$$A(\mathbf{k}, \omega) = \frac{1}{\pi} \frac{Im\Sigma(\mathbf{k}, \omega)}{(\omega - \epsilon_{\mathbf{k}} + \mu - Re\Sigma(\mathbf{k}, \omega))^2 + (Im\Sigma(\mathbf{k}, \omega))^2}. \quad (2.29)$$

The proof of Dyson equation is out of the scope of this thesis, but its final result implies that the excited state Green's function is obtained from (2.28) by just calculating the self-energy. However, one has to keep in mind that the self-energy is a summation over an infinite number of distinct diagrams, rendering this method applicable only if this self-energy can be approximated by the lowest order terms.

Compared to the non-interacting case, the spectral function (2.29) gives rise to a more structured ARPES spectrum with quasiparticle peaks at the energy $\epsilon_{\mathbf{k}} - \mu + Re\Sigma$ and with a damping rate of $Im\Sigma$. As can be seen in Fig. 2.4 (b), the line shape is composed of a coherent quasiparticle peak which becomes sharper when approaching the Fermi level and of the broad incoherent part which follows more or less the bare dispersion (dispersion in the absence of interaction).

2.4 Simulated example of the extraction of Σ from ARPES data

As solid state physicists we are interested in the spectral function of the photohole, which bears the information on the initial state. As shown above the self-energy contains all many body aspects

of the studied system and therefore a detailed knowledge of this quantity is of crucial importance to understand the physics behind. The self-energy is related to the ARPES signal through the relation (2.21), which has been obtained both within the three step model and the Green's function formalism. This expression does not consider the extrinsic effects of the photoelectron, however for the case of low-dimensional systems considered here these contributions can be neglected and thus this expression represents well the reality, meaning that $A(\mathbf{k}, \omega)$ and $\Sigma(\mathbf{k}, \omega)$ are available from ARPES data. Good examples of the application of this correspondance between ARPES and the self-energy can be found in the already-mentioned work of Claessen et al. on 1T-TiTe₂ [11] or in various observations of the electron-phonon coupling [13, 14, 34].

We will here present a procedure commonly used to extract the self-energy information from ARPES data, based on the so-called momentum distribution curves (MDC), i.e. ARPES signal plotted as a function of the momentum at a fixed energy. This technique has the advantage that if one assumes a negligible momentum dependence of the self-energy ($\Sigma(\mathbf{k}, \omega) \rightarrow \Sigma(\omega)$), the interacting spectral function (2.29) simplifies as:

$$A_{\omega}(\epsilon_{\mathbf{k}}) = \frac{1}{\pi} \frac{Im\Sigma(\omega)}{(\omega - \epsilon_{\mathbf{k}} - Re\Sigma(\omega))^2 + (Im\Sigma(\omega))^2} \quad (2.30)$$

which is a simple Lorentzian curve with position $\omega - Re\Sigma(\omega)$ and full width $2\Gamma = 2Im\Sigma(\omega)$. To check the accuracy of the self-energy extraction method we proceed as follow: first we calculate the spectral function with a given self-energy, then we introduce the Fermi cut off function and the effects of finite momentum and energy spectrometer resolution to obtain a simulated ARPES spectrum. Then we apply the MDC procedure and compare the self-energy extracted from the model data with the original assumption.

For our simulation we choose a model self-energy which contains only a contribution from electron-phonon interaction [14, 34, 35]. In case of weak momentum dependence of the electron-phonon coupling and at zero temperature the imaginary part of the self-energy can be written as [35]:

$$Im\Sigma(\omega) = \pi \int_0^{|\omega|} \alpha^2 F(\omega') d\omega' \quad (2.31)$$

where $\alpha^2 F(\omega')$ is the Eliashberg coupling function. The real part of the self-energy is obtained through the Hilbert transformation of $Im\Sigma$. With use of the 2D isotropic zero temperature Debye model for phonon an analytical form for this coupling function is obtained : $\alpha^2 F(\omega') = \lambda(\omega/\omega_D)^2$ for $\omega < \omega_D$ and zero otherwise . λ represents the strength of the coupling between electron and phonon and ω_D is the Debye energy. Within this Debye model we have finally:

$$|Im\Sigma(\omega)| = \begin{cases} \lambda\pi |\omega|^3 / (3\omega_D)^2, & |\omega| < \omega_D \\ \lambda\pi\omega_D/3, & |\omega| > \omega_D \end{cases} \quad (2.32)$$

and

$$Re\Sigma(\omega) = -(\lambda\omega_D/3)[(\omega/\omega_D)^3 \ln |(\omega_D^2 - \omega^2)/\omega^2| + \ln |(\omega_D + \omega)/(\omega_D - \omega)| + \omega/\omega_D] \quad (2.33)$$

To render our simulated ARPES spectra more realistic, we take into account the finite momentum resolution by summing the spectra within a given momentum window and convoluting the spectral function with a Gaussian function of a defined width to account for finite energy resolution. The simulated ARPES intensity, $I^{sim}(\mathbf{k}, \omega) = f(\omega) \int A_{\tilde{\omega}}(\epsilon_{\mathbf{k}}) Gauss(\tilde{\omega} - \omega) d\tilde{\omega}$, is plotted in Fig. 2.5 where the non-interacting band dispersion is $\epsilon_{\mathbf{k}} = -0.04 + 0.3k$, the Debye energy ω_D is 0,65 eV and the coupling constant λ is 0,65. The Fig. 2.5 shows the behaviour described in Fig 2.4

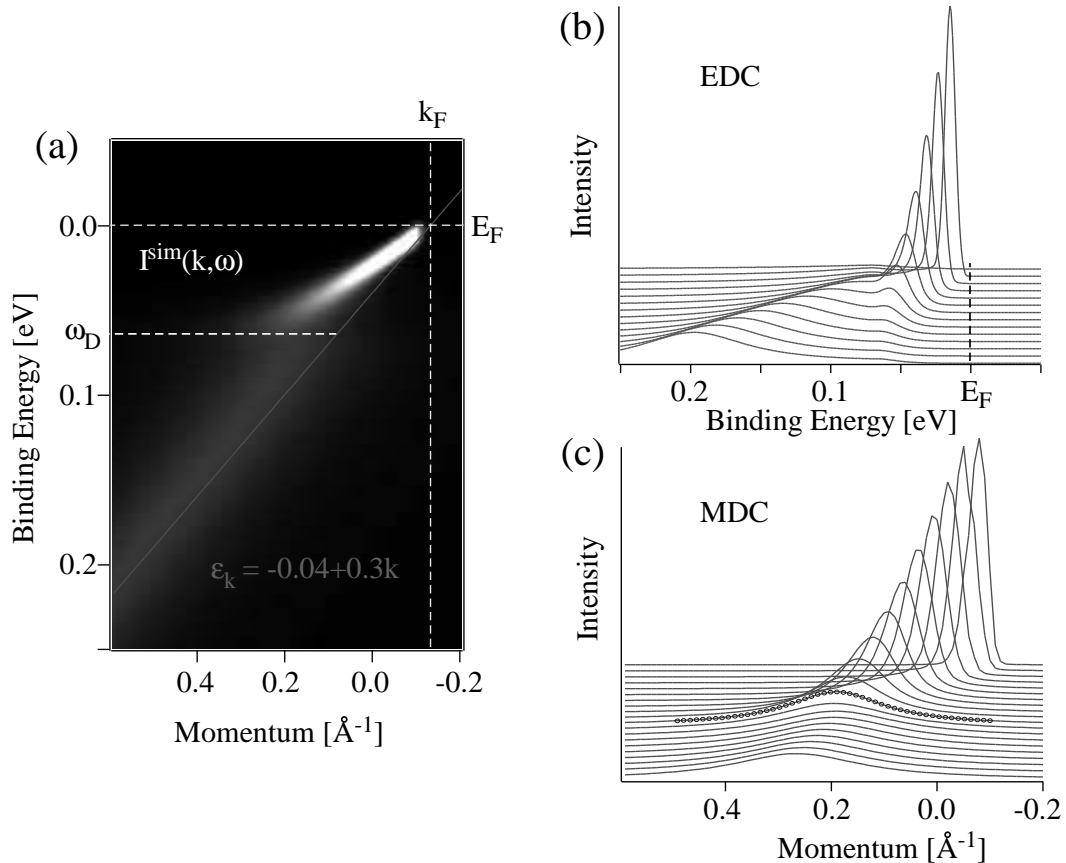


Figure 2.5: (a) Simulated ARPES intensity $I^{sim}(k, \omega)$ for the model self-energy (2.32), (2.33). ϵ_k is the interactionless dispersion and ω_D is the Debye energy characteristic of the phonons. (b) Energy distribution curves (EDC) corresponding to vertical cuts of (a). (c) Momentum distribution curves (MDC) corresponding to horizontal cuts of (a).

(b), namely a partition of the spectral weight into a coherent part (for $\omega < \omega_D$) and an incoherent part ($\omega > \omega_D$) following the interactionless dispersion. This complex behaviour is better seen in the energy and momentum distribution curves (EDC and MDC) shown in Fig. 2.5 (b) and (c), corresponding to vertical and horizontal cuts in the spectra of Fig. 2.5 (a), respectively.

To extract the self-energy from the model data we fit each MDC with the following function:

$$Fitfct(x) = h_0 + \frac{1}{\pi} \frac{h_6}{(\omega_{Fix}(h_3x + h_4) - h_5)^2 + h_1} \quad (2.34)$$

where h_1 and h_5 correspond to $Im\Sigma^{exp}$ and $Re\Sigma^{exp}$, respectively, ω_{Fix} is the energy position of the MDC and h_3, h_4 are dispersion parameters. h_0 and h_6 are free parameters.

The so-obtained $Im\Sigma^{exp}$ and $Re\Sigma^{exp}$ are plotted in Fig. 2.6 as functions of ω_{Fix} , for various energy and momentum resolutions. The agreement with the original self-energy is perfect for infinite momentum and energy resolution, while a finite resolution is smearing out the structures.

In this simulation we benefited from the preliminary knowledge of the free band dispersion ϵ_k which is usually not the case. This can be overcome by starting with a bare dispersion and adjusting it to get $Re\Sigma^{exp} = 0$ for $\omega_{Fix} = 0$ and $\omega_{Fix} \rightarrow \infty$.

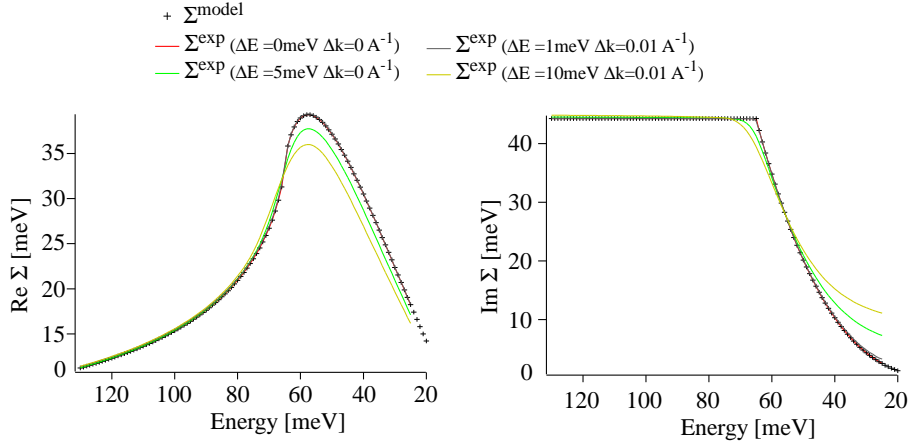


Figure 2.6: Real part $Re\Sigma$ and imaginary part $Im\Sigma$ of the self-energy extracted by fitting the MDC of Fig. 2.5 (c) with the fit function (2.34). To illustrate influence of the finite resolution the same procedure is applied for various energy and momentum resolutions.

References for chapter 2

- [1] H. Hertz, Ann. Physik **31**, 983 (1887).
- [2] A. Einstein, Ann. Physik **37**, 666 (1905).
- [3] N. V. Smith and M.M. Traum, Phys. Rev. B. **11**, 2087 (1975).
- [4] P.Aebi, J. Osterwalder, P. Schwaller, L. Schlapbach, M. Shimoda, T. Mochiku and K. Kawakami Phys. Rev. Lett. **72**, 2757 (1994).
- [5] J.-M. Imer, F. Patthey, B. Dardel, W.-D. Schneider and Y. Baer Phys. Rev. Lett. **62**, 336 (1989).
- [6] C. G. Olson, R. Liu, A.-B. Yang, D. W. Lynch, A. J. Arko, R. S. List, B. W. veal, Y. C. Chang, P. Z. Jiang and A. P. Paulikas, Science **245**,731 (1989).
- [7] Z.-X. Shen, D. S. Dessau, B. O. Wells, D. M. King, W. E. Spicer, A. J. Arko, D. Marshall, L. W. Lombardo, A. Kapitulnik, P. Dickinson, S. Doniach, J. DiCarlo, A. G. Loeser and C. H. Park, Phys. Rev. Lett. **70**, 1553 (1993).
- [8] D. Marshall, D. S. Dessau, A. G. Loeser, C. H. Park, A. Y. Matsuura, J. N. Eckstein, I. Bozovic, P. Fournier, A. Kapitulnik, W. E. Spicer and Z.-X. Shen, Phys. Rev. Lett. **76**, 4841 (1996).
- [9] A. G. Loeser et al. Science **273**,325 (1996).
- [10] H. Ding et al. Nature **382**,51 (1996).
- [11] R. Claessen, R. O. Anderson, J. W. Allen, C. G. Olson, C. Janowitz, W. P. Ellis, S. Harm, M. Kalning, R. Manzke and M. Skibowski, Phys. Rev. Lett. **69**, 808 (1992).
- [12] A. Damascelli, Z. Husain and Z.-X. Shen, Rev. Mod. Phys. **75**, 473 (2003).
- [13] T. Valla, A. V. Fedorov, P. D. Johnson, B. O. Wells, S. L. Hulbert, Q. Li, G. D. Gu and N. Koshizuka, Science **285**,2110 (1999).

- [14] M. Hengsberger, D. Parudie, P. Segovia, M. Garnier and Y. Baer Phys. Rev. Lett. **83**, 592 (1999)
- [15] A. Lanzara, P. V. Bogdanov, X. J. Zhou, S. A. Kellar, D. L. Feng, E. D. Lu, T. Yoshida, H. Elsaki, A. Fujimori, K. Kishio, J.-I. Shimoyama, T. Noda, S. Uchida, Z. Hussain and Z.-X. Shen, Nature **412**,510 (2001).
- [16] F. J. Himpsel, Adv. Phys. **32**, 1 (1983).
- [17] S. Hüfner, *Photoelectron Spectroscopy*(Springer-Verlag, Berlin, 1995).
- [18] S. D. Kevan, *Angle Resolved Photoemission-Theory and Current Applications*(Elsevier Science, Amsterdam, 1992).
- [19] W. E. Spicer, Phys. Rev. **112**, 114 (1958).
- [20] C. N. Berglund and W. E. Spicer, Phys. Rev. A **136**, 1030 (1964).
- [21] T. Miller, W. E. McMahon and T.-C. Chiang, Phys. Rev. Lett. **77**, 1167 (1996).
- [22] H. Martensson and P. O. Nilsson, Phys. Rev. B. **30**, 3047 (1984).
- [23] E. D. Kane, Phys. Rev. Lett. **12**, 97 (1964).
- [24] H. Becker, E. Dietz, U. Gerhardt and A. Angermueller, Phys. Rev. B **12**, 2084 (1975).
- [25] V. N. Strocov, R. Claessen, G. Nicolay, S. Hüfner, A. Kimura, A. Harasawa, S. Shin, A. Kakizaki, P. O. Nilsson, H. I. Starnberg and P. Blaha, Phys. Rev. Lett. **81**, 4943 (1998).
- [26] H. P. Hughes and H. I. Starnberg *electron spectroscopies applied to low-dimensional structures*(Kluwer Academic Publishers, London, 2000)
- [27] P. J. Feibelman and D. E. Eastman, Phys. Rev. B **10**, 4932 (1974).
- [28] J. B. Pendry, J. Phys. C **8**, 2413 (1975).
- [29] P. D. Johnson, J. Elect. Spectros. Relat. Phenom.**126**, 133 (2002).
- [30] G. D. Mahan, *Many-Particle Physics*(Plenum Press, New York, 1981)
- [31] D. Baeriswyl and N. Macris, *Méthodes à N corps en matière condensée*(Troisième cycle de la physique, 2000)
- [32] K. Elk and W. Gasser, *Die Methode der Greenschen Funktionen in der Festkörperphysik*(Akademie-Verlag, 1979)
- [33] D. Pines, *The Many-Body problem*(Benjamin Inc., 1961)
- [34] S. LaShell, E. Jensen and T. Balasubramanian, Phys. Rev. B **61**, 2371 (2000)
- [35] G. Grimval, Phys. Kond. Mat. **9**, 283 (1969)

Chapter 3

TMDCs quasi-two dimensional systems

3.1 Introduction

Layered TMDCs have attracted a widespread interest because of their unique electronic properties such as CDW and superconducting transitions. The compounds of this family have in common the formula MX_2 where M is a transition metal of the group IVb, Vb, VIb, VIIb or VIII and X stands for a chalcogen atom: sulphur (S), selenium (Se) or tellurium (Te). Structurally their quasi-2D character arises from their arrangement in a stacking of hexagonally packed planes forming X-M-X sandwiches weakly coupled to each other by van der Waals-type bonds. Depending on the stacking sequence of the sandwiches a further distinction into several polytypes is done. These are referred to as the 1T, 2H, 3R, 4H_a, 4H_b or 6R stacking-types. The number in this abbreviated notation denotes the number of X-M-X sandwiches per unit cell and T, H and R mean trigonal, hexagonal and rhombohedral symetries, respectively. The TMDCs subject of this thesis are all of the 1T-type. Regarding surface sensitive analysis technique like photoemission, these samples present the advantage of being easily prepared; indeed they can be easily cleaved, thus presenting a clean surface.

In what follows, structural and electronic properties of several 1T-type TMDCs are discussed in the context of a review article about ARPES method as probing bulk physics. Special attention is payed to the behaviour dependence on the degree of filling of the lowest lying d band.

3.2 Fermi surface of layered compounds and bulk charge density wave systems

F. Clerc,¹ C. Battaglia,¹ C. Monney,¹ H. Berger,² L. Despont,¹ M. G. Garnier,¹ and P. Aebi¹

¹ *Institut de Physique, Université de Neuchâtel, CH-2000 Neuchâtel, Switzerland*

² *Institut de Physique de la Matière Complexe, EPFL, CH-1015 Lausanne, Switzerland*

Submitted to J. Phys. C (2006)

A review is given on recent angle-resolved photoemission (ARPES) experiments and analyses on a series of layered charge density wave materials. Important aspects of ARPES are recalled in view of its capability for bulk band, Fermi surface and spectral function mapping despite its surface sensitivity. Discussed are TaS₂, TaSe₂, NbTe₂, TiSe₂ and TiTe₂ with structures related to the so-called *1T* polytype. Many of them undergo charge density wave transitions or exist with a distorted lattice structure. Attempts to explain the mechanism behind the structural reconstruction are given. Depending on the filling of the lowest occupied band a drastically different behavior is observed. Whereas density functional calculations of the electronic energy and momentum distribution reproduce well the experimental spectral weight distribution at the Fermi energy, the ARPES energy distribution curves reveal that for some of the compounds the Fermi surface is pseudogapped. Two different explanations are given, first based on density functional calculations accounting for the charge density wave induced lattice distortion and second relying on many body physics and polaron formation. Qualitatively both describe the observations well. However, in the future, in order to be selective, quantitative modeling will be necessary including the photoemission matrix elements.

3.2.1 Introduction

Context

From the experimental point of view, it is important to distinguish between surface versus bulk properties probed by the experiments, and to study implications on the experiment if the electronic structure has a two-dimensional (2D) or a three-dimensional (3D) character. Furthermore, why are we interested to map the Fermi surface (FS), and are we really measuring the FS?

In fact, we would like to learn about the low energy excitations of electrons, what interactions govern the properties of the system and whether we have quasiparticles. The topology of the FS gives an indication on the possible scattering channels of quasiparticles and is therefore an important ingredient for understanding the electronic properties. Naturally, electronic and lattice degrees of freedom are not independent, an aspect particularly interesting in CDW compounds where atom positions are modified thereby lowering the electron energy.

The interplay between lattice and electronic degrees of freedom has received renewed interest in the context of high-temperature superconductivity and colossal magneto resistance materials where electron-phonon coupling and possible polaronic effects are considered [1, 2]. A significant contribution to the discussion is given by angle-resolved photoemission experiments via analysis of the spectral function. Indeed, the one electron removal spectral function is one of the ingredients of the photoemission signal, containing the many body physics of the system.

The interpretation of the photoemission signal is a challenge, trying to extract information on the quasiparticles, their energy dispersion, self-energy and spectral function. The final goal

is to be able to obtain everything ranging from the electronic band structure and the FS to the many body physics and the excitation spectrum of electrons. The CDW materials present several interesting aspects in this context. First, electron-phonon coupling plays a role by definition and therefore these materials are a playground to study the interplay between the atomic and electronic structure, i.e. what is the strategy of the material to optimize its energy thereby creating the CDW, and second, unconventional spectral features discovered in the most important material's class of high critical temperature (T_c) superconductors can be compared to the ones obtained in this more conventional class of CDW compounds.

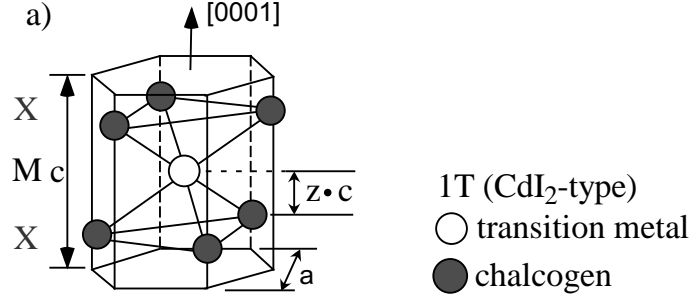


Figure 3.1: Sketch of the CdI₂-type 1T sandwich structure, transition metal atoms (M), chalcogen atoms (X). The trigonal elongation of the chalcogen octahedra along the c axis is characterized by the z -parameter.

Transition metal dichalcogenides

In the present article we consider a series of transition metal dichalcogenides (TMDCs). We discuss TaS₂, TaSe₂, TaTe₂, NbTe₂, TiSe₂ and TiTe₂, all in a structural form related to the so-called 1T polytype crystal structure (figure 3.1). Layered TMDCs are a class of quasi-2D materials. Many exhibit CDWs and even become superconducting at low temperatures. In the ionic picture the transition metal atom (M) has a $5d^36s^2$ (Ta), $4d^45s^1$ (Nb) or $3d^24s^2$ (Ti) configuration. The chalcogen atoms (X), S, Se and Te, with high electron affinity, have all a s^2p^4 configuration, missing two electrons for a filled shell. Therefore, the two chalcogen atoms per formula unit may attract a total of four transition metal d electrons and the degree of filling of the lowest lying d band will delicately influence the properties of the compound [3]. Nominally, Ta and Nb related compounds will be in a d^1 configuration whereas the ones with Ti will remain with zero d electrons (d^0).

Of course, hybridisation will modify this simplified view, but it is clear that the material's properties will be highly sensitive to the number of d electrons. The lower the number of electrons at E_F , the weaker the screening and the higher the tendency to instabilities. In this regard it seems likely that the heaviest metal (smallest electronegativity) together with the lightest of the chalcogen atoms (largest electronegativity), i.e. TaS₂, gives the most unstable combination and, on the other hand, TiTe₂ the most stable one. Indeed, TaS₂ has the most complicated phase diagram and TiTe₂ is a prototype for a 2D Fermi liquid.

Band structure calculations (figure 3.2(a)) confirm that the 6 lowest lying bands are mainly chalcogen related sp bands followed by a partially filled transition metal d band (downwards pointing arrows) and the rest of the metal d bands. The bulk Brillouin zone (BZ) of the three-fold symmetric 1T-structure as well as the surface BZ (SBZ) with corresponding high-symmetry points is indicated in figure 3.2(b). Due to the octahedral coordination of the metal atoms (figure 3.2(c)), the five d bands are split into a lower triplet of t_{2g} states and an upper doublet of e_g states (figures 3.2(a) and (d)). The σ bonding e_g orbitals have higher energies because they interact strongly

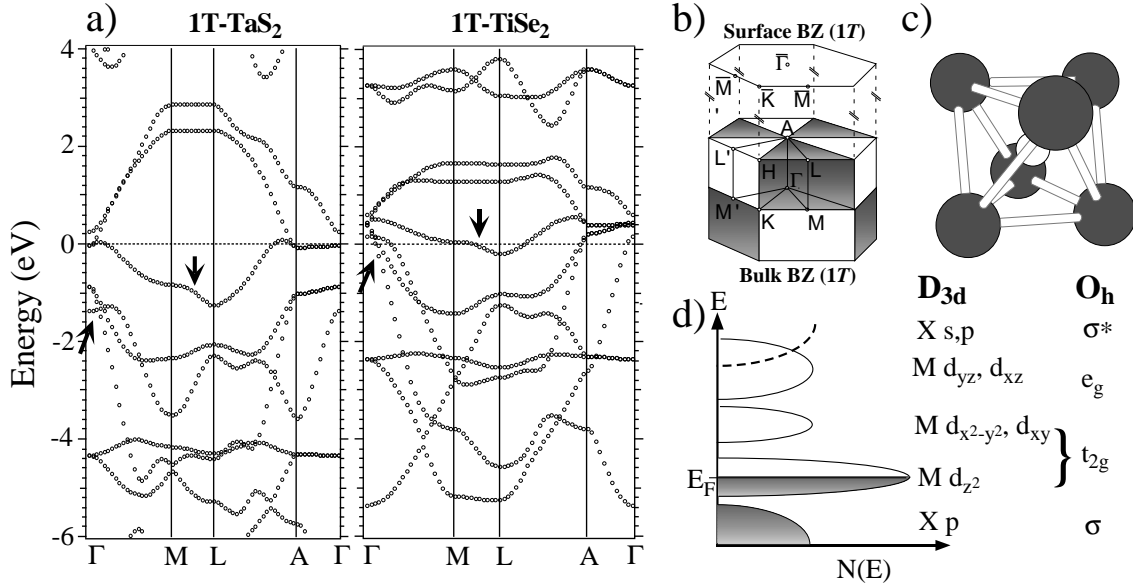


Figure 3.2: a) Calculated band structures, b) surface and bulk Brillouin zones of the $1T$ structure with labeled high symmetry points, c) octahedral coordination of the metal atoms, d) density of states with orbital characters in the ionic picture.

with the neighboring chalcogen atoms. The orbital degeneracy of the octahedral t_{2g} manifold is reduced in a Jahn-Teller like fashion by a trigonal elongation of the chalcogen octahedra along the c axis. This elongation influences the overlap of the metal d band with the highest chalcogen sp bands (figure 3.2(a), arrows pointing upwards) and is characterized by the so-called z -parameter as indicated in figure 3.1(a). A larger z -parameter indicates a larger metal-chalcogen distance and tends to lower hybridization.

Among the $1T$ compounds studied, TaS₂ and TaSe₂ are similar since they both exhibit an incommensurate (IC) CDW with $(\sqrt{13} \times \sqrt{13})$ symmetry at high temperature. At low temperature both compounds lock into the commensurate CDW with $(\sqrt{13} \times \sqrt{13}) - R 13.9^\circ$ symmetry. $1T$ -TaS₂ is more complicated additionally exhibiting a quasi-commensurate (QC) phase at intermediate temperature. TaTe₂ and NbTe₂ both stabilize in a monoclinically distorted version of the trigonal $1T$ polytype and can be interpreted as a (3×1) reconstruction [4,5]. Unlike TaTe₂, NbTe₂ becomes superconducting at ≈ 0.5 K [6]. After cooling of heat pulsed crystals to room temperature, transmission electron diffraction experiments reveal a second, CDW state with a $(\sqrt{19} \times \sqrt{19})$ signature [7–9], commensurate at room temperature, but readily rendered incommensurate just above. This observation is interesting since it links to the $(\sqrt{13} \times \sqrt{13})$ reconstruction of TaS₂ and TaSe₂.

$1T$ -TiSe₂ is different in the sense that the lattice is not distorted at room temperature. A $(2 \times 2 \times 2)$ reconstruction appears at ≈ 200 K together with a maximum in the resistivity [10,11]. $1T$ -TiTe₂ does not show any phase transition remaining in its trigonal high symmetry phase and is considered to be a prototype of a 2D Fermi liquid.

To get an overview on the different compounds we can classify them into two categories, the Ta (including Nb) compounds with d^1 configuration and the Ti related compounds with d^0 configuration. ARPES results within a given category are rather similar. Numerous studies of the electronic properties have been carried out for TMDCs [12–23]. For practical reasons, in this review article, results will be shown only for some of the compounds, but the discussion will involve all of them.

3.2.2 Aspects of photoemission

Even for quasi-2D materials such as the layered TMDCs, the photoemission experiment proceeds in the real 3D world and attention has to be paid to the fact that the escape depth of electrons is small. The result is that ARPES is very surface sensitive unless extremely high (of the order of a few keV) or low (5 - 10 eV, e.g. lasers) photon energies are used. Therefore, experiments such as the ones presented here effectively probe the surface electronic structure. Depending on the material and the presence of surface relaxation and/or reconstruction of atomic positions, so-called surface states may exist besides the bulk states. While surface states are interesting by themselves, they are not relevant for the bulk physics we are interested in here. Surface states (perfectly 2D objects) may exist in a region of wave vectors parallel to the surface (\mathbf{k}_{\parallel} region) and energy interval where there are no bulk states available for all wave vectors perpendicular to the surface (\mathbf{k}_{\perp}), i.e. where the bulk band structure is gapped. Furthermore, surface states are very sensitive to surface modification, e.g. due to adsorbates or contamination and do not show any dispersion as a function of \mathbf{k}_{\perp} . From these criteria we did not find indications for surface states in the experiments presented here.

Another important aspect occurring due to the surface sensitivity of ARPES is the following. Within first order time dependent perturbation theory ARPES is described by the Fermi golden rule giving the transition probability between two stationary states due to the perturbation, i.e. the photon field. Since for ARPES the contribution of the surface is dominant, the stationary states are the ones respecting the boundary conditions of a semi infinite solid. These are called inverse LEED states, named in connection with the low energy electron diffraction (LEED) experiment. The point is that parallel to the surface, periodicity is intact (maintaining Bloch states with quantum number \mathbf{k}_{\parallel} , 2D Bloch states) whereas it is broken perpendicular to the surface (\mathbf{k}_{\perp} is not a good quantum number, i.e. it is not conserved). In quantum mechanics, a trick is, to still use \mathbf{k}_{\perp} as a quantum number but to give it a "live time" or a "broadening" (\mathbf{k}_{\perp} broadening), instead of admitting a linear combination of basis functions from a complete set (i.e. the 3D Bloch functions) and calculating the inverse LEED states. Often in the literature this non-conservation of \mathbf{k}_{\perp} is associated with an electron and hole life time and the finite mean free path of the electron. The life time and mean free path of the electron due to interactions, however, are not specific for \mathbf{k}_{\perp} . But the association may be understood by the fact that electron interactions indeed are responsible for the surface sensitivity and therefore for the non-conservation of \mathbf{k}_{\perp} .

As a consequence, a strict momentum conservation of the 3D wave vector \mathbf{k} is not guaranteed and only \mathbf{k}_{\parallel} is conserved. This may have dramatic consequences particularly for 3D materials where for a given \mathbf{k}_{\parallel} different \mathbf{k}_{\perp} contribute to the ARPES signal, especially for \mathbf{k}_{\perp} with a high density of states (DOS), leading to a \mathbf{k}_{\perp} smearing and the measurement of the so-called 1D-DOS [24]. For 2D materials, as it is our case, the situation is to our advantage in the following sense. The transition in the Fermi golden rule goes from the initial state (ground state of the N electron system) to the final state, consisting (within the sudden approximation) of an N-1 electron system with a factorized independent electron in the detector. The N-1 electron system of the 2D material leads to the description of the ARPES signal in terms of the one electron removal spectral function $A(\mathbf{k}_{\parallel}, \omega)$ depending only on \mathbf{k}_{\parallel} and the electron energy ω and a 3D final state single electron reaching the detector. This 3D final state indeed suffers from \mathbf{k}_{\perp} broadening, inducing also an energy broadening, with the advantage of filling possible final state energy gaps. For strictly 2D electron systems this final state energy and \mathbf{k}_{\perp} broadening is not affecting the line shape of the ARPES signal, it is only influenced via an energy and \mathbf{k} dependent matrix element. However, a slight departure from the 2D character may already result in a broadening, not to be mixed up with spectral function effects (many body physics) [25].

3.2.3 Experiments and calculations

Traditionally, in ARPES, relatively few energy distribution curves (EDCs) were measured for different angles in order to determine the bandstructure and the \mathbf{k}_{\parallel} location where bands cross the Fermi level (E_F). Then, Santoni *et al.* [26] used an alternative way to obtain the same information. With a 2D display-type analyzer they mapped the FS of layered graphite directly by measuring the total intensity within a narrow energy window at E_F . Inspired by Ref. [26] sequential angle-scanning data acquisition [27, 28], as introduced by the surface structural x-ray photoelectron diffraction (XPD) method, was used to map the intensities within a narrow energy window at the Fermi energy [29–31]. It was also realized that simple intensity mapping at E_F as a function of angle or \mathbf{k}_{\parallel} might not be sufficient to determine the Fermi vector (\mathbf{k}_F) and that a combination of intensity mapping and EDCs is necessary in order to verify whether a quasiparticle peak indeed crosses the Fermi level [32]. Another, most important finding was that so-called angular distribution curves (ADCs), nowadays also called momentum distribution curves (MDCs), i.e. intensities as a function of angle or \mathbf{k}_{\parallel} for a fixed binding energy, are much easier to interpret and to fit for quantitative interpretation in terms of the spectral function than the traditional EDCs because of their much simpler line shape (Lorentz-function type functionality of the spectral function) [33–36]. The analysis of ADCs instead of EDCs has been applied successfully to the cuprate high T_c superconductors [37]. These ARPES modes are well established now and have proven their power on many systems [31, 32, 36, 38].

ARPES EDCs were acquired with a Scienta SES-200 hemispherical electron energy analyser with energy and angular resolution of 5 meV and 0.25° , respectively, while the Fermi surface mapping (FSM) measurements have been collected in a modified Vacuum Generator ESCALAB Mk II spectrometer [39] with energy and angular resolution of 50 meV and 0.5° , respectively. The sequential motorized sample rotation has been described elsewhere [31].

Monochromatized He I photons of energy 21.22 eV were used for all measurements reported here. The samples were prepared by vapour transport and cleaved *in situ* at pressures in the 10^{-10} mbar region at room temperature. Surface cleanliness before and after ARPES measurements was monitored by x-ray photoelectron spectroscopy (XPS), while LEED was used to check the sample orientation and the evolution of the CDW superstructures. The Fermi energy and instrumental energy resolution were calibrated by measuring a polycrystalline copper sample.

First principle calculations were performed in the framework of density functional theory (DFT) using the full potential augmented plane wave plus local orbitals (APW+lo) method in conjunction with the generalized gradient approximation (GGA) in the parametrization of Perdew, Burke and Ernzerhof [40] as implemented in the WIEN2k software package [41] as well as the ABINIT code [42, 43] using the local density approximation (LDA) and relativistic separable dual-space Gaussian pseudopotentials [44]. A recent extension to WIEN2k based on the OPTICS package allows the computation of the imaginary part of the static electronic susceptibility $\chi(\mathbf{q})$ [45]. The phonon dispersion is computed with the help of density functional perturbation theory (DFPT) capabilities of ABINIT [46, 47].

3.2.4 Results and discussion

Pseudo gap and missing Umklapp bands

Figure 3.3 presents FSMs for TaS₂ and TiSe₂ collected at room temperature (figures 3.3(a) and (b)). A DFT based calculation for the undistorted or normal state structure, using a free electron final state, is shown in figure 3.3(c). The measurements shown in figures 3.3(a) and (b) are typical for the nominally one and zero d electron compounds, respectively (see above). The different filling translates into a different sized ellipse around the \bar{M} point as illustrated in figure 3.3(d). In fact,

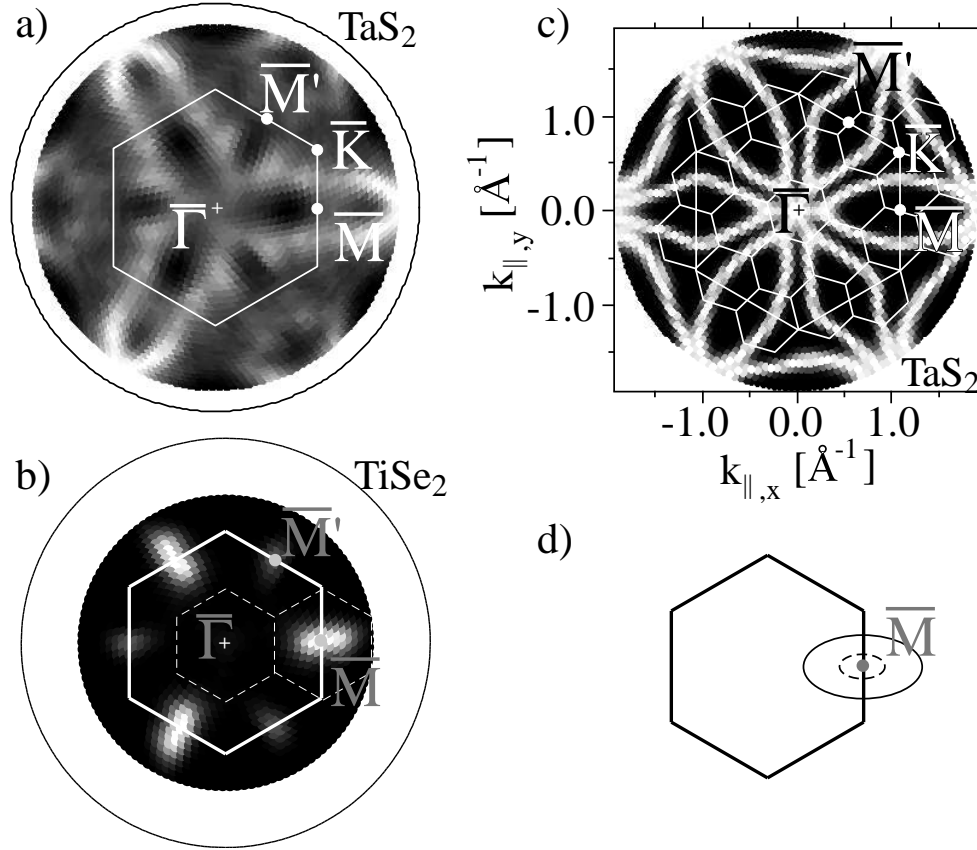


Figure 3.3: Fermi energy maps for a) TaS₂ and b) TiSe₂. Raw data has been normalized by the mean azimuthal value (see text). c) Density functional theory based simulation for TaS₂, inscribed are the CDW-induced reconstructed BZs and a possible nesting vector across \bar{M} . High intensity is in white. d) Sketch of the elliptically shaped Fermi energy contours for nominally one d electron (large ellipse) and zero d electron (small ellipse) filling.

FSMs for TaSe₂ [19] TaTe₂ and NbTe₂ [5] are very similar to the result for TaS₂ and the FSM for TiTe₂ [32] resembles the one of TiSe₂.

The calculated lines (only shown for TaS₂, figure 3.3(c)) agree well in shape with the measurements for all compounds. Differences exist mainly in the intensities with marked three-fold symmetry for the experiments. This is attributed to matrix element effects [13]. Note that figure 3.3(a) presents normalized data. In fact, for the raw data (not shown, see Ref. [5, 12, 13, 19]) intensity is maximal near normal emission ($\bar{\Gamma}$) and falls off rather quickly towards larger polar angles. This behavior is observed for TaS₂, TaSe₂, TaTe₂ and NbTe₂ and has been attributed to the d_{z^2} character of the transition metal band [13]. A normalization of the FSM by the mean intensity for each polar emission angle as shown in figure 3.3(a) eliminates this dependence and allows to reveal weaker off-normal features. However, centered circular features are then suppressed with the consequence that the closing of the ellipse near $\bar{\Gamma}$ is not apparent in the normalized data.

The important point to notice is that the CDW induced lattice distortion is present at room temperature for TaS₂, TaSe₂ as well as TaTe₂ and NbTe₂. However, the corresponding umklapp bands with the symmetry of the BZs due to the reconstruction (as inscribed in figure 3.3(c)) are not clearly observed. A second important observation is that, again for all but TiSe₂ and TiTe₂, the high intensity lines in the experiment do not correspond to Fermi energy crossings of intensity maxima or quasi particle peaks [5, 12, 19]. This is verified with EDCs measured across these high intensity lines as shown in figure 3.4(a). EDCs are displayed along the $\bar{\Gamma} - \bar{M}$ direction for NbTe₂,

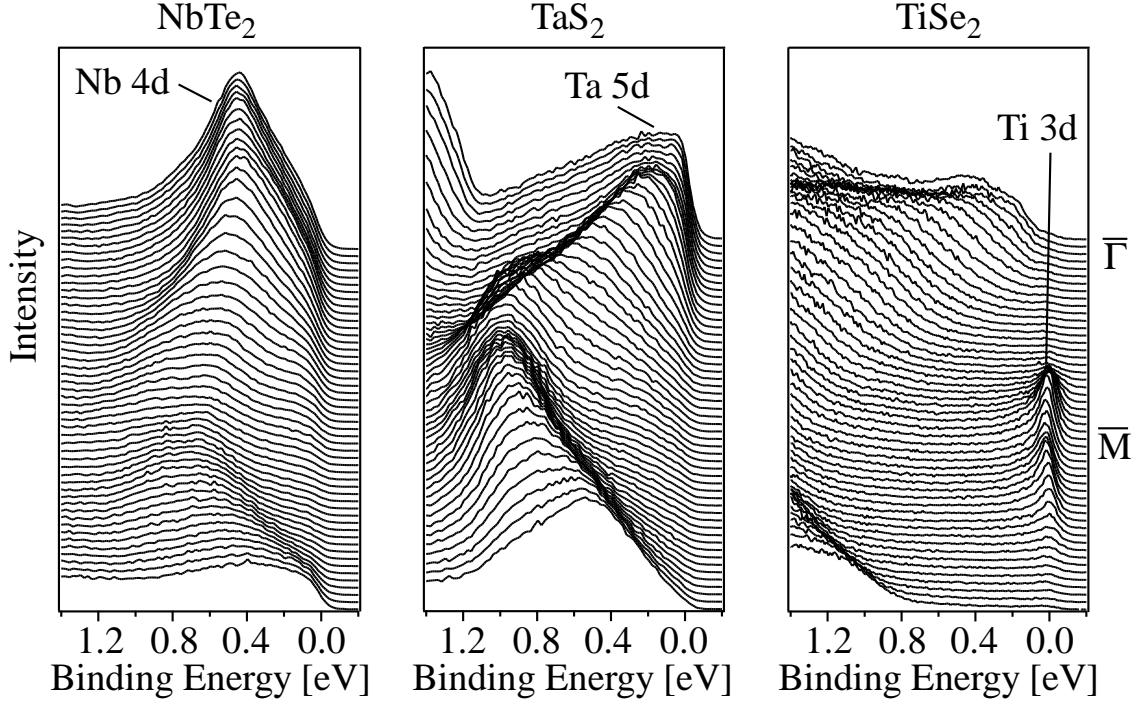


Figure 3.4: He I excited energy distribution curves along the $\bar{\Gamma} - \bar{M}$ direction for NbTe₂, TaS₂ and TiSe₂.

TaS₂ and TiSe₂. The dispersion of the *d* band is what is expected from the elliptically shaped FSM contours. What is striking, however, for NbTe₂ and TaS₂, is a characteristic back bending of the intensity maximum when approaching E_F , *not* crossing E_F but provoking considerable spectral weight at E_F (as seen in the FSM in figure 3.3). No quasiparticle crossing has been found for any of the measured energy dispersion curves. Thus, strictly speaking, the maps for TaS₂, TaSe₂ and NbTe₂ are not Fermi surfaces. The observed intensity originates from bands which come close to the Fermi level, but must not be associated with quasiparticle crossings, but rather spectral weight which leaks across the Fermi level. The signature of such a pseudogapped Fermi surface is also observed in high T_c superconductors [48] and has remained a controversial topic.

Therefore, for all but TiSe₂, the FSMs show that there is a so-called pseudogapped Fermi surface. As for TiSe₂, this is also not the case for TiTe₂, considered as prototype for a 2D Fermi liquid [49–51] where ARPES shows sharp quasiparticle peaks becoming increasingly narrow when approaching E_F according to what is expected from their life time.

The point to discuss is whether the two observations, i.e. a pseudogapped FS and the non-observation of the Umklapp bands are connected. From a deeper investigation of TaS₂ using DFT calculations it turns out that a connection can be made [19] as follows. From a band structure calculation point of view, even the slightest atom displacement inducing a structural reconstruction with symmetry breaking (such as indicated in figure 3.5(a)) will immediately introduce a new BZ (figure 3.5(b)) with back-folded bands (figure 3.5(c)). However, for sufficiently small atom displacements the electron wave functions probed by ARPES will practically be unaffected. Therefore, a band structure calculation of the reconstructed crystal structure will display a wealth of new bands (sub-bands, dotted lines in figure 3.5(c)), but the spectral weight distribution measured by ARPES will basically continue to follow the band structure of the unreconstructed lattice (open circles in figure 3.5(c)) [52]. In figure 3.5(d) the situation is explained for a quasi-1D atomic chain. The top and bottom panels show the unreconstructed and reconstructed chains, respectively. The influence of the reconstruction on the electronic structure (back-folded bands, FS) is sketched

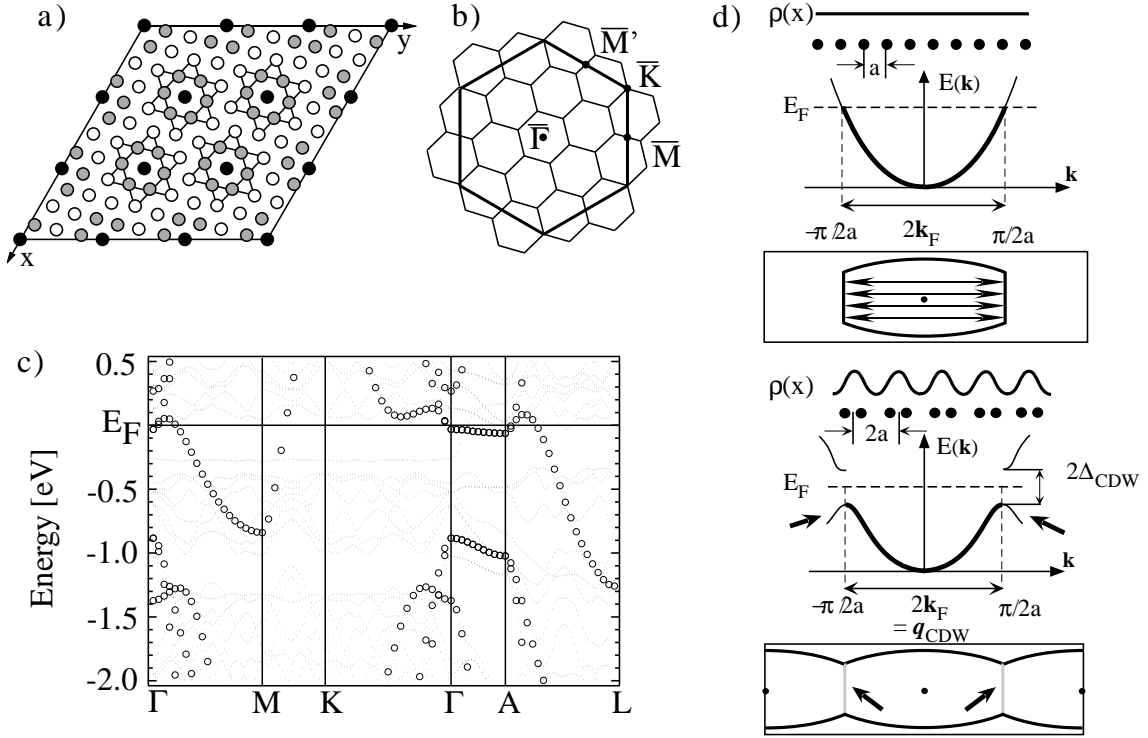


Figure 3.5: Band structure calculations for CDW phase a) Sketch of the Ta-plane with CDW-induced $(\sqrt{13} \times \sqrt{13}) - R 13.9^\circ$ reconstruction. b) TaS₂ normal state (large hexagon) and CDW-induced (small hexagons) BZs. c) TaS₂ band structure calculation for the distorted structure (dotted lines) calculated along high symmetry points of the normal state BZ together with the band structure of the normal state structure (open circles). d) Sketch of the behavior of the bandstructure and Fermi surface contours of a quasi-1D system with one electron per unit cell. Arrows indicate weak spectral weight observed on Umklapp bands (see text).

(arrows). The spectral weight on the new bands will depend on the scattering strength of the potential with the new symmetry. With this in mind we can understand that the observed EDCs (figure 3.4) display an intensity distribution following the sub-bands, but are heavily weighted by the bands of the unreconstructed structure. This is in agreement with the observation of a pseudogap since the topmost sub-band is present all over the BZ with empty states very close to E_F (figure 3.5(c)). Within this explanation, we are always finding spectral weight at E_F , whether it is originating from thermal occupation via the Fermi-Dirac distribution or whether states are truly below E_F . However, since these states are merely straddling E_F , we cannot observe a true crossing of a quasiparticle peak and hence experience a pseudogap behavior displaying an intensity distribution of spectral weight according to the unreconstructed lattice. Figure 3.6 is in agreement with this view. It shows the spectral weight distribution at E_F for TaS₂ measured at 20 K deep in the commensurate CDW phase, together with an FSM calculated for the $(\sqrt{13} \times \sqrt{13}) - R 13.9^\circ$ structure (see also figure 3.5(c)). The agreement is nice with high intensity in the center of the new BZs. However, TaS₂ when transiting to the commensurate CDW phase undergoes a Mott transition [53, 54] and is not metallic anymore. Nevertheless, the remaining experimental spectral weight distribution at E_F follows the symmetry of the new BZs [55]. Therefore a possible explanation of the pseudogap is given using the single particle picture and band structure calculations together with the fact that Umklapp bands carry only weak spectral weight. Although an identical analysis for TaSe₂, TaTe₂ and NbTe₂ has not been done, a similar explanation may also apply.

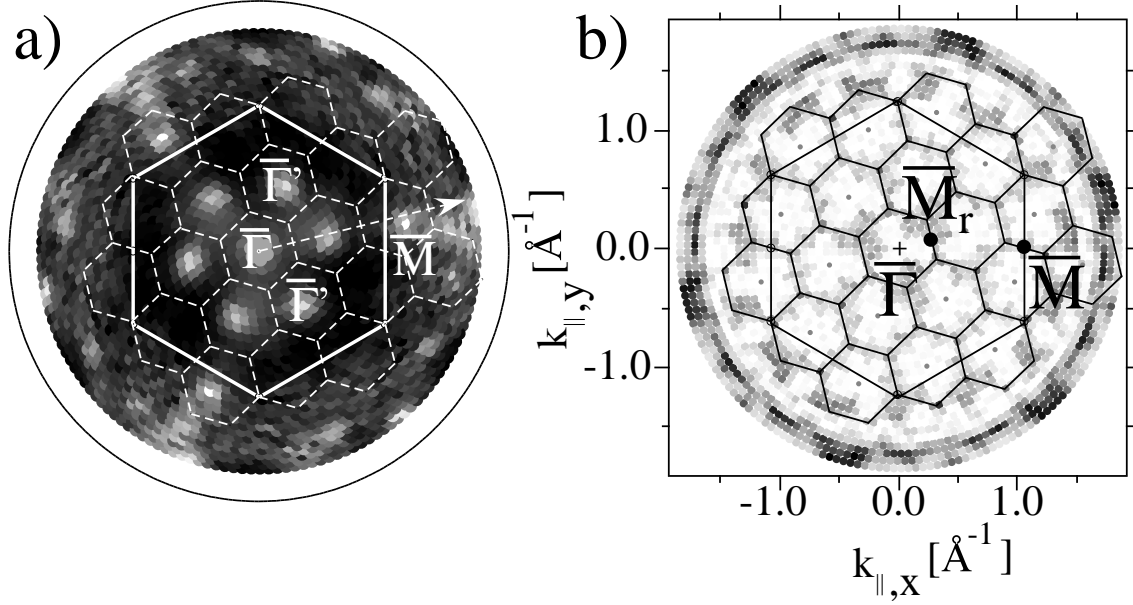


Figure 3.6: a) TaS₂ Fermi energy map measured in the commensurate phase at 20 K. Superimposed on it are the (1x1) BZ boundaries as well as the BZ boundaries of the commensurate ($\sqrt{13} \times \sqrt{13}$) - R 13.9° superstructure in thin dashed lines. b) Calculation of the FSM based on the (CDW phase) band structure (figure 3.5(c)). High intensity is in white.

Fermi surface nesting

The next point, which will lead us to a deeper understanding, is the question of the origin of the lattice distortion. What is the strategy of the material to gain electronic energy necessary to compensate the elastic energy for the lattice distortion? The classical mechanism in 1D for the occurrence of a CDW is the Peierls instability [56, 57] where a metal becomes unstable with respect to a spatially modulated perturbation with wave vector \mathbf{q}_{CDW} equal to two times the Fermi vector $2\mathbf{k}_F$ (figure 3.5(d)). This leads to the formation of electron-hole pairs with the same wave vector and finally to the opening of a gap which provides a gain in electronic energy in order to compensate the elastic energy paid for the lattice distortion. Figure 3.5(d) (top) displays the case of a strongly nested FS as indicated by arrows connecting nested (parallel) parts of the FS contour. One electron per atom (and unit cell) of chains of atoms with distance a is assumed. Therefore the Fermi vector is $k_F = \pi/(2a)$ since the quasi-1D band is half filled. The BZ boundary is located at $2k_F = \pi/a$ (figure 3.5(d), top). If the lattice is distorted in order to double the periodicity, i.e. to introduce a CDW with wave length $2a$, elastic energy has to be paid. At the same time a doubling of the periodicity in real space results in reducing the dimension of the BZ by a factor of two. The consequence is that the new BZ boundary is now located at $k_F = \pi/(2a)$ and the band is full (two electrons per unit cell, due to the doubling of the periodicity) with the opening of a gap at the new BZ boundary at $\pi/(2a)$ and a corresponding gain of electronic energy. However, especially for long \mathbf{q}_{CDW} (with many small new BZs) and imperfect nesting (with remaining small metallic pockets) it may be difficult to follow in detail the reconstruction and back folding of bands unless they carry enough spectral weight (see above). The driving force for such an instability is given by the topology of the Fermi surface (FS) which has to present favorable nesting conditions. Namely, large portions of the FS have to be connected or nested by the vector \mathbf{q}_{CDW} . A good indicator of the quality of the nesting is the imaginary part of the static electronic susceptibility $\chi(\mathbf{q})$ [58] which, in linear response theory, relates the response of the system to the perturbation. An estimate of the imaginary part of the static electronic susceptibility $\chi(\mathbf{q})$ may

be defined as $\Im\chi(\mathbf{q}) = \sum_{n',n,\mathbf{k}} \delta(\varepsilon_{n',\mathbf{k}+\mathbf{q}} - \varepsilon_{n,\mathbf{k}})$, neglecting matrix elements [5, 59]. The Dirac function δ gives a contribution or not depending on whether \mathbf{q} is a nesting vector or not.

For TaS₂, computation of $\Im\chi(\mathbf{q})$ [55] (not shown) for $q_{\perp} = 0$ gives a local maximum around $\mathbf{q}_{\parallel} = 1/\sqrt{13} \times \mathbf{a}^*$, consistent with Myron's [60] calculations obtained for a more limited set of \mathbf{q} vectors. The maximum is located along the Γ -M direction, 13.9° off with respect to the CDW wave vector of the commensurate phase. This is consistent with the CDW direction of the IC phase rotation by 13.9° while passing through the IC to QC phase transition. However, while FS nesting is a plausible explanation for the onset of the CDW, the overall quite large value of $\chi(\mathbf{q})$ found at least along Γ -M is intriguing and questions whether a relatively small and broad maximum at $\mathbf{q}_{\parallel} = 1/\sqrt{13} \times \mathbf{a}^*$ is sufficient to explain the occurrence of the IC CDW. As pointed out by Johannes et al. [58], definitive evidence for the contribution of nesting to the CDW formation needs confirmation by calculations of the real part of the static electronic susceptibility.

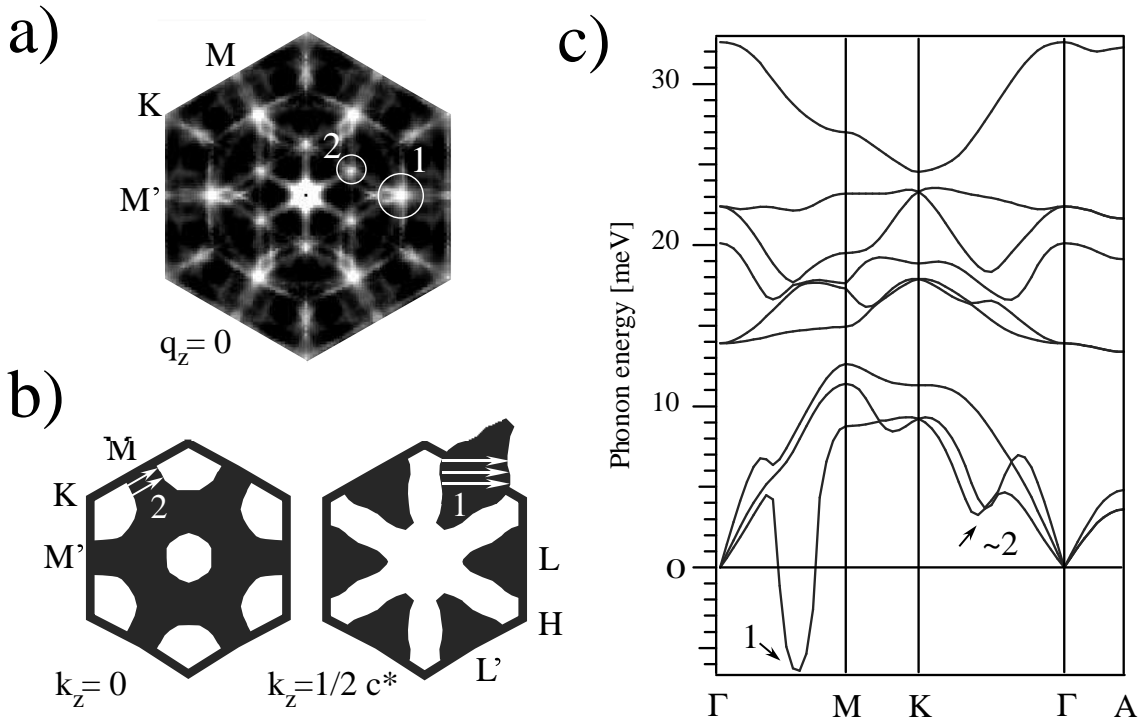


Figure 3.7: Calculations for 1T-NbTe₂. a) Results of $\Im\chi(\mathbf{q})$ calculations within the first Brillouin zone at $q_z = 0$ (Γ MK plane) obtained by integration of the APW+lo FS. The peak marked 1 occurs exactly at $q_x = \frac{1}{3}a^*$. Feature 2 is close to the nesting vector of the $\sqrt{19} \times \sqrt{19}$ CDW phase. b) APW+lo calculations of cuts through the Fermi surface at $k_z = 0$ and $k_z = c^*/2$. Nesting vectors of length $q = 1/3a^*$ feature 1 and $q = 0.19a^*$ feature 2 are indicated. c) Phonon dispersion of 1T-NbTe₂ along high symmetry lines obtained by the response function capabilities of ABINIT. Frequencies below 0 meV are imaginary. All free degrees within the trigonal P3m1 space group were relaxed using the Broyden-Fletcher-Goldfarb-Shanno minimization scheme as implemented in the ABINIT code.

For NbTe₂ the situation is more clear cut. Its structure is a monoclinically deformed 1T arrangement. LEED measurements suggest that the structure can be understood in terms of a (3×1) superstructure. For completeness, we note that the bulk structure exhibits a $(3 \times 1 \times 3)$ supercell structure, since successive layers are shifted within the plane. The results of $\Im\chi(\mathbf{q})$ calculations are presented as linear gray scale plots in figure 3.7(a) with white indicating a large response of the electron system. Strong nesting is present for small, but non-vanishing \mathbf{q} vectors.

These contributions are due to intraband nesting from weakly dispersing bands and can be reduced by choosing a smaller energy window.

Highly interesting is the peak at $\mathbf{q} = \frac{1}{3}\mathbf{a}^*$ along the ΓM and $\Gamma\text{M}'$ directions in figure 3.7(a) (feature 1). We associate this peak with a nesting vector leading to the (3×1) superstructure observed by LEED and plotted in the calculated FS cut in figure 3.7(b). Thus, the electronic structure of trigonal NbTe_2 appears unstable with respect to a potential with wavevector $\mathbf{q} = \frac{1}{3}\mathbf{a}^*$. As discussed in Ref. [5], a second maximum (feature 2) at $\mathbf{q} = 0.19\mathbf{a}^*$ along ΓK might be related to the $(\sqrt{19} \times \sqrt{19})$ CDW phase, which was observed after cooling of heat-pulsed crystals to a temperature just above room temperature [61].

The occurrence of a maximum in the electron susceptibility alone does not explain the distortion to the monoclinic structure. The presence of a perturbation with the corresponding \mathbf{q} vector is necessary. In the one-dimensional Peierls scenario this potential is provided by a soft phonon mode.

The DFPT phonon bandstructure for the relaxed trigonal NbTe_2 structure obtained by diagonalization of the dynamical matrix along high symmetry lines is shown in figure 3.7(b). The lowest lying acoustic branch exhibits imaginary frequencies. DFPT contains the implicit assumption that phonons are simple harmonic modes. Soft modes are by definition anharmonic and their frequency goes to zero. Zero frequency implies that the lattice structure is unstable and will transform, typically, to a lower symmetry phase. In the extreme case, electronic structure calculations may give an imaginary phonon frequency indicating that the ideal structure is unstable [62]. The phonon frequencies are the square roots of the eigenvalues of the dynamical matrix. Imaginary frequencies correspond to negative eigenvalues of the dynamical matrix. A negative entry in the diagonalized dynamical matrix contributes a negative energy to the total Hamiltonian, indicating that the expansion was not carried out around the equilibrium configuration. Thus there exists an energetically more favorable configuration. At high temperature, the lattice has sufficient energy to overcome the energy barrier between two or more symmetry-related variants of the low temperature structure such that the average observed structure has higher symmetry. In such cases the ideal structure is stabilized by high temperature and will undergo a phase transition on cooling, to a low temperature phase whose symmetry differs by the symmetry of the imaginary mode.

The most unstable modes in figure 3.7(b) occur along $\mathbf{q} = (1/3, 0, q_z)a^*$. This strongly supports the Fermi surface nesting scenario for NbTe_2 . Furthermore, from an analysis of the eigenvectors of the dynamical matrix, the distorted structure may be qualitatively constructed.

Electron phonon coupling

Despite the explanation given above for the absence of any clear quasiparticle crossing at E_F using DFT calculations, relying on many new BZs and Umklapp bands with weak spectral weight, the broad spectral weight distribution instead of delta-function like peaks, is peculiar. Electron-phonon coupling is expected to be relatively strong for the CDW compounds [61] and consequently polaronic effects may also play a role. Polarons recently received increased attention for the interpretation of anomalously broad ARPES features [1, 51, 63]. The polaron concept was first introduced by Landau [64] and represents an electron moving in a polarizable lattice carrying the lattice deformation with it. In the Holstein model [65] one assumes an on-site coupling of the electrons with dispersionless lattice vibration modes. Thus this model is adapted to short range electron-lattice interaction and refers to a small polaron. Since for increasing strength of the coupling the polaron radius shrinks to a single lattice site, the Holstein model is more suitable to study strong interactions. In the case of the Fröhlich Hamiltonian [66] long-range electron-lattice interaction is also active with lightly dressed particles polarizing the environment weakly on a large spatial extend around themselves. Thus in this case the polaron is called a large polaron. The

influence of electron-phonon coupling, if strong enough, may even gap a non-nested FS as shown by recent numerical calculations of the spectral function for the spinless Holstein model [67]. An illustration of this behavior at half filling is shown in figure 3.8(a). In the weak coupling regime most of the spectral weight close to k_F resides in the polaronic quasiparticle. The dispersion of this band exhibits a mass enhancement due to the weak dressing of the electron. Further away from k_F the polaron band is no more visible since most of the spectral weight is transferred to the incoherent part which follows the bare (not re-normalized) dispersion $\epsilon(k)$. For strong coupling the spectrum consists again of the polaronic quasiparticle and an incoherent part. However, as a consequence of the predominantly local effects in the strong coupling regime, the polaron quasiparticle contains almost zero electronic spectral weight for the whole momentum range and turns to a very narrow band. The incoherent part, where the electronic spectral weight is concentrated, broadens and does not cross the Fermi level but flattens in its proximity forming a pseudogap.

Intuitively this behavior can be understood from the exactly solvable model for the coupling of a single electron to a bath of independent phonons of frequency ω_0 [68]. The broad line shapes as well as the vanishingly small quasiparticle spectral weight comes naturally from the calculated spectral function of this model. Figure 3.8(b) sketches the outcome for the fixed particle with bare energy ϵ_c interacting with a set of Einstein phonons of frequency ω_0 . Due to the coupling the ground state energy is shifted by $\Delta = g\omega_0$, g being the coupling. The spectral function is an envelop of many individual peaks spaced by ω_0 . The peak closest the Fermi level is the quasiparticle peak or zero-phonon peak. It is shifted by Δ from the non-interacting energy position ϵ_c . The following peaks are satellites. They indicate that the single electron is not an eigenstate of the Hamiltonian and the particle has a finite probability of occupying other states carrying l phonons with it. From the PES point of view it means that a removal of an electron from the system occurs with a probability of shaking off a certain number of bosons. This picture also refers to what is called the Franck Condon broadening. Depending on the coupling more or less spectral weight is concentrated on the quasi-particle peak and the broadening is more or less pronounced. A polaron scenario thus allows to explain the apparent absence of quasiparticle crossings as well as the broadened line shape in the experimental ARPES spectra.

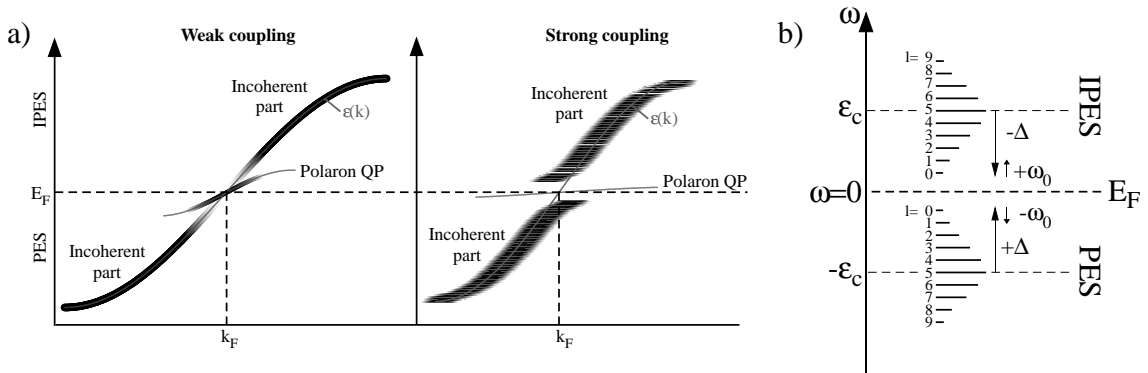


Figure 3.8: a) Schematic inverse photoemission (IPES, $\omega > 0$) and photoemission (PES $\omega < 0$) spectral functions adapted from the numerical calculations of the Holstein problem for the two limits of weak and strong coupling [67]. b) Spectral function of a single fixed electron coupled to a bath of phonons of frequency ω_0 [68]. The spectrum consists of a multi-peak structure and the quasi-particle ground state is shifted from the free electron energy ϵ_c by Δ which is larger for strong coupling. The stronger the coupling the more spectral weight is transferred to the satellites ($l > 0$) with maximum intensity on the centroid of the spectrum.

Figure 3.9 presents ARPES measurements in the IC and QC phases, taken at 350 K and 344 K, respectively. The intensity plots (high intensity in black) on figure 3.9(a) are azimuthal cuts

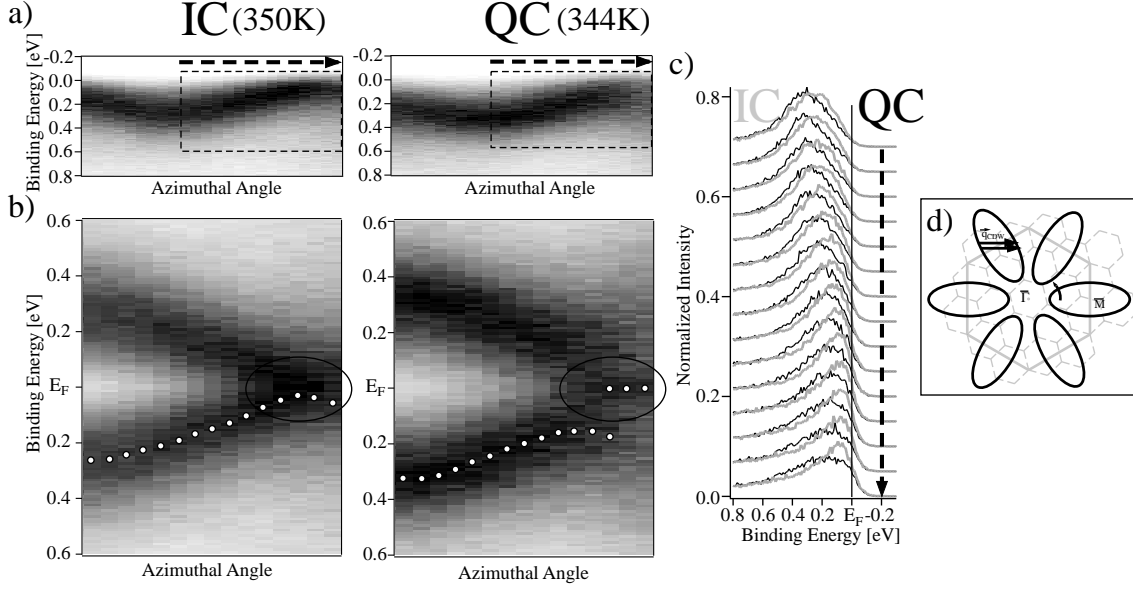


Figure 3.9: a) ARPES intensity maps measured along the azimuthal angle at a polar angle of 14° , for the IC and QC phases. b) Symmetrized plots of the zone delimited by the dashed rectangle on the maps of a). The corresponding location in the surface reciprocal space is shown by the curved arrow on the FS sketch in d). c) EDCs extracted from the maps plotted in a), in black for the QC phase and gray for the IC phase. The dashed arrow is located at the same position as the dashed arrows of a). d) The black ellipses represent a sketch of the FS where are also superimposed the (1×1) BZ and the $(\sqrt{13} \times \sqrt{13}) - R$ 13.9° BZ boundaries in continuous gray lines and dashed gray lines, respectively.

taken at a polar angle of 14° with respect to $\bar{\Gamma}$. The only visible band, near E_F , originates from Ta 5d electrons. In figure 3.9(b) these intensity plots are symmetrized with respect to the Fermi level and summed, in order [69, 70] to remove the perturbative effect of the Fermi-Dirac distribution cutoff and to infer whether the spectral function peak crosses the chemical potential or not. Figure 3.9(c) shows the energy distribution curves (EDCs) corresponding to the intensity plots shown in figure 3.9(a). In figure 3.9(d) a sketch of the FS contours is drawn, together with a superposition of the normal- and commensurate-state BZs. The curved arrow indicates the location of the intensity plots of figure 3.9(a). The presumed nesting vector \mathbf{q}_{CDW} is also drawn according to the calculation of $\Im\chi(\mathbf{q})$, connecting flat parts of the elliptically shaped FS with large, possibly nested (parallel) portions which have strongly turned the discussion of the origin of the CDW towards the nesting scenario.

In the following strong similarities with figure 3.8 become evident giving good reasons for a polaron scenario. Experimentally, large parts of the FS have been investigated (not shown) and we do not observe a different behaviour than that shown in figure 3.9 and described next.

In the IC phase (figures 3.9(a) and (b), left) a broad Ta 5d band flattens and narrows slightly when approaching E_F , giving rise to a small maximum centred at E_F in the symmetrized plot. In a standard interpretation of the symmetrization procedure this would be attributed to a Fermi level crossing of the quasiparticle peak. However, band calculations predict a linear slope through E_F and no flattening as observed. Moreover within the Fermi-liquid picture ARPES peaks are attributed to quasiparticle excitations whose lifetime increases when approaching E_F . However, in our case the Ta 5d peak remains anomalously broad near E_F . Thus we are clearly in the presence of a renormalized band which touches E_F without clearly crossing it.

An enhancement of the previous anomalies can be observed upon cooling down to the QC

phase (figure 3.9(c)). The line shape gets abruptly broader (when lowering T by only 6 K), the centre of mass of the Ta 5d band shifts towards higher binding energy when approaching the Fermi vector and becomes clearly separated from a small maximum visible in the symmetrized plot (figure 3.9(b), right). This symmetrization peak originates from a finite spectral weight near E_F . As described above, Bovet et al. [19] attributed this to a reconstruction induced band coming from above and merely straddling E_F . In the polaron picture proposed here, this finite intensity near E_F is also compatible with a remnant weight of the coherent quasiparticle (figure 3.8) [67].

The changes between the photoemission spectra of the IC and QC phases are abrupt and are interpreted as a change of the electron-phonon interaction character. Indeed, in 2D or 3D systems there is a qualitative dependence of the polaron type (large or small) on the range of the electron-lattice interaction [71]. While large polarons are formed if the electron-lattice interaction due to the long range Coulombic interaction between electronic carriers and lattice ions is of predominant importance, small polarons form if the short range electron-lattice interaction such as the deformation potential interaction dominates. The formation of the commensurate domains in the QC phase introduces, as shown above, the "Stars-of-David" which can be identified with small molecules acting as potential wells and hence favouring the short range interaction. Moreover, it has been noted [71] that the presence of long-range interaction eases the requirements for forming small polarons. Therefore, the CDW in the IC phase leads to a static deformation of the whole lattice structure which, in turn, leads to a more local character of the electron-lattice interaction and an enhancement of the electron-phonon coupling strength, i.e, to a lattice distortion enhanced electron-phonon coupling.

For the TaSe₂ and NbTe₂ it is likely that the situation is similar although a detailed analysis has not been made. Inspecting the spectra in figure 3.4 reveals a very similar behavior of broad peaks approaching E_F without crossing it together with spectral weight at E_F responsible for the FSMs being in good agreement with DFT calculations reproducing the image of the bare dispersion. For TiSe₂ and TiTe₂, however, the scenario appears to be very different. Sharp quasiparticle peaks are clearly crossing E_F . For TiTe₂, the FL prototype, this is understandable, but TiSe₂ undergoes a CDW transition and the mechanism for the system to gain electronic energy is under debate [72–74].

3.2.5 Conclusion and outlook

In summary, we have discussed a series of transition metal dichalcogenides related to the $1T$ structure, therefore having similar crystallographic and electronic structures. We have observed a distinctly different behavior between the compounds with, according to the ionic picture, nominally one and zero d electrons in the lowest occupied d band.

The d^1 compounds all show a very similar behavior as observed with ARPES and all present lattice distortions deviating from the $1T$ structure. The ARPES intensity distribution at E_F is well described by the single particle or DFT based band structure obtained for the un-reconstructed $1T$ structure. However closer examination shows that there are no quasiparticle peaks crossing E_F such that the FS appears pseudogapped. Two explanations have been put forward.

The first is based on DFT calculations for the distorted structure taking into account the many new sub-bands (Umklapp bands) producing electronic states all over the normal state BZ with most of the ARPES spectral weight along the bands of the un-reconstructed structure. In this scenario, the unusual energy broadening of bands may be explained by the contribution of many (experimentally unresolved and energetically close) sub-bands.

The second explanation is inspired by the peak shape of dispersing features being particularly large. A spectral function based on polaron formation has all the attributes to explain the experimental observations. In fact, electron-phonon coupling dresses the quasiparticles with lattice

vibration excitations leading to a broadened and re-normalized line shape resembling strongly the experimental observation.

The d^0 compounds are very different. Sharp quasiparticle peaks are observed the FS is not pseudogapped. However, whereas one of the compounds behaves Fermi-liquid like, the other undergoes a CDW transition. It is not clear presently what mechanism is responsible for the instability. It is certain that a delicate balance between interactions of the chalcogen sp electrons with the transition metal d electrons, their mobility and screening power together with the reaction of the lattice determine the amazing properties of these materials.

The calculated d^1 material's Fermi surfaces are all similar in shape and resemble an ellipse with rather flat parts that are susceptible for FS nesting. In order to investigate FS nesting as driving mechanism for the lattice distortion the imaginary part of the static electronic susceptibility has been calculated. The case for FS nesting is rather clear for NbTe₂ since phonon calculations also display a respective softening. It can, however, not be generalized for the others. In particular, the situation is more complicated for TaS₂.

An important conclusion is that from the present point of view we cannot distinguish between the two explanations for the behavior of the "one electron" compounds, i.e. single particles with many sub-band, versus polarons. The interpretation is not unique. It is necessary to refine the analysis to find unique differences. More accurate simulations are necessary in the future, in the sense of not only modeling the physics of the N-electron system but including photoemission matrix elements for a quantitative comparison. This would remove ambiguities related first, to strong versus weak spectral weight and second, to initial state (physics, spectral function) related versus final state (experiment specific, geometry) related broadening.

Acknowledgements

Skillful technical assistance was provided by the Neuchâtel mechanics and electronics workshops. Many helpful discussions with H. Beck are gratefully acknowledged. This project has been supported by the Fonds National Suisse de la Recherche Scientifique.

References for chapter 3

- [1] D. S. Dessau, T. Saitoh, C.-H. Park, Z.-X. Shen, P. Vilella, N. Hamada, Y. Moritomo and Y. Tokura, *J. Superconductivity* **12**, 273 (1999).
- [2] A. Lanzara, P. V. Bogdanov, X. J. Zhou, S. A. Kellar, D. L. Feng, E. D. Lu, T. Yoshida, H. Eisaki, A. Fujimori, K. Koshio, J.-L. Shimoyama, T. Noda, S. Uchida, Z. Hussain and Z.-X. Shen, *Nature* **412**, 510 (2001).
- [3] M.-H. Whangbo and E. Canadell, *J. Am. Chem. Soc* **114**, 9587 (1992).
- [4] B. E. Brown, *Acta Cryst.* **20**, 264 (1966).
- [5] C. Battaglia, H. Cercellier, F. Clerc, L. Despont, M. G. Garnier, C. Koitzsch, P. Aebi, H. Berger, L. Forrò, and C. Ambrosch-Draxl, *Phys. Rev. B* **72**, 195114 (2005).
- [6] M. H. van Maaren and G. M. Schaeffer, *Phys. Lett. A* **24**, 645 (1967).
- [7] J. van Landuyt, G. van Tendeloo and S. Amelinckx, *Phys. Stat. Sol.* **26**, 585 (1974).
- [8] J. van Landuyt, G. van Tendeloo and S. Amelinckx, *Phys. Stat. Sol.* **29**, K11 (1975).
- [9] J. A. Wilson, *Phys. Rev. B* **17**, 3880 (1978).
- [10] F. Lévy, *J. Phys. C* **12**, 3725 (1979).
- [11] F. J. Di Salvo, D. E. Moncton and J. V. Waszczak, *Phys. Rev. B* **14**, 4321 (1976).
- [12] Th. Pillo, J. Hayoz, H. Berger, M. Grioni, L. Schlapbach, and P. Aebi, *Phys. Rev. Lett.* **83**, 3494 (1999).
- [13] P. Aebi, Th. Pillo, H. Berger and F. Lévy, *J. Electron Spectrosc. Relat. Phenom.* **117-118**, 433 (2001).
- [14] Th. Pillo, J. Hayoz, D. Naumovic, H. Berger, L. Perfetti, L. Gavioli, A. Taleb-Ibrahimi, L. Schlapbach and P. Aebi, *Phys. Rev. B* **64**, 245105 (2001).
- [15] Th. Pillo, J. Hayoz, H. Berger, R. Fasel, L. Schlapbach and P. Aebi, *Phys. Rev. B* **62**, 4277 (2000).
- [16] K. Horiba, K. Ono, J. H. Oh, T. Kihara, S. Nakazono, M. Oshima, O. Shiino, H. W. Yeom, A. Kakizaki and Y. Aiura *Phys. Rev. B* **66**, 073106 (2002).
- [17] L. Perfetti, A. Georges, S. Florens, S. Biermann, S. Mitrovic, H. Berger, Y. Tomm, H. Höchst and M. Grioni, *Phys. Rev. Lett.* **90**, 166401 (2003).
- [18] M. Bovet, S. van Smaalen, H. Berger, R. Gaal, L. Forro, L. Schlapbach, and P. Aebi, *Phys. Rev. B* **67**, 125105 (2003).
- [19] M. Bovet, D. Popović, F. Clerc, C. Koitzsch, U. Probst, E. Busher, H. Berger, D. Naumović and P. Aebi, *Phys. Rev. B* **69**, 125117 (2004).
- [20] F. Clerc, M. Bovet, H. Berger, L. Despont, C. Koitzsch and P. Aebi, *Physica B* **351**, 245 (2004).

- [21] F. Clerc, M. Bovet, H. Berger, L. Despont, C. Koitzsch, O. Gallus, L. Patthey, M. Shi, J. Krempasky, M. G. Garnier and P. Aebi, *J. Phys. Cond. Mat.* **16**, 3271 (2004).
- [22] S. Colonna, F. Ronci, A. Cricenti, L. Perfetti, H. Berger and M. Grioni, *Phys. Rev. Lett.* **94**, 036405 (2005).
- [23] L. Perfetti, T. A. Gloor, F. Mila, H. Berger and M. Grioni, *Phys. Rev. B* **71**, 153101 (2005).
- [24] R. Leckey, private communication.
- [25] A. Bansil, M. Lindroos, S. Sahrakorpi and R. S. Markiewicz, *Phys. Rev. B* **71**, 012503 (2005).
- [26] A. Santoni, L. J. Terminello, F. J. Himpsel and T. Takahashi, *Appl. Phys. A* **52**, 229 (1991).
- [27] J. Osterwalder, T. Greber, A. Stuck and L. Schlapbach, *Phys. Rev. B* **44**, 13764 (1991).
- [28] D. Naumović, A. Stuck, T. Greber, J. Osterwalder and L. Schlapbach, *Phys. Rev. B* **47**, 7462 (1993).
- [29] J. Osterwalder, A. Stuck, T. Greber, P. Aebi, L. Schlapbach and S. Hüfner, *Vacuum ultraviolet radiation physics, proc. 10th vuv conference*, 475 (1993).
- [30] P. Aebi, J. Osterwalder, R. Fasel, D. Naumović and L. Schlapbach, *Surf. Sci.* **307**, 917 (1994).
- [31] P. Aebi, J. Osterwalder, P. Schwaller, L. Schlapbach, M. Shimoda, T. Mochiku and K. Kadowaki, *Phys. Rev. Lett.* **72**, 2757 (1994).
- [32] Th. Straub, R. Claessen, P. Steiner, S. Hüfner, V. Eyert, K. Friemelt and E. Bucher, *Phys. Rev. B* **55**, 13473 (1997).
- [33] T. J. Kreutz, P. Aebi and J. Osterwalder, *Solid State Commun* **96**, 339 (1995).
- [34] T. J. Kreutz, P. Aebi, J. Osterwalder and L. Schlapbach, *J. Electron Spectrosc. Relat. Phenom.* **76**, 601 (1995).
- [35] P. Schwaller, P. Aebi, H. Berger, C. Beeli, J. Osterwalder and L. Schlapbach, *J. Electron Spectrosc. Relat. Phenom.* **76**, 127 (1995).
- [36] T. J. Kreutz, T. Greber, P. Aebi and J. Osterwalder, *Phys. Rev. B* **58**, 1300 (1998).
- [37] T. Valla, A. V. Fedorov, P. D. Johnson, B. O. Wells, S. L. Hulbert, Q. Li, G. D. Gu and N. Koshizuka, *Science* **285**, 2110 (1999).
- [38] P. Aebi, T. J. Kreutz, J. Osterwalder, R. Fasel, P. Schwaller and L. Schlapbach, *Phys. Rev. Lett.* **76**, 1150 (1996).
- [39] Th. Pillo, L. Patthey, E. Boschung, J. Hayoz, P. Aebi and L. Schlapbach, *J. Electron Spectrosc. Relat. Phenom.* **97**, 243 (1998).
- [40] J. P. Perdew, S. Burke and M. Ernzerhof, *Phys. Rev. Lett.* **77**, 3865 (1996).
- [41] Blaha P, Schwarz K and Luitz J *WIEN97 A Full Potential Linearized Augmented Plan Wave Package for Calculating Crystal Properties (Karlheinz Schwarz, Techn. Universitt Wien, Austria), 1999. ISBN 3-9501031-0-4*

- [42] X. Gonze, J.-M. Beuken, R. Caracas, F. Detraux, M. Fuchs, G.-M. Rignanese, L. Sindic, M. Verstaete, G. Zerah, F. Jollet, M. Torrent, A. Roy, M. Mikami, Ph. Ghosez, J.-Y. Raty and D. C. Allan, *Computational Materials Science* **25**, 478 (2002).
- [43] The ABINIT code is a common project of the Université Catholique de Louvain, Corning Incorporated, and other contributors (URL <http://www.abinit.org>).
- [44] C. Hartwigsen, S. Goedecker and J. Hutter, *Phys. Rev. B* **58**, 3641 (1998).
- [45] C. Ambrosch-Draxl and J. O. Sofo, *cond-mat/0402523* (2004).
- [46] X. Gonze, *Phys. Rev. B* **55**, 10337 (1997).
- [47] X. Gonze and C. Lee, *Phys. Rev. B* **55**, 10355 (1997).
- [48] A. Damascelli, Z.-X. Shen, and Z. Hussain, *Rev. Mod. Phys.* **75**, 473 (2003).
- [49] R. Claessen, R. O. Anderson, J. W. Allen, C. G. Olson, C. Janowitz, W. P. Ellis, S. Harm, M. Kalning, R. Manzke, and M. Skibowski, *Phys. Rev. Lett.* **69**, 808 (1992).
- [50] R. Claessen, R. O. Anderson, G.-H. Gweon, J. W. Allen, W. P. Ellis, C. Janowitz, C. G. Olson, Z.-X. Shen, V. Eyert, M. Skibowski, K. Friemelt, E. Bucher, and S. Hüfner, *Phys. Rev. B* **54**, 2453 (1996).
- [51] L. Perfetti, H. Berger, A. Reggiani, L. Degiorgi, H. Höchst, J. Voit, G. Margaritondo, and M. Grioni, *Phys. Rev. Lett.* **87**, 216404 (2001).
- [52] J. Voit, L. Perfetti, F. Zwick, H. Berger, G. Margaritondo, G. Grüner, H. Höchst, and M. Grioni, *Science* **290**, 501 (2000).
- [53] P. Fazekas and E. Tosatti, *Phil. Mag. B* **39**, 229 (1979).
- [54] P. Fazekas and E. Tosatti, *Physica B* **99**, 183 (1980).
- [55] F. Clerc, *et al.*, *Phys. Rev. B* submitted (2006).
- [56] R. E. Peierls, *Quantum Theory of Solids* (Oxford University Press, Oxford, 1955).
- [57] G. Grüner, *Density Waves in Solids* (Addison-Wesley, Massachusetts, 1994).
- [58] M. D. Johannes, I. I. Mazin, and C. A. Howells, *cond-mat/0510390* (2005).
- [59] C. Koitzsch, J. Hayoz, M. Bovet, F. Clerc, L. Despont, C. Ambrosch-Draxl and P. Aebi, *Phys. Rev. B* **70**, 165114 (2004).
- [60] H. W. Myron, J. Rath, and A. J. Freeman, *Phys. Rev. B* **15**, 885 (1977).
- [61] J. A. Wilson, *Phys. Rev. B* **17**, 3880 (1978).
- [62] G. Ackland, *RIKEN review* **29**, 34 (2000).
- [63] L. Perfetti, S. Mitrovic, G. Margaritondo, M. Grioni, L. Forró, L. Degiorgi, and H. Höchst, *Phys. Rev. B* **66**, 075107 (2002).
- [64] L. Landau, *Z. Phys.* **3**, 664 (1933).

- [65] T. Holstein, *Ann.Phys.* **8**, 325 (1959).
 - [66] H. Fröhlich, *Adv.Phys.* **3**, 325 (1954).
 - [67] M. Hohenadler, D. Neuber, W. von der Linden, G. Wellein, J. Loos, and H. Fehske, *Phys. Rev. B* **71**, 245111 (2005).
 - [68] G. D. Mahan, *Many-Particle Physics*(Plenum Press, New York, 1981)
 - [69] M. R. Norman, H. Ding, M. Randeria, J. C. Campuzano, T. Yokoya, T. Takeuchi, T. Takahashi, T. Mochiku, K. Kadowaki, P. Guptasarma, and D. G. Hinks, *Nature* **392**, 157 (1998).
 - [70] J. Mesot, M. Randeria, M. R. Norman, A. Kaminski, H. M. Fretwell, J. C. Campuzano, H. Ding, T. Takeuchi, T. Sato, T. Yokoya, T. Takahashi, I. Chong, T. Terashima, M. Takano, T. Mochiku, and K. Kadowaki, *Phys. Rev. B* **63**, 224516 (2001).
 - [71] D. Emin, *Phys. Rev. B* **48**, 13691 (1993).
 - [72] Th. Pillo, J. Hayoz, H. Berger, R. Fasel, L. Schlapbach and P. Aebi, *Phys. Rev. B* **61**, 16213 (2000).
 - [73] T. E. Kidd, T. Miller, M. Y. Chou and T.-C. Chiang, *Phys. Rev. Lett* **88**, 226402 (2002).
 - [74] K. Rossnagel, L. Kipp and M. Skibowski, *Phys. Rev. B* **65**, 235101 (2002).
-

Chapter 4

On the search for the CDW origin in $1T\text{-TaS}_2$

4.1 Introduction

Among the many phase transitions occurring in low dimensions, the charge density waves, first discussed theoretically by Fröhlich in 1954 and by Peierls in 1955 [1], play an important role. Peierls, in his famous book *The quantum Theory of Solids*, described how a one dimensional metal becomes unstable with respect to a spatially modulated perturbation with wave vector \mathbf{q}_{CDW} equals to two times the Fermi wave vector \mathbf{k}_{F} . This leads to the formation of electron-hole pairs with the same wave vector and finally to the opening of a gap which provides a gain in electronic energy in order to compensate the elastic energy paid for the lattice distortion. It was recognized early that the driving force for such an instability is given by the topology of the Fermi surface (FS) which has to present favourable nesting conditions, namely large portions of the FS that can be connected or nested by the vector \mathbf{q}_{CDW} . The nesting condition is perfect in ideally one-dimensional systems, the FS being composed of two points separated by $2\mathbf{k}_{\text{F}}$. Not surprisingly, experimental evidence for these broken symmetry states was found much later with the availability of new quasi one-dimensional materials with linear chain structures and metallic properties.

The occurrence of CDWs in other than quasi-one-dimensional systems was first experimentally demonstrated by Wilson with diffraction experiments on the $1T\text{-TaS}_2$ and $1T\text{-TaSe}_2$. As discussed in chapter 3, the $1T\text{-TaS}_2$ is a quasi-two-dimensional material with a quite complex phase diagram as a function of temperature. On the contrary of 1D, the FS of 2D materials is not perfectly nested making questionable if the mechanisms behind CDW formation in 2D are the same than in 1D. At first the flat parts of the elliptically shaped FS of the $1T\text{-TaS}_2$ with parallel areas spanned by a vector of the order of the \mathbf{q}_{CDW} appear to be in favour of the nesting scenario as in 1D. However a closer analysis of the CDW induced new BZ and the possible energy balance between elastic deformation energy and electronic energy points to a more complicate scenario. Moreover with the improvement on the experimental side, notably of the energy and momentum resolution of ARPES instruments, new peculiar spectral features are revealed which are not fully consistent with the standard Peierls scenario for the formation of a CDW.

In this chapter, we discuss the origin of the CDW in the layered transition metal dichalcogenide $1T\text{-TaS}_2$ and we confront our experimental results with the expected standard Peierls mechanism. The chapter is organized as follows. In section 4.2 we review the basic theory behind CDW in a one-dimensional metal. Its generalization to 2D materials with quasi-one-dimensional character is presented in section 4.3 as well as a first analysis of the CDW formation in $1T\text{-TaS}_2$, which points to a more complicated mechanism than the standard nesting one. In section 4.4 a detailed analysis of the $1T\text{-TaS}_2$ as a function of temperature is shown. We present ARPES measurements for the three phases of the CDW in $1T\text{-TaS}_2$ (IC, QC, and C phases) and we introduce the possible influence of strong electron-phonon coupling in the interpretation of our data, as well as at the origin of the CDW in this compound. Finally general conclusions are given in section 4.6.

4.2 CDW theory in a one-dimensional metal

This section presents the basic theory behind the existence of a CDW ground state. For more complete information, the reader is referred to the large literature existing on the subject, especially Gruner [2], Berlinsky [3] and Kagoshima [4].

We begin by presenting in subsection 4.2.1 how a linear metallic chain of atoms can lower its energy by distorting its structure. In subsection 4.2.2, using linear response theory, we introduce the notion of susceptibility or response function, which is the key parameter to understand the instability of a one dimensional metal under a spatially modulated perturbation. Then in the last subsection 4.2.3 we discuss the electron-phonon interaction and see how this interaction, coupled to a finite susceptibility, can lead in 1D to a strongly renormalized phonon spectrum, generally referred to as the Kohn anomaly [5].

4.2.1 Peierls transition and energy balance

The influence on the electronic band dispersion of a static periodic ionic potential, in absence of electron-electron or electron-phonon interaction, is well known. This leads, within a nearly free electron model, to a gap opening at the BZ boundaries. This approach is evidently very crude, even at zero temperature, since the periodic ion array may (dynamically) respond to the presence of the electrons. Peierls pointed out that if one includes any interaction between the electrons and the phonons, it is energetically favourable to introduce a periodic lattice distortion with a period related to the Fermi wave vector \mathbf{k}_F by $\lambda = \pi/k_F$.

To illustrate this phenomenon, we consider a one dimensional metal with lattice constant a and at temperature $T = 0$ K. Fig. 4.1 (a) shows the situation in absence of electron-phonon coupling. The ground state is constructed by filling the electronic states up to the Fermi level E_F . A periodic lattice distortion with wave vector $2\mathbf{k}_F$ is described by

$$u = u_{2\mathbf{k}_F} \cos(2\mathbf{k}_F \mathbf{x}), \quad (4.1)$$

where u is the displacement of the atoms from their equilibrium position. The introduction of such a modulation, considered as static for simplicity, gives rise to a potential

$$V = V_{2\mathbf{k}_F} \cos(2\mathbf{k}_F \mathbf{x}), \quad (4.2)$$

which acts on the electrons. $V_{2\mathbf{k}_F}$ is equal $g \cdot u$, g representing the strength of the electron-phonon coupling.

Similarly to the nearly free electron theory of metals, the distorted potential has matrix elements connecting states with wave vector distant by $2k_F$, leading to the opening of band gaps at $\mathbf{k} = \pm\mathbf{k}_F$ in the conduction band of electrons, as illustrated in Fig 4.1(b). This modification of the dispersion relation leads to a change of the charge density which is a periodic function of the position \mathbf{x} :

$$\rho(\mathbf{x}) = \rho_0 [1 + \cos(2\mathbf{k}_F \mathbf{x} + \varphi)] \quad (4.3)$$

The next step is the evaluation of the change in energy induced by the distortion. Due to the opening of a gap at $\mathbf{k} = \pm\mathbf{k}_F$ the electron bands lying below and above E_F are bent downward and upward at $\mathbf{k} = \pm\mathbf{k}_F$, respectively. At $T = 0$ K only states below the gap are occupied, leading therefore to a decrease of the electronic energy. The perturbed energy can be calculated as follows:

$$E_{\mathbf{k}}^{\pm} = \frac{1}{2}(E_{\mathbf{k}}^0 + E_{\mathbf{k}+2\mathbf{k}_F}^0) \pm \frac{1}{2}\sqrt{(E_{\mathbf{k}}^0 - E_{\mathbf{k}+2\mathbf{k}_F}^0)^2 + 4 |V_{2\mathbf{k}_F}|^2}. \quad (4.4)$$

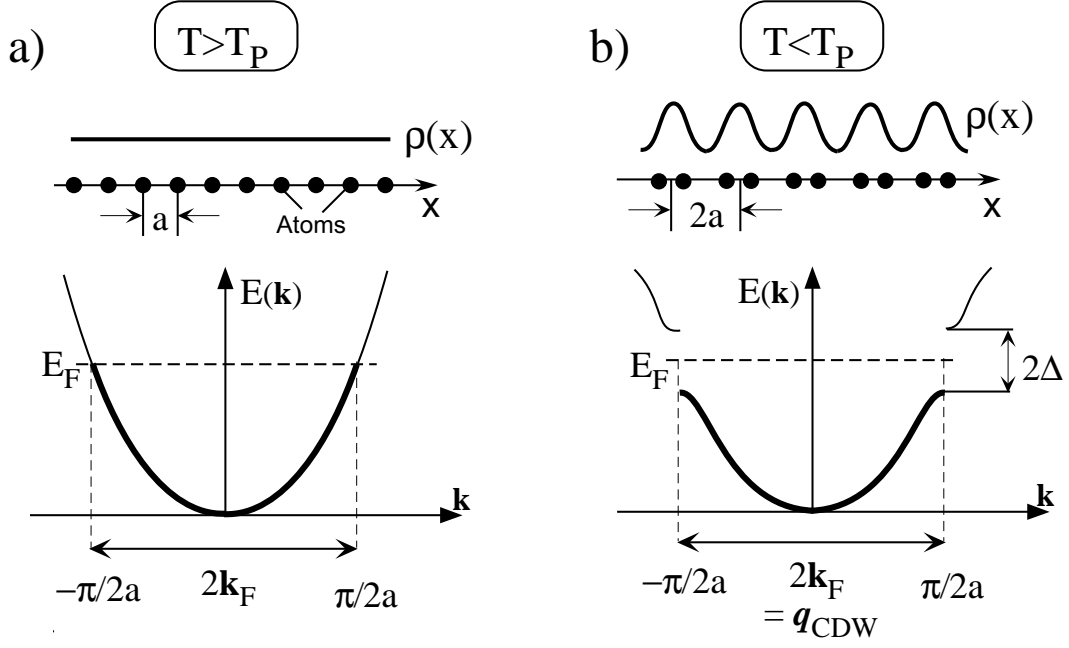


Figure 4.1: The Peierls transition in a one dimensional electron system with a half filled band. (a) Undistorted metal. (b) The doubling of the periodicity in real space halves the Brillouin zone in k -space. A gap opens at the new Brillouin zone boundaries leading to the Peierls insulating state.

$E_{\mathbf{k}}^0$ and $E_{2\mathbf{k}_F}^0$ are the unperturbed energies and the sign \pm denotes the upper and lower bands. At finite temperature the change in the electronic energy is thus:

$$\delta E = \sum_{\mathbf{k}} E_{\mathbf{k}}^{\pm} f(E_{\mathbf{k}}^{\pm}) - \sum_{\mathbf{k}} E_{\mathbf{k}}^0 f(E_{\mathbf{k}}^0). \quad (4.5)$$

Assuming $V_{2\mathbf{k}_F} \ll E_F$, one obtains

$$\begin{aligned} \delta E &= - |V_{2\mathbf{k}_F}|^2 N \sum_{\mathbf{k}} \frac{f(E_{\mathbf{k}+2\mathbf{k}_F}^0) - f(E_{\mathbf{k}}^0)}{E_{\mathbf{k}}^0 - E_{\mathbf{k}+2\mathbf{k}_F}^0} \\ &= - |V_{2\mathbf{k}_F}|^2 N \chi^{\circ}(2\mathbf{k}_F), \end{aligned} \quad (4.6)$$

where we have already introduced the bare susceptibility $\chi^{\circ}(2\mathbf{k}_F)$, that will be discussed in more details in the next subsection.

The periodic lattice distortion costs also some elastic energy, that corresponds to an increase of the strain energy by an amount of

$$\delta U = \frac{1}{2} c u_{2\mathbf{k}_F}^2, \quad (4.7)$$

where c is the elastic spring constant of the lattice. Finally the change of the total energy of electrons and lattice system is

$$\delta E + \delta U = - |V_{2\mathbf{k}_F}|^2 N \chi^{\circ}(2\mathbf{k}_F) + \frac{c}{2} u_{2\mathbf{k}_F}^2, \quad (4.8)$$

and with the band gap $2\Delta = 2 |V_{2\mathbf{k}_F}| = 2g |u_{2\mathbf{k}_F}|$, we obtain

$$\delta E + \delta U = -\Delta^2 [N \chi^{\circ}(2\mathbf{k}_F) - \frac{c}{2g^2}]. \quad (4.9)$$

In the next subsection, we will show that $\chi^{\circ}(\mathbf{q})$ diverges logarithmically for $\mathbf{q} \rightarrow 2\mathbf{k}_F$ and $T \rightarrow 0$. Therefore $\delta E + \delta U$ becomes negative below a certain temperature T_P and the lattice distortion,

called the Peierls instability, takes place whenever g is finite, leading to a gap opening at E_F and to an insulating state. This metal-insulator transition is called a Peierls transition. An expression for T_P can be derived on the basis of a mean field approximation and is given as [2]

$$2\Delta = 3.52k_B T_P. \quad (4.10)$$

The disappearance of the gap at $T > T_P$ is due to thermally excited electrons which cross the gap and screen the electron-phonon interaction and hence reduce the size of Δ .

We note here that the periodicity of the modulation is given by the position of the Fermi wave vector, \mathbf{k}_F , and thus by the band filling which leads in general to a CDW incommensurate with the underlying lattice i.e. λ/a is irrational in the general case.

4.2.2 Linear response theory and generalized susceptibility

We examine here the response of a non-interacting electrons system to a weak external perturbative potential and treat it in the framework of linear response theory.

To keep generality, we first consider a many-particle system described by the Hamiltonian H and coupled to an external source field $\lambda(\mathbf{r})$ via an internal variable O of the system. This coupling leads to the following perturbative term

$$H_{ext} = \int d^3\mathbf{r} \lambda(\mathbf{r}) O(\mathbf{r}) \quad (4.11)$$

$O(\mathbf{r})$ is a hermitian operator and $\lambda(\mathbf{r})$ is real. The response of the system to H_{ext} is reflected by a change of O . The expectation value of $O(\mathbf{r})$ is defined as

$$\langle O(\mathbf{r}) \rangle = \frac{\langle \psi_0 | O(\mathbf{r}) | \psi_0 \rangle}{\langle \psi_0 | \psi_0 \rangle} \quad (4.12)$$

where $|\psi_0\rangle$ is the ground state of the system in the presence of the external field. We assume that this true ground state can be generated from the ground state $|\phi_0\rangle$ of the Hamiltonian without the perturbative term by adiabatically switching the interaction. To the first order in λ we obtain

$$\begin{aligned} \langle O(\mathbf{r}) \rangle &= \\ & \langle \phi_0 | O(\mathbf{r}) | \phi_0 \rangle - \lim_{\eta \rightarrow 0} \frac{i}{\hbar} \int d^3\mathbf{r}' \lambda(\mathbf{r}') \\ & \int_{-\infty}^0 dt' e^{\eta t'} \langle \phi_0 | [O(\mathbf{r}), O(\mathbf{r}', t')] | \phi_0 \rangle \end{aligned} \quad (4.13)$$

where $\langle \phi_0 | O(\mathbf{r}) | \phi_0 \rangle$ represents the expectation value of O before switching on the external field, and the exponential factor $e^{\eta t}$ with $\eta > 0$ guarantees that for $t \rightarrow -\infty$ the system is in its unperturbed state. $O(\mathbf{r}, t) = e^{\frac{i}{\hbar} H t} O(\mathbf{r}) e^{-\frac{i}{\hbar} H t}$ is the time dependent operator in the Heisenberg representation. The expectation value of the change of O induced by the perturbation $\lambda(\mathbf{r})$ is finally given by

$$\begin{aligned} \langle \delta O(\mathbf{r}) \rangle &= \langle O \rangle - \langle \phi_0 | O(\mathbf{r}) | \phi_0 \rangle \\ &= \lim_{\eta \rightarrow 0} \int d^3\mathbf{r}' \lambda(\mathbf{r}') \int_{-\infty}^{\infty} dt' e^{\eta |t'|} \chi(\mathbf{r}, \mathbf{r}'; 0, t') \end{aligned} \quad (4.14)$$

where we have introduced the retarded response function, also called generalized susceptibility, defined as

$$\chi(\mathbf{r}, \mathbf{r}'; t, t') = -\frac{i}{\hbar} \vartheta(t - t') \langle \phi_0 | [O(\mathbf{r}, t), O(\mathbf{r}', t')] | \phi_0 \rangle \quad (4.15)$$

As can be seen by looking at our introduction to the Green's function formalism in chapter 2, this expression has the form of a retarded Green's function. The Fourier transform of Eq. 4.14 gives

$$\langle \delta O(\mathbf{q}, \omega) \rangle = \chi(\mathbf{q}, \omega) \lambda(\mathbf{q}) \quad (4.16)$$

This means that the linear response of a system to an external potential is described in terms of a retarded Green's function.

We can use the above formalism to describe the rearrangement of the charge density $\rho(\mathbf{r})$ of a free electron system in response to an external electrostatic potential Φ_{ext} , which could result, for example, from a positively charged particle placed at a fixed position. In the homogeneous electron gas the particle density operator for zero wavenumber has an expectation value of zero unless there is a perturbation of the system, that causes a polarization of the electron system. As shown in the linear screening model and assuming that the electrons respond to the total potential $\Phi(\mathbf{r})$, the induced change of $\rho(\mathbf{r})$ is related to $\Phi(\mathbf{r})$, by analogy to (4.16), through

$$\langle \delta \rho^{ind}(\mathbf{q}) \rangle = \chi(\mathbf{q}, \omega) \Phi(\mathbf{q}). \quad (4.17)$$

In this case the proportionality term is described by the Fourier transform of the charge susceptibility

$$\chi^\circ(\mathbf{r} - \mathbf{r}', t - t') = -\frac{i}{\hbar} \vartheta(t - t') \langle \phi_0 | [\rho(\mathbf{r}, t), \rho(\mathbf{r}', t')] | \phi_0 \rangle. \quad (4.18)$$

Therefore according to (2.23) the Fourier transform can be written as $\chi^\circ(\mathbf{q}, \omega) = \ll \rho_{\mathbf{q}\omega} \rho_{\mathbf{q}\omega}^+ \gg_\omega^{ret}$ with $\rho_{\mathbf{k}} = \sum_{\mathbf{k}+\mathbf{q}} c_{\mathbf{k}+\mathbf{q}}^+ c_{\mathbf{k}}$ and thus represents a two particle Green's function describing the propagation of electron-hole pair with momentum \mathbf{q} . $\chi^\circ(\mathbf{q}, \omega)$ is easily calculated using the Green's function method :

$$\chi^\circ(\mathbf{q}, \omega) = \sum_{\mathbf{k}} \frac{f_{\mathbf{k}} - f_{\mathbf{k}+\mathbf{q}}}{\omega + \frac{1}{\hbar}(\epsilon(\mathbf{k}) - \epsilon(\mathbf{k} + \mathbf{q})) + i\eta}, \quad (4.19)$$

for the dynamic response and

$$\chi^\circ(\mathbf{q}, 0) = \sum_{\mathbf{k}} \frac{f_{\mathbf{k}} - f_{\mathbf{k}+\mathbf{q}}}{\epsilon(\mathbf{k}) - \epsilon(\mathbf{k} + \mathbf{q})}, \quad (4.20)$$

for the static limit. $f_{\mathbf{k}} = f(\epsilon_{\mathbf{k}})$ is the Fermi-Dirac distribution. This last expression for the response function is the bare susceptibility that we already used in (4.6).

In the 1D case and with a linear electronic dispersion relation near E_F , the bare susceptibility takes the following form:

$$\chi^\circ(\mathbf{q}) = -e^2 n(\epsilon_F) \ln \left| \frac{\mathbf{q} + 2\mathbf{k}_F}{\mathbf{q} - 2\mathbf{k}_F} \right|, \quad (4.21)$$

e is the elementary charge and $n(\epsilon_F)$ is the density of states at E_F . For small \mathbf{q} , it transforms into the Thomas-Fermi approximation, $\chi^\circ(\mathbf{q}) = -e^2 n(\epsilon_F)$ [6]. The logarithmic singularity at $2\mathbf{k}_F$ in (4.21) means that in 1D the electron gas is unstable against an external perturbation with period $\lambda = \pi/k_F$, which can consist in a charge or spin density wave. The response function for temperature $T = 0$ K is displayed for 1D, 2D and 3D in Fig. 4.2, where the singularity in 1D, which, according to (4.9), renders energetically favourable a lattice distortion, is obvious. In contrast in 2D and 3D there is only a jump and a divergence in the derivative of χ° at $2\mathbf{k}_F$. This different behaviour can be understood by considering the contributing terms in (4.20) and the

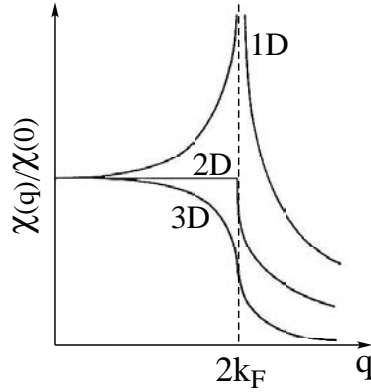


Figure 4.2: Response function at $T=0$ K in each dimension.

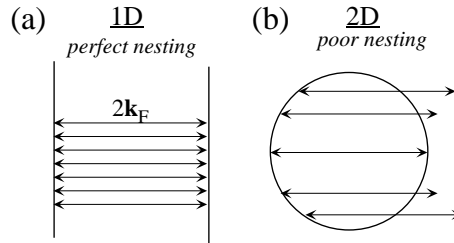


Figure 4.3: Topology of the Fermi surface for a 1D(a) and 2D(b) electron gas. The arrows connect pairs of states differing by the wavevector $\mathbf{q} = 2\mathbf{k}_F$.

topology of the FS. From (4.20) it is clear that one full and one empty state at the same energy, differing by $\mathbf{q} = 2\mathbf{k}_F$, give divergent contributions. In an ideal 1D case, as shown in Fig. 4.3 (a), the FS consists of perfectly parallel FS portions connected by $\mathbf{q} = 2\mathbf{k}_F$. This is called perfect nesting, meaning that every state of this 1D FS gives a divergent contribution to χ° . However in higher dimension the number of such states is significantly reduced as shown in Fig. 4.3 (b) for the 2D case. In the static limit, the strength of the response to an external perturbation depends strongly on the geometry of the FS.

4.2.3 Electron-phonon interaction and Kohn anomaly

The Kohn anomaly consists in a strong renormalization of the phonon spectrum at $\mathbf{q} = 2\mathbf{k}_F$ for 1D systems, due to the strong divergence in χ° described above and leading to a static deformation at $T = T_P$

The electron-phonon interaction gives rise to many effects, all of them playing a crucial role on the properties of many materials. Apart from the effects of the structural distortion discussed in this chapter, one can mention the formation of Cooper pairs which is the basis of conventional superconductivity, or the formation of polarons, which consist in charge carriers surrounded by the lattice distortions they induce (see complement 4.5.2).

The Hamiltonian describing the electron-phonon system is usually expressed within the formalism of second quantization. It can be written as [7]:

$$H = H_{el}^\circ + H_{ph}^\circ + H_{el-ph} \quad (4.22)$$

where

$$H_{el}^{\circ} = \sum_{\mathbf{k}} \epsilon_{\mathbf{k}} c_{\mathbf{k}}^{\dagger} c_{\mathbf{k}} \quad (4.23)$$

$$H_{ph}^{\circ} = \sum_{\mathbf{q}} \omega_{\mathbf{q}} b_{\mathbf{q}}^{\dagger} b_{\mathbf{q}} \quad (4.24)$$

$$H_{el-ph} = \frac{1}{\sqrt{N}} \sum_{\mathbf{k}, \mathbf{q}} g(\mathbf{k}, \mathbf{q}) (b_{-\mathbf{q}}^{\dagger} + b_{\mathbf{q}}) c_{\mathbf{k}+\mathbf{q}}^{\dagger} c_{\mathbf{k}} \quad (4.25)$$

For simplicity we have dropped the spin indices as well as the phonon polarization indices. $c_{\mathbf{k}}^{\dagger}$ ($c_{\mathbf{k}}$) and $b_{\mathbf{q}}^{\dagger}$ ($b_{\mathbf{q}}$) are electron and phonon creation (destruction) operators respectively, $\epsilon_{\mathbf{k}}$ is the unperturbed electron energy, $\omega_{\mathbf{q}}$ is the unperturbed phonon frequency, N is the number of lattice sites and $g(\mathbf{k}, \mathbf{q})$ describes the electron-phonon coupling. The term $g(\mathbf{q}) b_{\mathbf{q}} c_{\mathbf{k}+\mathbf{q}}^{\dagger} c_{\mathbf{k}}$ corresponds to the absorption of phonons by electrons and the term $g(\mathbf{q}) b_{-\mathbf{q}}^{\dagger} c_{\mathbf{k}+\mathbf{q}}^{\dagger} c_{\mathbf{k}}$ represents the emission of phonons by electrons. $g(\mathbf{k}, \mathbf{q})$ is simplified in $g(\mathbf{q})$ in two well known models: the Fröhlich model with $g(\mathbf{q}) \sim \frac{1}{q}$, which is established for a free or nearly free electron gas, and the Holstein model with $g(\mathbf{q}) = g = \text{cst}$ which is applicable if only the one-site energy in a tight-binding model is affected.

The modification of the phonon spectrum induced by the coupling of phonons with electrons may be calculated thanks to the one-phonon Green's function which is defined as

$$D(\mathbf{R}_i, t_1; \mathbf{R}_j, t_2) = -i \langle \phi_0 | T[\varphi_{\lambda}(\mathbf{R}_i, t_1), \varphi_{\lambda}(\mathbf{R}_j, t_2)] | \phi_0 \rangle \quad (4.26)$$

where $|\phi_0\rangle$ is the ground state and $\varphi_{\lambda}(\mathbf{R}) = \frac{1}{\sqrt{V}} \sum_{\mathbf{q}} (b_{-\mathbf{q}}^{\dagger} + b_{\mathbf{q}}) e^{i\mathbf{q}\mathbf{R}}$ is the field operator.

In the absence of coupling ($g=0$), the Hamiltonian of the system simplifies to H_{ph}° and the Fourier transform of the Green's function is easily calculated and results in*

$$D_{\circ}(\mathbf{q}, \omega) = \ll \varphi_{-\mathbf{q}}; \varphi_{\mathbf{q}} \gg_{\omega} = \frac{2\omega_{\mathbf{q}}}{\omega^2 - \omega_{\mathbf{q}}^2 + i\eta'} \quad (4.27)$$

where D_{\circ} is the unperturbed one-phonon Green's function.

The switching on of the electron-phonon interaction physically means that the electrons are allowed to follow the ion motion, or in other words, to screen the motion of the ions. This screening can be taken into account by considering that its effect would involve many electron-hole pairs. This results for the perturbed phonon Green function in the random phase approximation to the following diagrammatic representation:

The diagram shows the expansion of the perturbed phonon Green function. It starts with a wavy line labeled 'q'. This is followed by a plus sign and another wavy line labeled 'q'. Then, there is a plus sign and a wavy line labeled 'q' connected to a polarization bubble (a circle with a dot) labeled 'k', which is then connected to a wavy line labeled 'q'. This is followed by a plus sign and a similar term with two polarization bubbles, and so on.

where --- corresponds to the unperturbed one-phonon Green function D_{\circ} and --- is the polarization bubble $\Pi_{\circ} = \ll \rho_{\mathbf{q}}, \rho_{\mathbf{q}} \gg^{ret} = \sum_{\mathbf{k}} G_{\circ}^{(2)}(\mathbf{k}, \mathbf{q}, \omega) = \ll c_{\mathbf{k}}^{\dagger} c_{\mathbf{k}+\mathbf{q}}; c_{\mathbf{k}+\mathbf{q}}^{\dagger} c_{\mathbf{k}} \gg^{ret}$, where $G_{\circ}^{(2)}$ is the unperturbed electron-hole Green function. This polarization term Π_{\circ} is identical to the

* $\eta' = 2\omega\eta > 0$, with η an infinitesimal quantity added to ensure that the Fourier transform integral converge.

4.2. CDW theory in a one-dimensional metal

expression of the bare susceptibility χ° discussed in the precedent subsection (Eq. 4.18), as they both describe the propagation of electron-hole pairs.

The last diagrammatic representation may be rewritten using the Dyson equation

which in analytical form becomes

$$D(\mathbf{q}, \omega) = D_\circ(\mathbf{q}, \omega) + D_\circ(\mathbf{q}, \omega) \frac{|g|^2}{\hbar^2} \Pi_\circ(q) D(\mathbf{q}, \omega). \quad (4.28)$$

Using Eq. 4.27 we find

$$D(\mathbf{q}, \omega) = \frac{2\omega_{\mathbf{q}}}{\omega^2 - \omega_{\mathbf{q}}^2 + \frac{2\omega_{\mathbf{q}}|g|^2}{\hbar^2} \Pi_\circ}. \quad (4.29)$$

The perturbed phonon frequencies correspond to those values of ω for which the denominator of $D(\mathbf{q}, \omega)$ vanishes. Thus the renormalized phonon frequencies are

$$\omega_{\mathbf{q}}^{ren2} = \omega_{\mathbf{q}}^2 - 2\omega_{\mathbf{q}} \frac{|g|^2}{\hbar^2} \chi^\circ(\mathbf{q}, T) \leq \omega_{\mathbf{q}}^2. \quad (4.30)$$

As we know from subsection 4.2.2, for the case of 1D electrons system $\chi^\circ(\mathbf{q}, T)$ diverges logarithmically as $\mathbf{q} \rightarrow 2\mathbf{k}_F$ and $T \rightarrow 0$, thus the frequency $\omega_{2\mathbf{k}_F}^{ren}$ approaches 0 with decreasing temperature. Indeed in 1D the Kohn anomaly leads to a frozen phonon frequency at $\mathbf{q} = 2\mathbf{k}_F$ and thus to a static lattice distortion, while in 2D or 3D the anomaly is weaker as can be seen in Fig. 4.4.

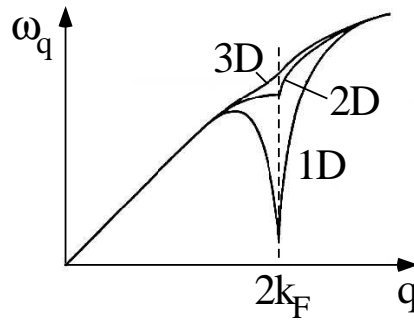


Figure 4.4: Kohn anomaly in the phonon spectrum for each dimensionality.

As already mentioned the temperature at which the $\omega_{2\mathbf{k}_F}^{ren}$ becomes zero is the Peierls transition temperature T_P . It can be shown that for the temperatures $T > T_P$ the renormalized phonon frequency obeys the following expression

$$\omega_{2\mathbf{k}_F}^{ren2} = \lambda \omega_{2\mathbf{k}_F}^2 \ln \frac{T}{T_P} \quad (4.31)$$

where λ is the dimensionless electron-phonon coupling. In summary for $T > T_P$ the phonon frequency at $2\mathbf{k}_F$ is progressively depressed by a factor $(\lambda \ln \frac{T}{T_P})^{\frac{1}{2}}$ until $T = T_P$ where the frequency

vanishes. This zero frequency leads to a static distortion of the lattice for $T \leq T_P$ and, as discussed in the two previous subsection, to the opening of a gap at $\pm\mathbf{k}_F$ rendering the material insulating. For completeness, we note that the Coulomb interaction can screen the coupling between electrons and phonons. If this effect is taken into account, in all the previous formula the bare susceptibility χ° has to be replaced by the generalized one

$$\chi = \frac{\chi^\circ}{1 + \frac{V}{\hbar}\chi^\circ} \quad (4.32)$$

where V represents the coulomb interaction.

4.3 CDW in 1T-TaS₂: An angle-resolved photoemission study

F. Clerc,¹ M. Bovet,¹ H. Berger,² L. Despont,¹ C. Koitzsch,¹ M. G. Garnier,¹ and P. Aebi¹

¹ *Institut de Physique, Université de Neuchâtel, CH-2000 Neuchâtel, Switzerland*

² *Institut de Physique Appliquée, EPFL, CH-1015 Lausanne, Switzerland*

Published in *PhysicaB* **351**, 245-249 (2004)

The transition metal dichalcogenide 1T-TaS₂ is a layered material exhibiting charge density waves. Based on angle-resolved photoemission experiments mapping spectral weight at the Fermi surface and density functional theory calculations we discuss possible mechanisms involved with the creation of charge density waves. At first the flat parts of the elliptically shaped Fermi surface appear to play an important role via Fermi surface nesting. A closer analysis of the charge density wave induced new Brillouin zones and the possible energy balance between elastic deformation energy and electronic energy points to a more complicated scenario.

Low dimensional systems have particularly attracted interest through the discovery of high temperature superconductors (HTCs). Many angle-resolved photoemission (ARPES) experiments have been conducted on such materials. With the improvement of the energy and momentum resolution on the experimental side, the interpretation has become very sophisticated and many unusual signatures in the spectral function have been found. Among them is the signature for the opening of a pseudogap, for a sort of collective mode (of unknown origin) and, very recently, for a spontaneous symmetry breaking of time reversal symmetry [8]. Also, stripes, i.e., doped holes that are self-organized, a sort of density waves, appear to play an important role. [9] Nevertheless, the final word about the mechanism behind HTC is not spoken. It is therefore important to relate these findings and apply the same sophistication in the analysis to other layered materials.

Layered transition metal dichalcogenides are a class of quasi two-dimensional (2D) materials. Many exhibit charge density waves (CDWs) and even become superconducting at low temperatures. Indeed there is renewed and growing activity on these materials. [10, 11] 1T-TaS₂ is such a material exhibiting CDW's and a quite complex phase diagram as a function of temperature [12, 13]. The studies on such materials serve a better understanding of the mechanisms at work in low dimensional electron systems in general.

In the present article we discuss the occurrence of CDWs in 1T-TaS₂. From ARPES and density functional theory (DFT) calculations we analyze the shape of the Fermi surface (FS) with respect to possible nesting and the arrangement of the new CDW induced Brillouin zones (BZs). We consider different possible ingredients in the energy balance governing the occurrence of the CDWs.

ARPES measurements have been done at room temperature (RT) in a modified VG ESCALAB Mk II spectrometer using monochromatized He I α ($h\nu = 21.2$ eV) photons. [14] The sequential motorized sample rotation has been outlined elsewhere. [15] The energy and angular resolution was 20 meV and $\pm 0.5^\circ$, respectively. Pure 1T-TaS₂ samples were prepared by vapor transport [16, 17] and cleaved *in situ* at pressures in the lower 10^{-10} mbar region. The accurate position of the Fermi level (E_F) has been determined on a polycrystalline copper sample. Cleanness and quality have been checked by x-ray photoelectron spectroscopy and by low energy electron diffraction (LEED), respectively. Well-defined LEED superspots confirmed the presence of the CDW-induced reconstruction. X-ray photoelectron diffraction was used to determine the sample orientation *in situ* with an accuracy of better than 0.5° .

Band structure calculations have been performed using the WIEN package implementing the FLAPW method within the framework of DFT. [18] For the exchange-correlation potential the generalized gradient approximation was used. [19] We considered the photoemission process in assuming a free electron final state without introduction of any matrix elements effects. [20]

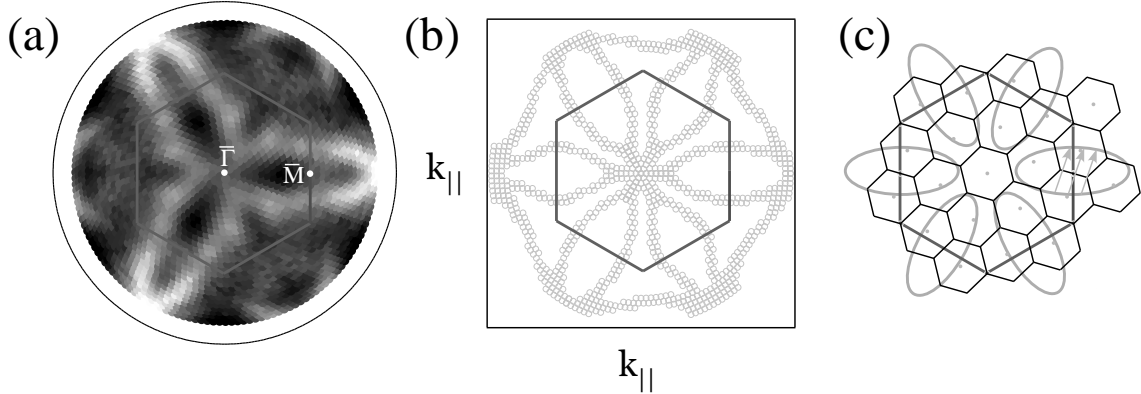


Figure 4.5: (a) Experimental Fermi energy intensity map taken with HeI radiation at room temperature, plotted linearly in k_{\parallel} ; high intensity is in white; center and outer circle correspond to normal and 90° emission, respectively; the hexagon represents the normal state BZ. (b) Corresponding density functional theory calculated map for the normal state. (c) Superposition of normal- and CDW-state BZs, together with a sketch of the FS contours; possible nesting vectors are plotted (see text).

Fig.4.5(a) displays the result of an E_F mapping experiment at RT. At RT the CDW is well established as seen in LEED (not shown) and consists of commensurate CDW domains of approximately 70Å in diameter [21, 22] with incommensurate regions in between. The RT phase is called the quasi-commensurate phase in contrast to the commensurate (“C”) phase below 180 K where no incommensurate regions exist anymore. The first order transition to the “C”-phase is accompanied by a jump in the resistivity of more than an order of magnitude (see e.g. ref [23]). 1T-TaS₂ in its unreconstructed or normal state consists of hexagonal Ta planes sandwiched between sulfur atoms. In the ionic picture Ta[Xe]4f¹⁴5d³6s² gives four of its five electrons to the two sulfur (S[Ne]3s²3p⁴) atoms creating a system with one d -electron per unit cell. Indeed, band structure calculations for the normal state [23] display a single Ta d -band dispersing close to E_F . The calculation for the E_F scan (Fig.4.5(b)) represents a cut through the FS and is in good agreement with the experiment (Fig. 4.5(a)). The BZ of the non-reconstructed structure is also drawn in Fig. 4.5(a). It is important to note that despite the presence of the CDW at RT, the experiment exhibits the symmetry of the normal state BZ, as is also evident from the good agreement of experiment (Fig. 4.5(a)) and normal state calculation (Fig. 4.5(b)). This observation has been discussed previously [23] and is a consequence of the spectral weight distribution, as measured by ARPES, remaining strongest along the bandstructure of the non-reconstructed phase. [24] The experiment only shows strong intensity for three of the six ellipses, a fact which has been attributed to the final state scattering of the outgoing photoelectron. [25]

Another important point to notice is that only a remnant FS is visible [26], i.e., the E_F map (Fig. 4.5(a)) does not actually represent the locations of quasiparticle peaks crossing E_F . As a matter of fact no clear crossing has been observed in ARPES data. A careful study of experimental data combined with bandstructure calculations *including* the lattice distortion concluded that the pseudogap can be explained by the splitting and backfolding of bands introduced by the new BZs. [27]

Figure 4.5(c) displays a sketch of the situation with both, the $(\sqrt{13} \times \sqrt{13}) - R$ 13.9° reconstructed (small hexagons) and the un-reconstructed BZs plotted. We have an elliptically shaped normal state FS with evidence for nested parts along the flat parts of the ellipses (see arrows in Fig. 4.5(c)). [28] The important question is what drives the CDW. Is it the classical Peierls transition as in 1D? If this is the case, what do we expect from a strongly nested quasi-1D FS? Fig. 4.6(a) displays the case of a strongly nested FS as indicated by arrows connecting nested (parallel) parts of the FS contour. One electron per atom (and unit cell) of chains of atoms with distance a is assumed. Therefore the Fermi vector $k_F = \pi/(2a)$ since the quasi-1D band is half filled. The BZ boundary is located at $2k_F = \pi/a$ (Fig. 4.6(a)). If the lattice is distorted in order to double the periodicity, i.e., to introduce a CDW with wave length $2a$, elastic energy has to be paid. At the same time a doubling of the periodicity in real space results in reducing the dimension of the BZ by a factor of two. The consequence is that the BZ boundary is now located at $k_F = \pi/(2a)$ and the band is full (two electrons per unit cell, due to the doubling of the periodicity) with the opening of a gap at the new BZ boundary at $\pi/(2a)$ and a corresponding gain of electronic energy. Therefore, what we expect from a strongly nested FS is that its nested parts disappear (due to the gap opening) with the occurrence of the CDW (Fig. 4.6(b)).

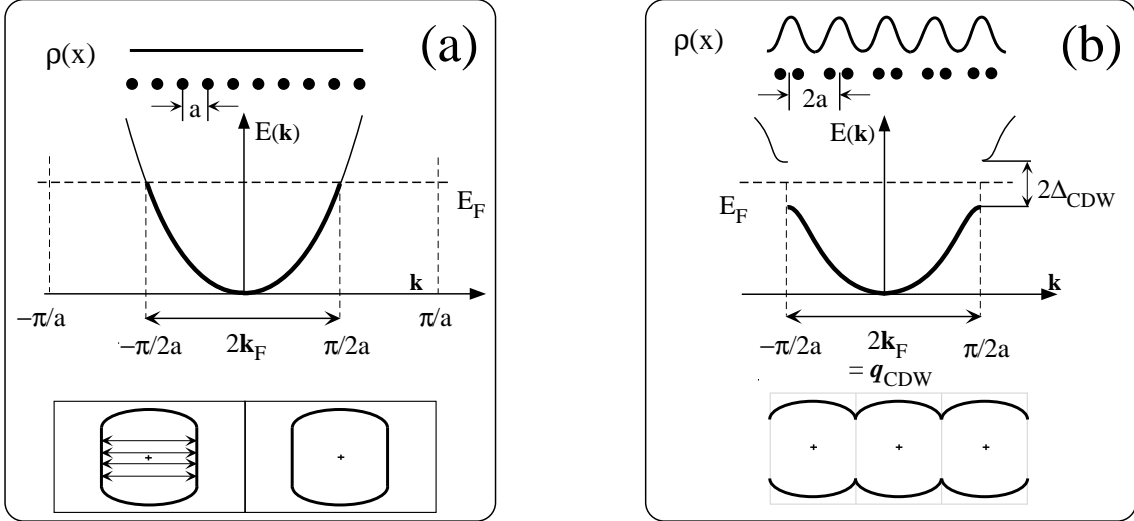


Figure 4.6: Sketch of the behavior of the bandstructure and Fermi surface contours of a quasi-1D system with one electron per unit cell (see text).

However, looking carefully at Fig. 4.5, this is not what we observe. The boundaries of the new BZs are not along the expected nested parts of the normal state FS (indicated by arrows in Fig. 4.5(c)) indicating that we do not have a quasi-1D system.

It is necessary to explore the ingredients of the energy balance of the transition. [4] The energy balance of elastic energy paid and electronic energy gained is expressed in terms of the susceptibility $\chi(\mathbf{q})$ (polarization function or Lindhard function), the elastic spring constant of the lattice, c , and the magnitude of the electron-lattice interactions g , to be $-\Delta_{CDW}^2 \cdot (N\chi(\mathbf{q}) - \frac{c}{g^2})$, where $-\Delta_{CDW}$ is half of the gap size and \mathbf{q} the wave vector of the lattice distortion. [4] The susceptibility (appearing in the electronic energy part) connects the charge response, $\rho(\mathbf{q})$, to a perturbation $V(\mathbf{q})$ (introduced by phonons) via $\rho(\mathbf{q}) = -\chi(\mathbf{q}) V(\mathbf{q})$. The susceptibility can be written as $\chi(\mathbf{q}) = \frac{1}{N} \sum_{\mathbf{k}} \frac{f_{\mathbf{k}+\mathbf{q}} - f_{\mathbf{k}}}{E_{\mathbf{k}} - E_{\mathbf{k}+\mathbf{q}}}$, where f and E express the Fermi-Dirac function and the energy eigenvalues at the given \mathbf{k} -vector, respectively. It is clear that only occupied and empty states very close to E_F separated by a vector \mathbf{q} contribute to the sum, which basically describes the FS nesting. This sum is strongly dependent on the dimensionality and it diverges in 1D. [4] It is

also a diverging susceptibility, together with the electron-phonon coupling, that leads to a phonon softening, finally observed in the static lattice deformation induced by the CDW.

What is the role of the susceptibility in the case of 1T-TaS₂? As seen from Fig. 4.5(c) it is not clear whether nesting is strong. A clear statement is not possible based on the present data since the system has not chosen to align the new BZs along potentially nested parts (flat parts of the ellipses) of the FS contour as expected for a quasi-1D system. However, from the above formula for the energy balance, we see that even for a moderate susceptibility it is possible to obtain a favorable energy balance if only the electron-phonon coupling is strong enough. The $(\sqrt{13} \times \sqrt{13}) - R 13.9^\circ$, reconstructed (large) unit cell is 13 times larger and contains 13 Ta and 26 sulfur atoms. Star-like arrangements develop around one central Ta atom with six nearest and six next nearest neighbors. [22] Realistic bandstructure calculations [23] including the CDW-induced star-like lattice distortion show that the single Ta *d*-band of the normal state is split. In the calculation 7 sub-bands develop, six of them full and the seventh crossing E_F . The reconstructed unit cell contains 13 inequivalent Ta atoms with a total of 13 electrons assuming the ionic picture. In order to place these electrons (two per band) 6 full bands are needed and the seventh half full, crossing E_F . Therefore we can identify two avenues for the system to gain electronic energy. First, the introduction of many small new BZ's results in the normal state FS contours to be cut into many pieces and many small gaps contribute to a lowering of electronic states. Second, the reconstruction (unit cell with 13 Ta atoms, 39 atoms in total) leads to a bandstructure where six of seven sub-bands are completely lowered below E_F , again indicative for a lower electronic energy in the CDW state. However, it is not possible to say whether these two observations represent the driving force for the CDW formation or are merely the consequence. Likewise, indications would be needed for an arbitrary system to determine whether it will or not undergo an instability and what will be the symmetry. In this context, it is interesting to note that the CDW induces a star formation (including 13 Ta atoms) with weak overlap of electronic wavefunctions between the stars possibly being responsible for the localization-induced Mott transition [30, 31]. One could think of these stars as small molecules being the consequence of a Jahn-Teller distortion at the origin of the CDW formation.

In summary, we have discussed CDW formation in 1T-TaS₂ with respect to the energy balance governing the occurrence of the CDWs. The flat parts of the elliptically shaped FS at first appear to be susceptible for nesting as for a 1D Peierls transition. A closer analysis based on the $(\sqrt{13} \times \sqrt{13}) - R 13.9^\circ$ symmetry of the CDW shows that this is not the case. Two main fingerprints pointing to a gain of electronic energy are identified, one due to many new, small BZs and one due to the creation of many sub-bands lying completely below E_F .

Skillful technical assistance was provided by E. Mooser, O. Raetz, R. Schmid, Ch. Neururer and F. Bourqui. This project has been supported by the Fonds National Suisse de la Recherche Scientifique.

4.4 Lattice-distortion enhanced electron-phonon coupling and Fermi surface nesting in 1T-TaS₂

F. Clerc,¹ C. Battaglia,¹ M. Bovet,¹ L. Despont,¹ C. Monney,¹ H. Cercellier,¹ M. G. Garnier,¹ H. Berger,² L. Forró,¹ and P. Aebi¹

¹ *Institut de Physique, Université de Neuchâtel, CH-2000 Neuchâtel, Switzerland*

² *Institut de Physique de la Matière Complexe, EPFL, CH-1015 Lausanne, Switzerland*

Submitted to Phys. Rev. B (2006)

The temperature dependence of the electronic structure of the quasi-two-dimensional material 1T-TaS₂ is revisited by considering angle-resolved photoemission spectroscopy (ARPES) and density functional theory to calculate the imaginary part of the static electronic susceptibility characterizing the nesting strength. While nesting appears to play a role in the high temperature phase, the ARPES line shapes reveal peculiar spectral properties which are not consistent with the standard two-dimensional Peierls scenario for the formation of a charge density wave. The temperature dependence of these anomalous spectral features suggests a lattice-distortion enhanced electron-phonon interaction.

4.4.1 Introduction

The interplay between lattice and electronic degrees of freedom has received renewed interest in the context of high-temperature superconductivity and colossal magneto resistance materials where electron-phonon coupling and possible polaronic effects are considered. [32,33] A significant contribution to the discussion is given by angle-resolved photoemission experiments via analysis of the spectral function. In this context it is important to examine other, more conventional materials with respect to unconventional spectral features.

1T-TaS₂ is a layered transition metal dichalcogenide (TMDC) with a quasi-two-dimensional character. Reduced dimensionality leads to peculiar electronic properties and an interesting phase diagram [13]. In particular, a charge density wave (CDW) occurs with three distinct phases as the temperature is lowered. It is incommensurate (IC phase) between 600 K and 350 K and commensurate (C phase) with a ($\sqrt{13} \times \sqrt{13}$) periodicity below 180 K, resulting in a rotation of 13.9° with respect to the underlying unreconstructed (1×1) lattice. Between 350 K and 180 K, a hexagonal array of commensurate domains with typical size of 70 Å, the so-called quasi-commensurate (QC phase) phase, is formed. The domains are separated by domain walls, or discommensurations, where the CDW changes quickly [34]. Moreover the transition to the C phase at 180 K is accompanied by a jump of the resistivity of more than one order of magnitude.

In one dimension (1D) the occurrence of a CDW is well explained by the theory of the Peierls instability [1,2] where a metal becomes unstable with respect to a spatially modulated perturbation with wave vector \mathbf{q}_{CDW} equal to two times the Fermi vector $2\mathbf{k}_{\text{F}}$. This leads to the formation of electron-hole pairs with the same wave vector and finally to the opening of a gap which provides a gain in electronic energy in order to compensate the elastic energy paid for the lattice distortion. The driving force for such an instability is given by the topology of the Fermi surface (FS) which has to present favourable nesting conditions. Namely, large portions of the FS have to be connected or nested by the vector \mathbf{q}_{CDW} . A good indicator of the quality of the nesting is the imaginary part of the static electronic susceptibility $\chi(\mathbf{q})$ which, in linear response theory, relates the response of the system to the perturbation.

The Peierls mechanism is also commonly evoked in order to explain the CDW in 1T-TaS₂ [13, 28, 35]. The topology of the FS of 1T-TaS₂ with parallel sections spanned by a vector of approximately \mathbf{q}_{CDW} has contributed to strengthen this assumption. In a recent paper [36] it was shown that in order to confirm this scenario, the knowledge of the gap-momentum dependence is of central importance. Pillo et al. [26], in their FS measurements, have observed a pseudogap over the whole FS in the C phase at a temperature below 180K as well as in the QC phase at room temperature. The removal of states at the Fermi level (E_F) is explained by a Mott localization (electron-localization of collective nature) [30, 31], which gives also rise to the strong resistivity enhancement between the QC to C phase transition. Pillo et al. interpreted the pseudogap observed at room temperature as a possible precursor effect of the Mott transition. Another explanation for the pseudogap is based on the spectral weight change induced by the new periodicity due to the CDW lattice distortion [27].

These interpretations of the pseudogap are either based on electron-electron correlations or on one-electron band theory, neglecting possible effects of strong electron-phonon interaction in this CDW material where electron phonon interaction necessarily has to play an important role. The only contribution of electron-phonon interaction considered until now is the one allowing momentum transfer between electrons and holes near E_F .

Therefore it is the aim of this paper to examine the influence of electron-phonon interaction. Indeed, as nested areas of the FS can be removed by the formation of electron hole pairs during the Peierls transition, non-nested FS may also be gapped by the influence of strong enough electron-phonon coupling [37]. Moreover, the elastic energy paid for the Peierls distortion being inversely proportional to the electron-phonon coupling parameter g , strong electron-phonon interaction can help a 2D Peierls transition. In a CDW material, the electron-lattice interaction leads to a static distortion of the whole lattice structure, but may also induce a local dynamic distortion of the lattice around the electron, forming a quasiparticle (QP) called polaron. In the case of short-range interaction it is called a small polaron, as first introduced by Holstein [38] for the study of molecular crystals. Recently, intensive numerical works have been performed on the Holstein model leading to very interesting results, notably a calculated spectral function showing a tendency towards an insulating Peierls state [37, 39, 40], depending on the electronic filling or the strength of the coupling parameter g .

After describing the experimental and computational details in the next section, we will show angle-resolved photoelectron spectroscopy (ARPES) measurements for the three phases (IC, QC, and C phase). The observed spectral changes are discussed with special attention to the influence of strong electron-phonon coupling. Low energy electron diffraction (LEED) experiments are presented to illustrate the structural changes induced by the CDW formation, and one-electron calculations based on density functional theory (DFT) are used to examine the amplitude of Fermi surface nesting. It appears that the electron-phonon coupling changes across the different CDW phases, indicating an enhancement of the coupling induced by the lattice distortion.

4.4.2 Experimental and computational details

ARPES energy distribution curves (EDC's) were acquired with a Scienta SES-200 hemispherical analyser with energy and angular resolution of $\Delta E=5$ meV and 0.25° , respectively, while the Fermi surface mapping (FSM) measurements have been collected in a modified Vacuum Generator ESCALAB Mark II spectrometer with energy and angular resolution of 50 meV and 0.5° , respectively. The sequential motorized sample rotation has been described elsewhere [15]. Monochromatized photons of energy 21.22 eV were used for all measurements reported here [14]. 1T-TaS₂ samples were prepared by vapour transport [16, 17] and cleaved *in situ* at pressures in the 10^{-11} mbar region. Surface cleanliness before and after ARPES measurements was monitored by X-ray photoelectron

spectroscopy (XPS), while we used LEED to check the sample orientation and the evolution of the CDW superstructure. The Fermi energy and instrumental energy resolution were calibrated by measuring a polycrystalline copper sample. Computation of the imaginary part of the static electronic susceptibility $\chi(\mathbf{q})$ has been done using a recent extension to Wien2k [18] based on the OPTICS package [41].

4.4.3 Results and discussion

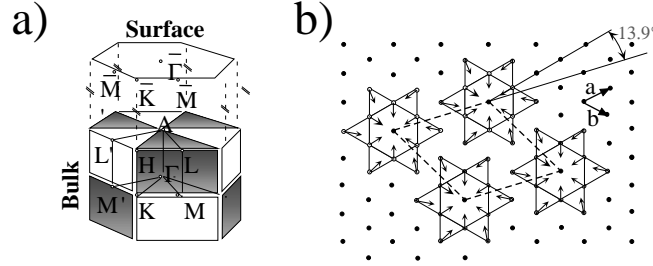


Figure 4.7: (a) Surface and bulk Brillouin zones of the 1*T* structure. (b) The (1x1) Ta plane. The arrows show the lattice distortions on the Ta sites shaping the "Stars-of-David" caused by the $(\sqrt{13} \times \sqrt{13}) - R 13.9^\circ$ -superstructure in the commensurate CDW phase.

The bulk as well as the surface Brillouin zones (BZ) are shown in Fig. 4.7(a). In Fig. 4.7(b) the Ta plane is represented with arrows indicating the CDW-induced displacements, that lead to the commensurate $(\sqrt{13} \times \sqrt{13}) - R 13.9^\circ$ superlattice observed in the C phase as well as in the domains of the QC phase. The displaced Ta atoms build the so called "Star-of-David" arrangement constituted of two outer shells of six atoms and a single atom in the centre of the star (this latter being the localization site in the model of Fazekas and Tosatti [30,31] that explains the Mott transition in this material). The CDW manifests itself also along the third dimension as shown by an x-ray diffraction study [22,23].

The LEED measurements allow to follow the evolution of the CDW as a function of temperature. In the IC phase (Fig. 4.8(a) and (b)) one can observe the high intensity spots of the (1x1) lattice, each of them being surrounded by six less intense CDW satellite spots. Only the six superspots closest to the main spot are visible due to incommensuration [42]. In accordance with previous work [43] the superspots are aligned along the $\bar{\Gamma}\bar{M}$ direction of the (1x1) structure. Note that this is 13.9° off with respect to the CDW wave vector of the C phase. By passing through the IC to QC transition the diffraction pattern (Fig. 4.8(c)) shows a drastic rotation of $\sim 11^\circ$ of the CDW satellite reflections with respect to the $\bar{\Gamma}\bar{M}$ direction. In Fig. 4.8(d) the orientation of the CDW spots is reported as function of temperature. In good agreement with previous electron diffraction [44] and STM [45] measurements, it appears that after a first step of $\sim 11^\circ$ the CDW angle is gradually increasing.

The transition from the IC phase to the QC phase has been studied theoretically on the basis of the Landau theory by McMillan [46] and more specifically for 1*T*-TaS₂ by Nakanishi and co-worker [34]. Depending on the CDW-lattice interaction they predict for the QC phase a discommensuration model consisting of domains with a commensurate structure as in the C phase separated by discommensuration regions. This model has found large support thanks to STM works [47,48] and confirmation by x-ray crystal structure refinement [22]. Therefore, the rotation of $\sim 11^\circ$ is attributed to the appearance of domains. Although inside the domains the local angle between the CDW and the lattice is 13.9°, a slightly lower angle is measured. This discrepancy is explained by Wu and al. [47], showing that the measured angle is consistent with an average

CDW vector (due to different phases of the CDW in the different commensurate domains). The evolution of this angle while lowering the temperature appears to be related to the growth of the domain sizes, the commensurate domain areas gaining weight. In our data the angle appears to go quicker to the equilibrium value than in previous experiments [44,47]. We attribute this difference to different sample quality. Indeed, a strong influence of defects on the domain sizes has been shown by Zwick [49].

An indication of the role of electronically driven instabilities as the origin of the observed CDW in the IC phase may be provided by an estimate of the imaginary part of the static electronic susceptibility $\chi(\mathbf{q})$ which is defined as $\Im\chi(\mathbf{q}) = \sum_{n',n,\mathbf{k}} \delta(\varepsilon_{n',\mathbf{k}+\mathbf{q}} - \varepsilon_{n,\mathbf{k}})$, neglecting matrix elements [50,51]. The Dirac function δ gives a contribution or not depending on whether \mathbf{q} is a nesting vector or not. Computation of $\Im\chi(\mathbf{q})$ is presented for two different q_{\perp} values on linear gray scale plots in Fig. 4.9 with white color indicating a large response of the electron system, together with $\Im\chi$ plotted along the ΓM direction. The strong intensity around $q_{\parallel} = 0$ is due to intraband contributions from a weakly dispersing band and is irrelevant for the nesting. Indeed, for $q_{\perp} = 0$ a local maximum is found around $\mathbf{q}_{\parallel} = 1/\sqrt{13} \times \mathbf{a}^*$, consistent with Myron's [52] calculations obtained for a more limited set of \mathbf{q} vectors. Out of the basal plane, one observes at $\mathbf{q}_{\perp} = 1/13 \times \mathbf{c}^*$ and $\mathbf{q}_{\parallel} = 1/\sqrt{13} \times \mathbf{a}^*$ a more pronounced local maximum confirming the out-of-plane component of the nesting vector [22,23]. Therefore, for the IC phase where the CDW is directed along ΓM and the calculated susceptibility has a distinct maximum for $\mathbf{q}_{\parallel} = 1/\sqrt{13} \times \mathbf{a}^*$, FS nesting is a plausible explanation for the onset of the CDW. Additional confidence for a standard Peierls scenario to explain the occurrence of the ICCDW comes from Fig.4.9(b) where a Fermi surface mapping (FSM) of the 1T-TaS₂ measured at room temperature is reproduced. We superimpose on this FSM the BZ corresponding to the IC superstructure. It clearly shows that some of the BZ boundaries of the IC superstructure follow the nested areas of the FS as expected in the standard Peierls scenario. Therefore, this result leads to a significant potential for electronic energy gain.

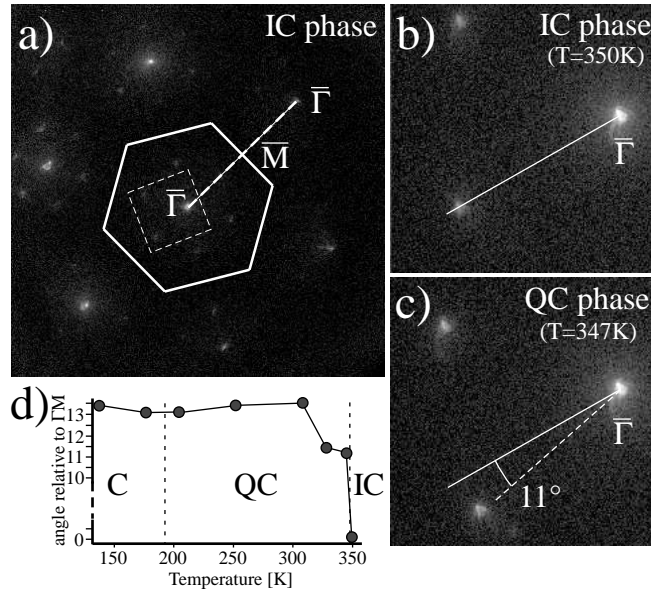


Figure 4.8: Low-energy electron diffraction patterns (electron energy 93.7 eV) for the IC phase (a) and (b) and the QC phase (c). On (a) the (1×1) hexagonal BZ is plotted and the dashed line indicates the $\bar{\Gamma}\bar{M}$ direction. (b) and (c) are zoomed pictures of the region delimited by the dashed square of (a). The lines are guide to the eye and refer to the $\bar{\Gamma}\bar{M}$ direction. (d) Temperature dependence of the angle between $\bar{\Gamma}\bar{M}$ direction and $\bar{\Gamma}$ -superspot position.

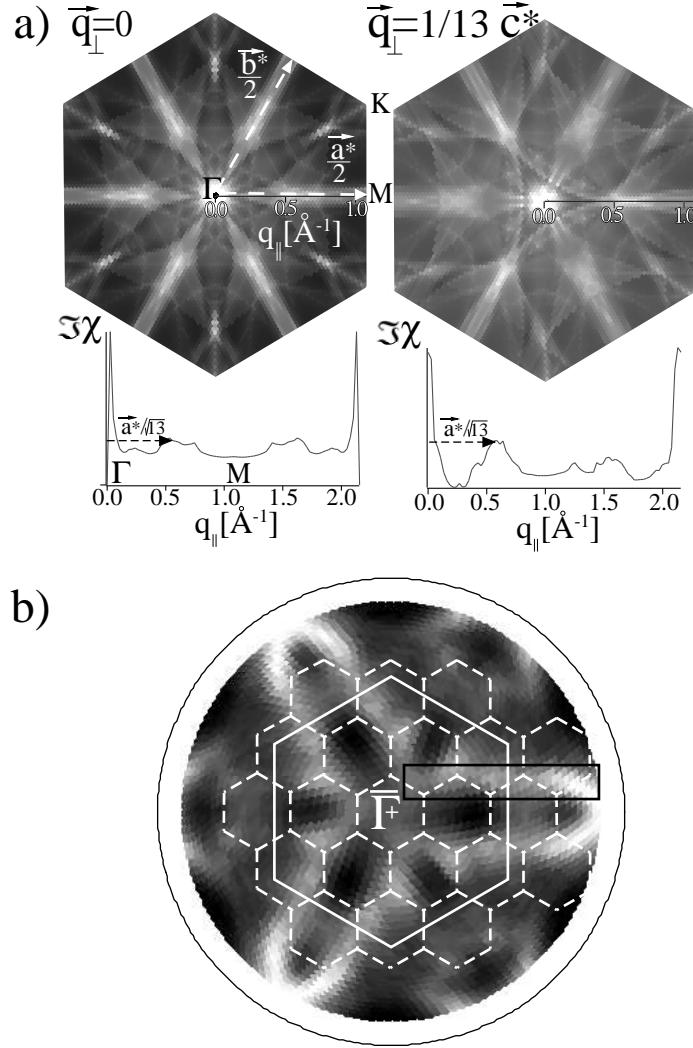


Figure 4.9: (a) Top, imaginary part of the static electronic susceptibility in the first Brillouin zone at $q_\perp=0$ (Γ MK plane) and $\frac{1}{13}c^*$. Bottom, imaginary part of the static electronic susceptibility vs momentum vector along Γ M direction. The dashed arrows correspond to the CDW vector of the IC phase extracted from diffraction measurements. (b) Fermi surface mapping measured at room temperature with the unreconstructed hexagonal BZ (white plain line) and the hexagonal BZ of the IC superstructure (white dashed line). The black rectangle is used to highlight the superposition of the nested FS areas with the BZ boundaries of the IC phase.

But, as pointed out by Johannes et al. [53], the definitive evidence of the nesting contribution to the CDW formation needs confirmation by calculation of the real part of the static electronic susceptibility. Presently this calculation is beyond our capabilities. Nevertheless, we can expect a local maximum in the real part. In fact, given the geometry of the FS of 1T-TaS₂, the maximum in the imaginary part of the susceptibility at the correct \mathbf{q}_{ICDW} vector can be attributed to the presence of flat areas on the FS, and, numerical simulation (not using DFT) for a 2D toy model (not shown), i.e. closed FS with flat areas, leads to a local maximum not only in the imaginary part of the susceptibility but also in the real part of the susceptibility.

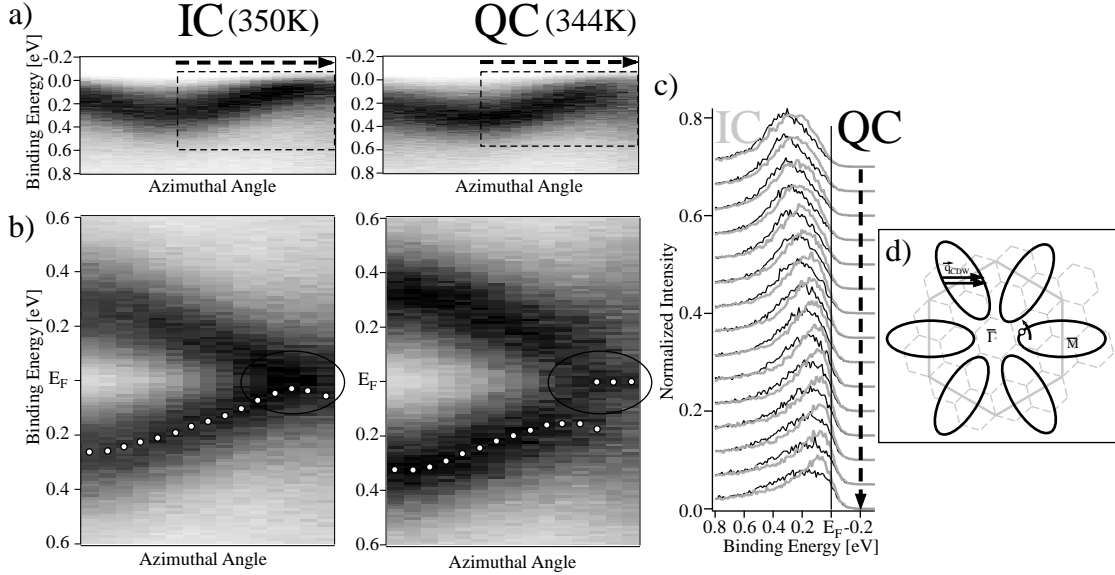


Figure 4.10: (a) ARPES intensity maps measured along the azimuthal angle at a polar angle of 14° , for the IC and QC phases. (b) Symmetrized plots of the zone delimited by the dashed rectangle on the maps on top. The corresponding location in the surface reciprocal space is shown by the curved arrow on the FS sketch in (d). (c) EDCs extracted from the maps plotted in (a), in black for the QC phase and gray for the IC phase. The dashed arrow is located at the same position as the dashed arrows of (a). (d) The black ellipses represent a sketch of the FS where are also superimposed the (1×1) BZ and the $(\sqrt{13} \times \sqrt{13}) - R 13.9^\circ$ BZ boundaries in continuous gray lines and dashed gray lines, respectively. The small white circle indicates the location where the EDCs of Fig.4.11 are measured

Fig. 4.10 presents ARPES measurements in the IC and QC phases, taken at 350 K and 344 K, respectively. The intensity plots (high intensity in black) on Fig. 4.10(a) are azimuthal cuts taken at a polar angle of 14° with respect to $\bar{\Gamma}$. The only visible band, near E_F , originates from Ta 5d electrons. In Fig. 4.10(b) these intensity plots are symmetrized with respect to the Fermi level and summed, in order [54, 55] to remove the perturbative effect of the Fermi-Dirac distribution cutoff and to infer whether the spectral function peak crosses the chemical potential or not. Fig. 4.10(c) shows the energy distribution curves (EDCs) corresponding to the intensity plots shown in Fig. 4.10(a). In Fig. 4.10(d) a sketch of the FS contours is drawn, together with a superposition of the normal- and commensurate-state BZs. The curved arrow indicates the location of the intensity plots of Fig. 4.10(a). The presumed nesting vector \mathbf{q}_{CDW} is also drawn according to the calculation of $\Im\chi(\mathbf{q})$, connecting flat parts of the elliptically shaped FS with large, possibly nested (parallel) portions which have strongly turned the discussion of the origin of the CDW towards the nesting scenario.

As mentioned in the introduction a clear picture of the gap momentum dependence is crucial for the interpretation of the origin of the CDW. Pillo et al. [26] first, and Bovet et al. [27] later, have both observed an entirely pseudogapped FS at room temperature (QC phase) without any differentiation between presumed nested areas, new BZ boundaries and other FS parts. The pseudogap was either interpreted as a precursor effect of the Mott transition in the commensurate domains due to the already formed "Stars-of-David" superstructure with electron localization sites at the centre [26] or as a band structure effect due to the new symmetry induced by the lattice deformation [27]. Here we want to introduce a new possible explanation based on the detailed spectral features of Fig. 4.10. However, one has to be aware that the new interpretation does not contradict the previous ones, but gives a new point of view. As long as quantitative modeling of ARPES for realistic microscopic models is not available it is not clear to what degree a given interpretation is unique.

Consistently with the two previous authors we have performed the same measurements on large parts of the FS (not shown) and we do not observe a different behaviour than that shown in Fig. 4.10 and described in the following.

In the IC phase (Fig. 4.10(a) and (b), left) a broad Ta 5d band flattens and narrows slightly when approaching E_F , giving rise to a small maximum centred at E_F in the symmetrized plot. In a standard interpretation of the symmetrization procedure this would be attributed to a Fermi level crossing of the quasiparticle peak (QP). However, band calculations predict a linear slope through E_F and no flattening as observed. Moreover within the Fermi-liquid picture ARPES peaks are attributed to QP excitations whose lifetime increases when approaching E_F . However, in our case the Ta 5d peak remains anomalously broad near E_F . Thus we are clearly in presence of a renormalized band which touches E_F without clearly crossing it. Also, a renormalization of the entire FS, as observed, is not consistent with an explanation based solely on a 2D Peierls scenario. Since the interaction of electrons with the lattice is a key aspect of the CDW instability, a natural candidate to explain these anomalous spectral properties is electron-phonon coupling which can induce polaronic effects [32, 56, 57]. A polaron is the fermionic QP made of an electron surrounded by a local lattice distortion which enhances its mass. Depending on the strength and the character of the interaction, the spectral changes induced by the electron-phonon coupling can be more or less dramatic. But, in any case, they are reflected by a band flattening and a partial or complete transfer of the spectral weight from the coherent QP to a broad incoherent part on the high binding energy side (for a detailed view of changes induced in the spectral function see references [7, 32, 37, 56, 57]). A polaronic scenario could thus explain the apparent absence of QP crossing as well as the broad line shape and the isotropically pseudogapped experimental FS.

An enhancement of the previous anomalies can be observed upon cooling down to the QC phase (Fig. 4.10(c)). The line shape gets abruptly broader (when lowering T by only 6 K), the centre of mass of the Ta 5d band shifts towards higher binding energy when approaching the Fermi vector and becomes clearly separated from a small maximum visible in the symmetrized plot (Fig. 4.10(b), right). This symmetrization peak originates from a finite spectral weight near E_F . Bovet et al. [27] attributed this to a reconstructed band coming from above and merely straddling E_F . In the polaronic picture proposed here, this finite intensity near E_F is also compatible with a remnant weight of the coherent QP [37].

The changes between the photoemission spectra of the IC and QC phases are abrupt and are interpreted as a change of the electron-phonon interaction character. Indeed, in 2D or 3D systems there is a qualitative dependence of the polaron type (large or small) on the range of the electron-lattice interaction [58]. While large polarons are formed if the electron-lattice interaction due to the long range Coulombic interaction between electronic carriers and lattice ions is of predominant importance, small polarons form if the short range electron-lattice interaction such as the deformation potential interaction dominates. The formation of the commensurate domains in

the QC phase introduces, as shown above, the "Stars-of-David" which can be identified with small molecules acting as potential wells and hence favouring the short range interaction. Moreover, it has been noted [58] that the presence of long-range interaction eases the requirements for forming small polarons. Therefore, the CDW in the IC phase leads to a static deformation of the whole lattice structure which, in turn, leads to a more local character of the electron-lattice interaction and an enhancement of the electron-phonon coupling strength, i.e, to a lattice distortion enhanced electron-phonon coupling.

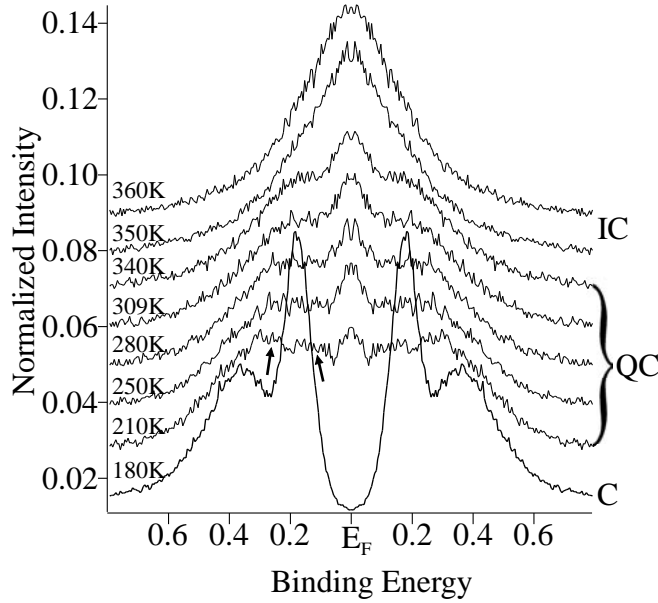


Figure 4.11: Temperature dependence of symmetrized ARPES spectra. All the spectra are taken at the position indicated by the white circle on the FS sketch of Fig.4.10(d). The arrows point to the two separated structures discussed in the text.

A complete evolution of the symmetrized EDCs as a function of temperature is represented in Fig. 4.11. These EDCs are all measured at the position indicated by the white circle on the FS sketch of Fig. 4.10(d). The abrupt changes when going from the IC to the QC phase are obvious: the broad feature centred at E_F in the IC phase is split into a small maximum and a broad hump on the higher binding energy side in the QC phase. Inside the QC phase, a smooth variation, reflected by a slightly decreasing intensity at E_F and a spreading of the hump towards higher binding energy is observed when lowering the temperature. The hump structure even splits up into two structures at binding energies of 0.125 eV and 0.270 eV, as indicated by the two arrows. This is in agreement with the domain size growth observed by STM [47, 48], with a continuous shrinkage of the discommensurate region which hence has less weight in the ARPES intensity and thus allows the appearance of the commensurate electronic structure which is split into sub-bands [59]. Moreover, as was mentioned by Zwick and al. [49], the number of free carriers able to screen electron-electron as well as electron-phonon interaction steadily decreases along with the domain growth. Therefore, the evolution of the spectral line shape in the QC phase is also influenced by a variation of the electron-lattice coupling.

The transition into the C phase (Mott transition [30, 31]) introduces more drastic modifications in the symmetrised curves, with the disappearance of the small maximum at E_F and the strong intensity enhancement of the peak closest to the Fermi level accompanied by a shift of ≈ 60 meV towards higher binding energy. Moreover, the splitting of the Ta5d band into sub-bands, as predicted by the Tosatti and Fazekas model, appears very clearly. All these spectral changes

were previously attributed to a change of regime, with the electron-electron correlation strongly dominating the physics of the C phase, leading to a Mott transition. It is interesting to note that the splitting of the Ta 5d band takes place above the occurrence of the Mott transition. This splitting has the effect of strongly reducing the electronic bandwidth and, in parallel, contributing to increase the relative weight of the Hubbard repulsion term, confirming that favourable conditions for the Mott insulator transition are induced by the CDW reconstruction.

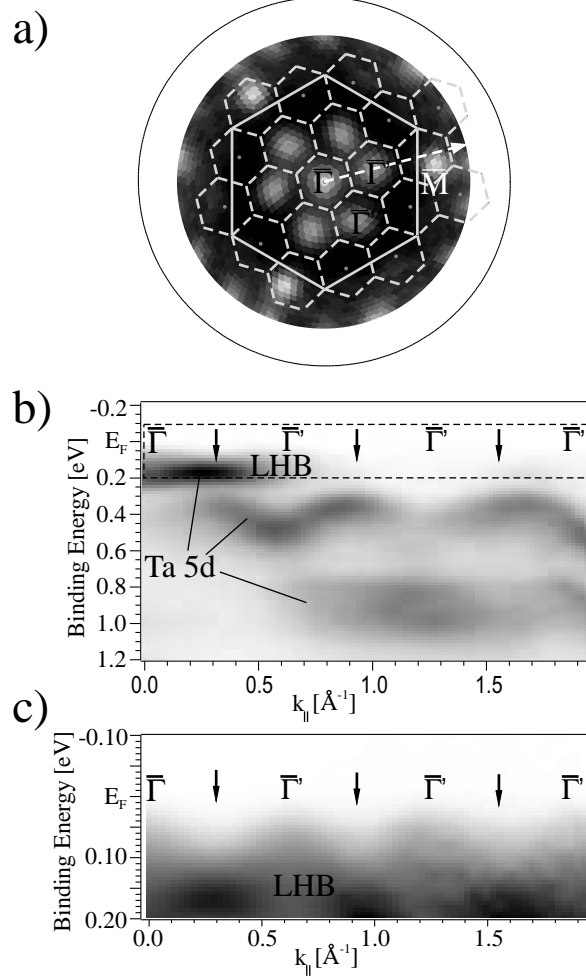


Figure 4.12: (a) Fermi-surface map measured in the C phase. Superposed on it are the (1x1) BZ boundaries as well as the BZ boundaries of the commensurate superstructure in thin dashed lines. (b) ARPES intensity map measured in the direction of the new $\bar{\Gamma}$ points of the $(\sqrt{13} \times \sqrt{13}) - R 13.9^\circ$ -superstructure. The corresponding direction in surface reciprocal space is given by the dashed white arrow on the FSM. (c) Zoom and renormalization of the region delimited by the dashed rectangle in (b). The small arrows in (b) and (c) point to the location of the new BZ boundaries.

In Fig. 4.12(a) a FSM measured at 20 K is plotted with respect to the wave vector component parallel to the surface. The (1x1) BZ is superimposed as well as the new BZ due to the commensurate CDW, illustrated by the small hexagons. What is reported is the photoelectron intensities (grayscale, with high intensity in white) measured in a narrow energy window around E_F , as a function of emission angle. The outer circle corresponds to grazing emission. Having identified no clear QP crossing of E_F in the previously discussed data we note that the experimental FSM is a pattern reflecting the anisotropic distribution of the remaining spectral weight of the electrons

at E_F . The obtained pattern with high intensity features centred in the small hexagons is fully consistent with the $(\sqrt{13} \times \sqrt{13}) - R 13.9^\circ$ symmetry of the commensurate superstructure. For larger polar angles the correspondence is less perfect, and the absence of intensity at the centre of some hexagons may be explained by matrix element arguments used to explain the absence of branches of the elliptically shaped normal state FS [25]. In Fig. 4.12(b) EDCs measured along the new $\bar{\Gamma}$ points (indicated by the white dashed arrow in Fig. 4.12(a)) are shown in grayscale with high intensity in black. According to the "Stars-of-David" picture and its inequivalent Ta atoms, one can distinguish three smoothly dispersing Ta 5d sub-bands, two completely filled at binding energies of 0.43 eV and 0.9 eV and the lower Hubbard band (LHB) closer to E_F . By zooming into the dispersion of the LHB (see Fig. 4.12(c)), after adjusting the gray scale, one can observe decreased spectral weights at the new BZ boundary positions (indicated by arrows) and increased spectral weights at the new $\bar{\Gamma}$ points. We therefore conclude that the intensity peaks in the FSM result from the dispersion of the LHB. In a recent article [60] the authors identify a splitting of the LHB, presumably induced by magnetic ordering with a new periodicity. However, in view of the perfect correspondence of the LHB dispersion with the CDW induced BZs, we preferably attribute these structures to the commensurate superstructure and note that the periodic depletion of spectral weight (arrows in Fig. 4.12(c)) is attributed to the CDW gap which follows the new BZ boundaries. Indeed, if we base on the results of Sangiovanni and al. [61] who observed that in a strongly correlated regime where the Hubbard repulsion is the dominant scale, the electron-phonon coupling has basically no effect on the QP spectral shape anymore, we can expect that these modulations in the LHB were hidden in the QC phase by the influence of electron-phonon interaction, and reappear in the C phase when going to the strong electron-electron correlation regime.

4.4.4 Summary and conclusion

We have investigated the temperature dependence of the electronic structure of 1T-TaS₂. The computation of the imaginary part of the static susceptibility reveals a small and broad local maximum at a q value in good agreement with the expected nesting vector for the IC phase. Additionally the superposition on the FSM of the BZ corresponding to the IC superstructure show the possibility of a significant potential of electronic energy gain. These two observations point strongly towards the Peierls mechanism to explain the ICCDW phase occurrence. We exploited ARPES to study the band structure in the three phases (IC-QC-C). In contradiction with a pure 2D Peierls scenario, we did not find any clear QP crossing in the QC phase as well as in the IC phase but instead, we observed a broad dispersing feature with renormalized dispersion while approaching the Fermi level. Based on polaronic considerations, we can understand these anomalous spectral properties. However, the presence of polarons has to be confirmed by other methods. Available optical measurements do not allow to accept or reject this point of view [62]. More precise data in the midinfrared region as a function of temperature are needed. By interpreting the "star-of David" cluster as a small molecule we invoke a possible interplay between long range and short range electron-lattice interaction which may well enhance the strength of the coupling and hence give even more support to the polaronic point of view. By lowering the temperature through the Mott transition, the physics changes to a strongly correlated electron-electron interaction regime. The C phase data is in perfect agreement with the symmetry of the commensurate superstructure and even reveals a dispersive modulation of the LHB which allows to locate the CDW gap at the position of the new BZ boundaries. To conclude, it turns out that although 1T-TaS₂ has been studied since decades, its complex phase diagram and the mechanism behind the CDW formation are still subject of debate. As long as quantitative simulations of ARPES data with realistic microscopic models are still missing, it is not clear to what point a

4.4. Lattice-distortion enhanced electron-phonon coupling and Fermi surface nesting in 1T-TaS₂

given interpretation is unique. Nevertheless, the qualitative agreement of the behaviour of our measured line shapes with a scenario based on the presence of polarons presents a new point of view to explain instabilities in 1T-TaS₂.

Acknowledgements

We are grateful to Claudia Ambrosch-Draxl for extending the optic package of Wien2k to the computation of susceptibility. Skillful technical assistance was provided by our workshop and electric engineering team. This project has been supported by the Fonds National Suisse pour la Recherche Scientifique.

4.5 Complement

4.5.1 Coexisting periodicities in 1T-TaS₂

In ordinary periodic crystals, the energy levels are organized in bands reflecting the translational symmetry. This band structure differs from the free electron dispersion essentially by the opening of gaps at the BZ boundaries and by the folding back of dispersion branches into the first BZ [6]. Thanks to the periodicity, all electronic states can be described using wavevectors in the first BZ only. In CDW systems a more complex situation arises, due to the presence of two different periodic potentials in the solid at the same time. The questions are how is the band structure influenced by the CDW potential and what do we measure with ARPES?

Fig. 4.13 shows an ARPES measurements taken at room temperature (QCCDW state) of 1T-TaS₂ along the $\bar{\Gamma}\bar{M}$ direction. As already observed in section 4.3, despite the presence of the CDW potential V_{CDW} , the experiment exhibits the symmetry of the normal state BZ. Thus, although the electron wavefunctions must conform to the resulting overall periodicity, the ARPES seems to be insensitive to the periodicity of V_{CDW} . To investigate the effects of competing periodic potentials on the band structure and ARPES intensity, we consider the simple 1D model used by Voit et al. [24,63] and we evaluate the spectral function by exploiting Green's function method.

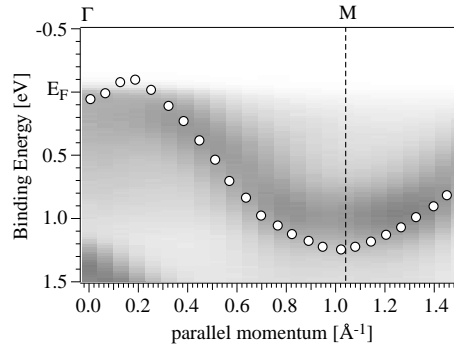


Figure 4.13: Band dispersion along the $\bar{\Gamma}\bar{M}$ direction of the Ta 5d-derived band of the 1T-TaS₂ in QCCDW state.

First, we consider the simple case of a 1D tight binding electron system with a lattice constant a (periodicity in reciprocal space $Q_1 = \frac{2\pi}{a}$). The resulting dispersion $\epsilon(k) = -2t\cos(ka)$ is plotted in red in Fig. 4.14 (a). A second periodic potential $V(x) = V\cos(ka_1)$, commensurate with the first one for reasons of simplicity, is introduced. We choose $a_1 = 2a$ (periodicity in reciprocal space $Q_2 = \frac{\pi}{a}$). This situation corresponds exactly to what is encountered in a 1D electron system with a half-filled conduction band undergoing a Peierls transition. The corresponding Hamiltonian is expressed in second quantification as:

$$H = \sum_k \{ \epsilon(k) c_k^+ c_k + \sum_q [V(q) c_{k+q}^+ c_k + H.c.] \} \quad (4.33)$$

where the potential is $V(q) = V\delta_{qQ_2}$, c_k (c_k^+) is the destructor (creator) of an electron with momentum k , and the spin is neglected. Because $2Q_2$ is a reciprocal lattice vector, the Hamiltonian is the 2×2 following matrix:

$$\hat{M} = \begin{pmatrix} \epsilon(k) & 2V \\ 2V & \epsilon(k + Q_2) \end{pmatrix}$$

Its diagonalization leads to the following eigenvalues $\lambda_k^\pm = \pm \sqrt{4t^2 \cos^2(k) + 4V^2}$, and therefore to the new dispersion drawn in blue in Fig. 4.14 (a). As expected a gap opens at the new zone boundaries $\pm \frac{\pi}{a_1}$ and the band folds back into the new BZ. These results seem to be in conflict

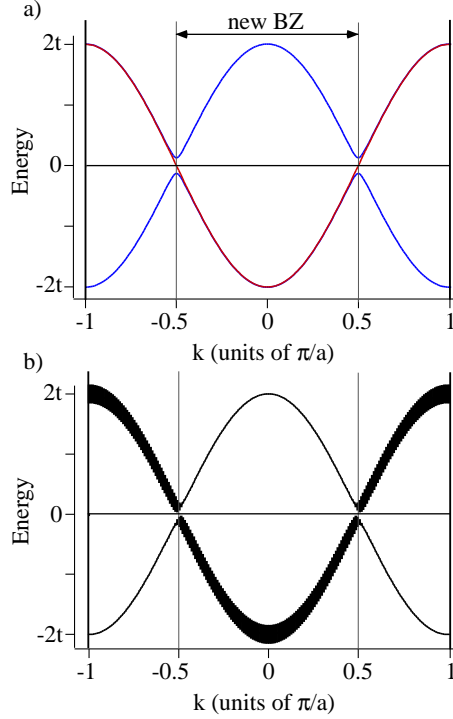


Figure 4.14: (a) Tight binding bands for a 1D potential with periodicity a (red line) and for a system with a second perturbative potential with periodicity $a_1 = 2a$. (b) Spectral weight distribution for a system with competing commensurate periodicities (see text).

with what is observed in Fig. 4.13 for the $1T$ -TaS₂ where the new periodicity of $\sqrt{13}$ is not reflected. However we ought to keep in mind that the ARPES intensity is proportional to the spectral function weighted by matrix elements.

In the aim to determine the spectral function, one starts by defining the Green's function matrix as

$$\hat{G}(k, t) = \begin{pmatrix} \ll c_k(t); c_k^+(0) \gg & \ll c_k(t); c_{k+Q_2}^+(0) \gg \\ \ll c_{k+Q_2}(t); c_k^+(0) \gg & \ll c_{k+Q_2}(t); c_{k+Q_2}^+(0) \gg \end{pmatrix}$$

The equations of motion can be formulated for each component of $\hat{G}(k, t)$. For the first element $\ll c_k(t); c_k^+(0) \gg$, the equation of motion is

$$\begin{aligned} i \frac{\delta}{\delta t} \ll c_k(t); c_k^+(0) \gg &= \frac{\delta}{\delta t} \{ \langle c_k(t) c_k^+(0) \rangle \Theta(t) - \langle c_k^+(0) c_k(t) \rangle \Theta(-t) \} \\ &= \delta(t) \langle c_k(t) c_k^+(0) \rangle + \Theta(t) \langle \frac{\delta}{\delta t} c_k(t) c_k^+(0) \rangle \\ &\quad + \delta(t) \langle c_k^+(0) c_k(t) \rangle - \Theta(-t) \langle c_k^+(0) \frac{\delta}{\delta t} c_k(t) \rangle \\ &= \delta(t) \langle \{ c_k(t), c_k^+(0) \} \rangle + \langle T \{ \frac{\delta}{\delta t} c_k(t) c_k^+(0) \} \rangle \\ &= \delta(t) + \ll [c_k(t), H]; c_k^+(0) \gg \end{aligned} \quad (4.34)$$

where in the last step we apply the anticommutation property of fermions operators and the time evolution of a Heisenberg operator ($i \frac{\delta}{\delta t} A(t) = [A(t), H]$). By introducing the Hamiltonian

expression 4.33 we can evaluate the commutator

$$[c_k(t), H] = \sum_{k'} \{ \epsilon(k') c_{k'}(t) \delta_{kk'} + V c_{k'}(t) (\delta_{kk'+Q_2} + \delta_{kk'}) \}$$

and introduce the result in (4.34). Therefore the equation of motion for $\ll c_k(t); c_k^+(0) \gg$ leads finally to the following expression

$$\begin{aligned} i \frac{\delta}{\delta t} \ll c_k(t); c_k^+(0) \gg &= \\ \delta(t) + \epsilon(k) \ll c_k(t); c_k^+(0) \gg & \\ + 2V \ll c_{k+Q_2}(t); c_k^+(0) \gg & \end{aligned} \quad (4.35)$$

By proceeding in the same manner for all the elements of \hat{G} , we obtain the equation of motion of the matrix \hat{G}

$$i \frac{\delta \hat{G}}{\delta t} = \hat{M} \hat{G} + \mathcal{I} \delta(t) \quad (4.36)$$

By analogy with a one dimensional calculation, the equation (4.36) can be solved by a Fourier transform:

$$\hat{G}(k, \omega)^{-1} = i\mathcal{I}\omega - \hat{M} = \begin{pmatrix} i\omega - \epsilon(k) & 2V \\ 2V & i\omega - \epsilon(k + Q_2) \end{pmatrix} \quad (4.37)$$

At this point we artificially consider that the spectral function is derived only from the first component of $\hat{G}(k, \omega)$:

$$\begin{aligned} G_{11}(k, \omega) & \\ &= \frac{i\omega - \epsilon(k + Q_2)}{(i\omega - \epsilon(k))(i\omega - \epsilon(k + Q_2)) - 4V^2} \\ &= \frac{i\omega - \epsilon(k + Q_2)}{(i\omega - \lambda_k^+)(i\omega - \lambda_k^-)} \\ &= \frac{u^2}{i\omega - \lambda_k^+} + \frac{v^2}{i\omega - \lambda_k^-} \end{aligned} \quad (4.38)$$

where $u^2 = \frac{\lambda_k^+ - \epsilon(k + Q_2)}{\lambda_k^+ - \lambda_k^-}$ and $v^2 = \frac{\lambda_k^- - \epsilon(k + Q_2)}{\lambda_k^- - \lambda_k^+}$. Finally the spectral function is

$$A(k, \omega) = \frac{1}{\pi} | \text{Im} G_{11}(k, \omega) | = u^2 \delta(\lambda_k^+) + v^2 \delta(\lambda_k^-). \quad (4.39)$$

This spectral function is drawn in Fig. 4.14 (b) where we observe that while the dispersion of the eigenvalues follows the repeated zone scheme, the spectral weight keeps peaked on the extended zone scheme dispersion and thus follows the unperturbed periodicity, in agreement with our ARPES measurements. The only visible effects of the second potential are the gaps which appear at the new zone boundaries. Their presence depends on the weight transfer to the backfolded band, which is a function of the strength of the perturbative potential.

Thus consistency with ARPES data is found by only considering the first component of $\hat{G}(k, \omega)$ during the evaluation of the spectral function. An identical calculation starting with the last component of $\hat{G}(k, \omega)$, namely $G_{22}(k, \omega)$, will give a similar result but with the negative spectral weight as the previous one. Therefore, we conclude that the effect of matrix elements for systems with competing periodicities is similar to a projection on the unperturbed dispersion (in our case the red one of Fig. 4.14 (a)).

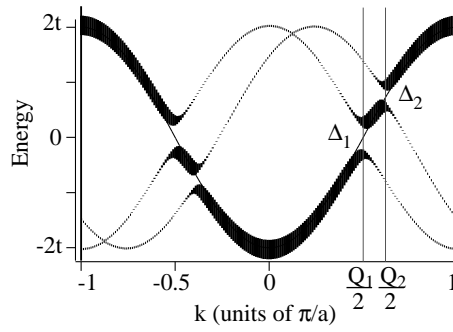


Figure 4.15: Spectral weight distribution found for a system with competing incommensurate periodicities.

We can now consider the more general case of two incommensurate potentials Q_1 and Q_2 . In these conditions the potential in 4.33 becomes $V(\mathbf{q})=V_1\delta_{\mathbf{q},Q_1} + V_2\delta_{\mathbf{q},Q_2}$ and the matrix representing H is now infinite. We can find approximate solutions by truncating this matrix and repeating the calculation done for the commensurate case. The spectral function found for a truncation of H by a 3×3 matrix is drawn on Fig. 4.15. Again the spectral intensity is concentrated on the extended zone scheme dispersion. Gaps open at $\frac{Q_1}{2}$ and $\frac{Q_2}{2}$ and new weak bands are generated. These ones cannot be described in a repeating zone picture contrary to the commensurate case. The number of shadow bands and gaps increases with the size of the truncated Hamiltonian matrix and the gap sizes become exponentially small. Thus with larger matrices the eigenvalues tend to form a non dispersive scheme but by the localization of the spectral weight on eigenvalues following the extended zone scheme, we find again a dispersion representative of the unperturbed structure.

So despite the destruction of translational invariance and the absence of periodicity, ARPES intensity of such a system with incommensurate competing potentials displays dispersion. Our measurements of the $1T$ -TaS₂ in the incommensurate CDW state (Fig. 4.10) confirm these assumptions. Such behavior has also been observed in quasi-crystalline systems [64].

4.5.2 Polaron

To understand the ARPES line shape it is crucial to establish the existence of gaps, pseudogaps or dispersion anomalies in samples. As discussed in chapter two where we have introduced many body aspects, the spectral function can exhibit complex structures composed of a main peak, the so-called quasiparticle peak, and of an incoherent background. This interpretation of ARPES data has allowed identification of many famous features such as the Fermi liquid behaviour of some metallic systems [65], the superconducting gap [66–68], the kink of the dispersion curves of cuprates [33] or spectral signs of electron-phonon coupling on metallic surfaces [69–71]. However during this last decade several works have revealed failures of this conventional framework assuming that the main peak of the ARPES spectra represents a quasiparticle pole. Indeed some materials such as certain manganites with colossal magnetic resistance [72, 73], certain cuprates in underdoped regime [74, 75] or quasi-one dimensional conductors exhibiting CDW [76, 77] expose pseudogapped broad ARPES line shapes with missing quasiparticle peak. Independently of the studied material the authors of these works explain these anomalous spectral features in terms of strong coupling with collective excitations. While the nature of these collective modes in cuprates is still debated [78], strong electron-phonon coupling is generally put forward to explain the unusual spectra of manganites and quasi-one dimensional CDW compounds. We also consider this mechanism to explain the complete removal of the Fermi surface of the $1T$ -TaS₂ in the QCCDW state (section 4.4). Thus we propose here to detail the behaviour of ARPES line shapes under (strong) electron-phonon coupling conditions.

As first approach we choose to study the exactly solvable model of the coupling of a single

electron to a bath of independant phonons of energy ω_0 [7]. We will see that the broad line shape as well as the vanishingly quasiparticle spectral weight come naturally from the calculated spectral function of this model. Moreover as nicely showed by Dessau et al. [72] an unusual dispersion behaviour can be extrapolated from this independent boson model. The Hamiltonian representative of this model may be written as:

$$H = c^\dagger c [\epsilon_c + \sum_{\mathbf{q}} M_{\mathbf{q}} (a_{\mathbf{q}} + a_{\mathbf{q}}^\dagger)] + \sum_{\mathbf{q}} \omega_{\mathbf{q}} a_{\mathbf{q}}^\dagger a_{\mathbf{q}}. \quad (4.40)$$

and after canonical transformation it becomes:

$$H = c^\dagger c (\epsilon_c - \Delta) + \omega_0 \sum_{\mathbf{q}} a_{\mathbf{q}}^\dagger a_{\mathbf{q}}. \quad (4.41)$$

It describes a fixed particle of bare energy ϵ_c interacting with a set of Einstein phonons of energy ω_0 . Due to the coupling the ground state energy is shifted by an amount $\Delta = g\omega_0 = \sum \frac{M_{\mathbf{q}}^2}{\omega_0}$ where $M_{\mathbf{q}}$ is the ion mass and g the coupling constant describing the coupling strength. We note that the interaction between the fixed electron and the set of independent bosons occurs only when the state is occupied, namely when $c^\dagger c = 1$.

The spectral function may be determined by standard calculation of the Green's function and is for zero temperature:

$$A(\omega) = 2\pi e^{-g} \sum_{l=0}^{\infty} \frac{g^l}{l!} \delta(\omega - \epsilon_c + \Delta - \omega_0 l) \quad (4.42)$$

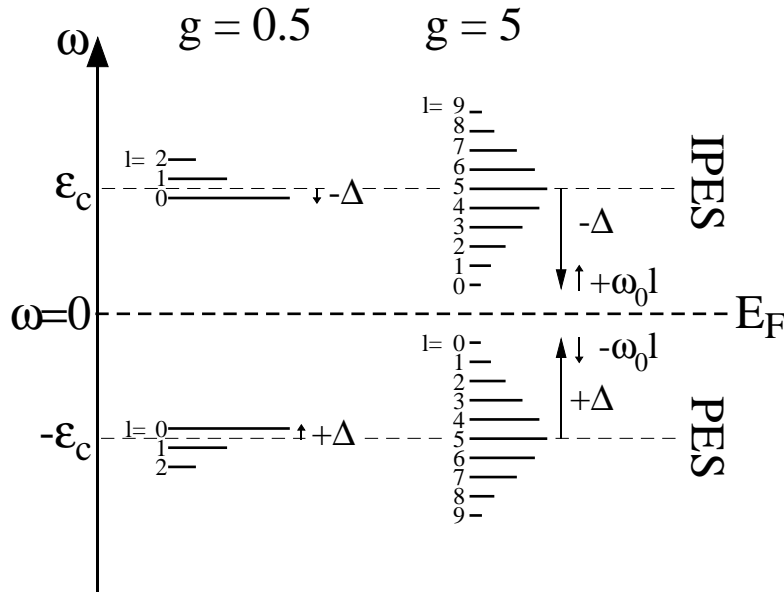


Figure 4.16: Schematic IPES ($\omega > 0$) and PES ($\omega < 0$) spectral functions of a single fixed electron coupled to a bath of phonons of frequency ω_0 for weak ($g=0.5$) and strong ($g=5$) coupling. For both regimes the spectrum consists of a multi-peaks structure and the quasiparticle ground state is shifted from the free electron energy ϵ_c by Δ , more significant for strong coupling case. For $g=0.5$ the quasiparticle ($l=0$) contains most of the spectral weight while for the larger g the spectral weight is transferred to the satellites ($l > 0$) with maximum of intensity located on the centroide of the spectrum.

This function is drawn in Fig. 4.16 for the weak and the strong coupling cases. In Fig. 4.16 we separate also the IPES region ($\omega > 0$) from the PES region ($\omega < 0$). The spectral function is an envelope of many individual peaks spaced ω_0 apart. The peak closest to the Fermi level is the

quasiparticle peak or zero-phonon peak, shifted by Δ from the non-interacting energy position ϵ_c . The following peaks are satellites. They indicate that the single electron is not an eigenstate of the Hamiltonian (4.40), and that therefore the particle has a finite probability of occupying other states carrying l phonons with them. From the PES point of view it means that a removal of an electron from the system occurs with a probability of shaking off a certain number of bosons. This picture gives rise to a similar photoemission spectrum that for the molecule H_2 , and is thus mentioned as due to Franck Condon broadening. From Fig. 4.16 we observe obvious differences between the two coupling regimes. For the weak coupling case most of the spectral weight is concentrated on the quasiparticle peak which is still located near the bare energy ϵ_c . For strong coupling the shape is broader, with the quasiparticle far away from ϵ_c and having very small spectral weight. The maximum of intensity is still located near ϵ_c but in the region of the satellites. This strong coupling line shape describes very well the spectra observed in works cited above and thus gives confidence on the role of electron-boson coupling in these systems.

For a non-zero temperature the spectral function becomes:

$$A(\omega) \sim 2\pi e^{-g} \sum_{l=-\infty}^{+\infty} e^{l \frac{\omega_0}{2k_B T}} \delta(\omega - \epsilon_c + \Delta - \omega_0 l) \quad (4.43)$$

This is similar to the case for $T=0$ K apart from the summation that contains here negative l values, due to the absorption by the particle of thermally activated phonons. However the shape remains similar to the one of fig. 4.16 because the factor $e^{l \frac{\omega_0}{2k_B T}}$ skews the envelope of intensities to the positive side, $l > 0$.

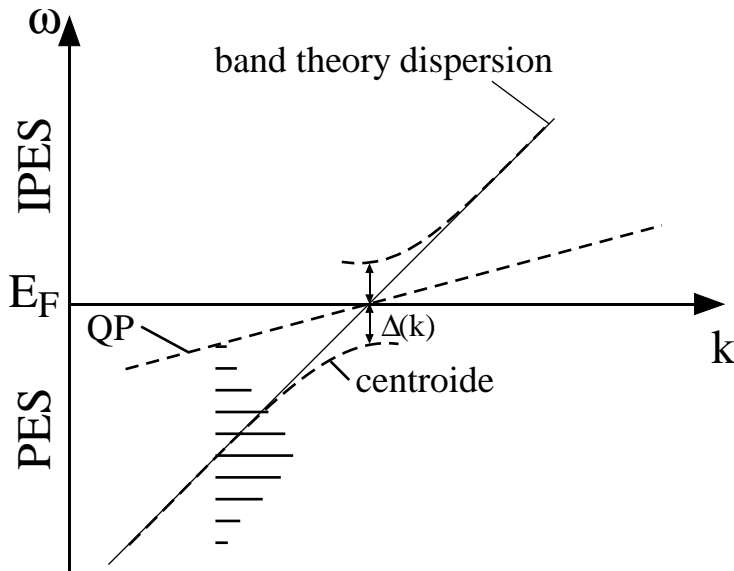


Figure 4.17: Extrapolated dispersion behaviour from the independent bosons model in strong coupling regime. The quasiparticle is expected to disperse less than what the band theory predicts but crosses the Fermi level at the band theory Fermi momentum. The centroid of the ARPES spectrum follows the free electron dispersion until it approaches the Fermi level where the band flattens leading to the opening of a pseudogap. From ref. [72]

To compare further this model for strong coupling with ARPES data, it is interesting to extrapolate it to a many particle system including band dispersion in the same manner as done by Dessau et al. [72]. The expected behaviour is exposed in Fig. 4.17 In analogy with the single electron model above, the centroid of the ARPES spectrum (maximum of intensity) follows the band theory dispersion through most of the k -space. The quasiparticle peak with almost no intensity is separated by Δ from the centroid. According to the Luttinger theorem, the

quasiparticle crosses the Fermi level at the same momentum than what the band theory predicts. We note by reference to our introduction of many body effects in chapter 2.3 that Δ corresponds to the self-energy. Δ being non-zero even at k_F , the centroid dispersion separates from the one of band theory and stays always well below the Fermi level. This flattening of the centroid dispersion leads to a pseudogap in the spectral function. We suggest that this pseudogap is responsible for the removal of the whole Fermi surface in case of isotropic coupling collective mode. Finally as said above the interaction between the particle and the collective modes occurs only when the states are occupied, therefore as soon as the quasiparticle peak crosses the Fermi level the entire photoemission spectrum rapidly loses intensity. However a remnant weight stays above k_F due to particle-hole mixing.

A step further than this extrapolation of the model of independent bosons is the study of the general Hamiltonian:

$$H = \sum_{\mathbf{k}} \epsilon_{\mathbf{k}} c_{\mathbf{k}}^{\dagger} c_{\mathbf{k}} + \sum_{\nu, \mathbf{q}} \omega_{\nu}(\mathbf{q}) a_{\mathbf{q}, \nu}^{\dagger} a_{\mathbf{q}, \nu} + \sum_{\mathbf{k}, \mathbf{q}, \nu} \lambda(\mathbf{k}, \mathbf{q}, \nu) c_{\mathbf{k}+\mathbf{q}}^{\dagger} c_{\mathbf{k}} (a_{-\mathbf{q}, \nu}^{\dagger} + a_{\mathbf{q}, \nu}) \quad (4.44)$$

where $\lambda(\mathbf{k}, \mathbf{q}, \nu)$ is the general form of electron-phonon coupling and the index ν represents the polarization of the phonon.

The two most famous simplified versions of this Hamiltonian are the Fröhlich and the Holstein models [38, 79]. The Fröhlich solution is applicable for long-range electron-lattice interaction where particles are lightly dressed and weakly polarize the environment on a large spatial extend around themselves. The Holstein model assumes a one electron-site coupling of the electrons with dispersionless lattice vibration modes, thus dealing with short range electron-lattice interaction. The concept of polaron, introduced by Landau [80], and that represents an electron moving in a polarizable lattice carrying the lattice deformation with it, is often used to distinguish between the Fröhlich and the Holstein models: one speaks of large polarons in the former model and of small polarons in the latter one. Since when increasing the strength of the coupling the polaron radius shrinks to a single lattice site, the Holstein model is more adapted to study strong interaction.

Recently some numerical works have addressed this Holstein problem [37, 39, 40, 81]. These numerical approaches give the possibility to simulate the spectral function in regions where the perturbation theory fails. The authors of these works are particularly interested in the crossover between weak and strong coupling in the adiabatic limit as well as in the effect of the system filling on the spectral function. We want here to compare the principal results of these more realistic models with our previous independent bosons picture.

The patterns in Fig. 4.18 illustrate the spectral function found at half filling for the weak and strong coupling limits. In the weak coupling scheme, most of the spectral weight near k_F resides on the polaronic quasiparticle. The dispersion of this band exhibits a mass enhancement due to the weak-dressing of the electron. Further from \mathbf{k}_F the polaron band is no more visible since most of the spectral weight is transferred to the incoherent band which follows the bare dispersion $\epsilon(\mathbf{k})$. For strong coupling the spectrum consists again of the polaronic quasiparticle and the coherent part. But as a consequence of the predominantly local effects in strong coupling region, the polaron band contains almost zero electronic spectral weight for the whole momentum range and turns to a very narrow band. The incoherent part where the electronic spectral weight is concentrated also changes: it becomes broader and is composed of a multi-peak structure in a similar manner as the previous model of independent bosons. Also, as shown in Fig. 4.17, the incoherent band does not cross the Fermi level but flattens in its proximity inducing the opening of a pseudogap. We remark that although the polaron band crosses the Fermi level the system becomes insulating since these states have a vanishingly small electronic character.

In summary, it appears that a relatively strong coupling between electrons and phonon modes can explain the unusual spectral behaviour observed in numerous materials and especially in the

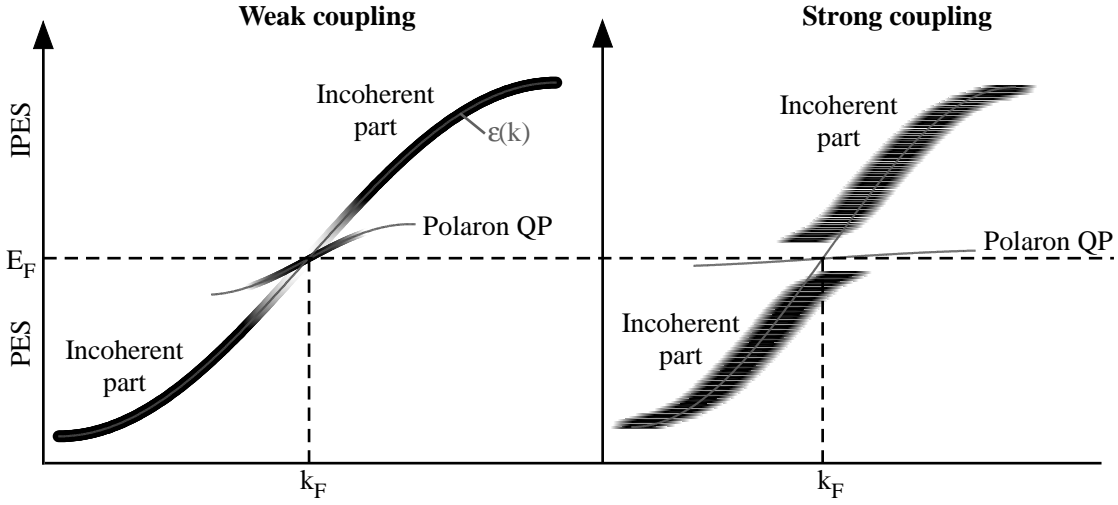


Figure 4.18: Sketch of the spectral functions derived from the numerical resolution of the Holstein problem for the two limits of weak and strong coupling.

1*T*-TaS₂. As proposed in section 4.4 and in reference to the above presentation, the coupling with dispersionless optical phonons is a valid candidate to explain the removal of the whole Fermi surface observed in this compound. However the strength of the coupling remains an open question and demands additional experimental works such as fine optical measurements. Nevertheless a first rough estimation of λ is possible thanks the following relation between the coupling constant and the CDW gap Δ_{CDW}

$$\Delta_{CDW} = 2\epsilon_F e^{-1/\lambda}. \quad (4.45)$$

We find for the Ta5d band perpendicular to the Γ -M direction a λ of the order of unity, which corresponds to the theoretical limit for the formation of a small polaron in the adiabatic limit.

4.6 Summary

Peierls early pointed out the importance of the high anisotropy of the band structure for inducing the CDW ground state. Indeed the strongly divergent response function of 1D systems, which is due to the peculiar FS topology, is the starting key to the formation of such a ground state. Therefore, it is not surprising that an explanation for the occurrence of CDW in higher dimensional systems has been first looked for in the topology of FS, in order to find good nesting conditions. And indeed, this explanation fits well for 2D systems that have a quasi-1D character, like purple bronze (KM₀₆O₁₇) where a hidden 1D FS has been found [82]. However for true 2D systems, such as 1*T*-TaS₂, the topology of the FS presents only imperfectly parallel parts, thus it is strongly questioning whether it is sufficient to account for the CDW formation.

In this thesis, we identify several points that could explain the complex behaviour of 1*T*-TaS₂. First, with the point of view of a generalization of the 1D Peierls scenario, we expect that the nesting is strong enough to induce the instability, and we explain the particular "stars-of-David" superstructure by putting forward that this configuration maximizes the energy gain thanks to its many small BZs cutting the FS and therefore creating many small gaps. Second, by identifying "stars-of-David" as small molecules, we argue that strong electron-phonon correlation plays an important role in the complex phase diagram of the 1*T*-TaS₂. We conclude by noting that an unified explanation will probably be found in the fusion of the Peierls nesting scenario with a molecular orbital approach.

References for chapter 4

- [1] R. E. Peierls, *Quantum Theory of Solids* (Oxford University Press, Oxford, 1955).
- [2] G. Grüner, *Density Waves in Solids* (Addison-Wesley, Massachusetts, 1994).
- [3] A. J. Berlinsky, Rep. Prog. Phys. **42**, 1243 (1979).
- [4] S. Kagoshima, H. Nagasawa, T. Sambongi, *One-Dimensional Conductors*, Solid-State Sciences 72,(Springer-Verlag, 1982)
- [5] W. Kohn, Phys. Rev. Lett. **2**, 393 (1959).
- [6] N. W. Ashcroft and N. D. Mermin, *Solid State Physics* (Holt, New-York, 1976).
- [7] G. D. Mahan, *Many-Particle Physics*(Plenum Press, New York, 1981).
- [8] A. Kaminski, S. Rosenkranz, H. M. Fretwell, J. C. Campuzano, Z. Li, H. Raffy, W. G. Cullen, H. You, C. G. Olson, C. M. Varma, H. Höchst, Nature **416**, 610 (2002).
- [9] B. Lake, H. M. Rønnow, N. B. Christensen, G. Aeppli, K. Lefmann, D. F. McMorrow, P. Vorderwisch, P. Smeibidl, N. Mangkorntong, T. Sasagawa, M. Nohara, H. Takagi, T. E. Mason, Nature **415**, 299 (2002).
- [10] A.H. Castro Neto, Phys. Rev. Lett. **86**, 4382 (2001).
- [11] T. Yokoya, T. Kiss, A. Chainani, S. Shin, M. Nohara, H. Takagi, Science **294**, 2518 (2001).
- [12] J.A. Wilson, A.D. Yoffe, Adv. Phys. **18**, 193 (1969).
- [13] J.A. Wilson, F.J. Di Salvo, S. Mahajan, Adv. Phys. **24**, 117 (1975).
- [14] Th. Pillo *et al.*, J. Electr. Spectrosc. Relat. Phenom. **97**,243 (1998) .
- [15] P. Aebi, J. Osterwalder, P. Schwaller, L. Schlapbach, M. Shimoda, T. Mochiku and K. Kadowaki, Phys. Rev. Lett. **72**, 2757 (1994) .
- [16] B. Dardel, M. Grioni, D. Malterre, P. Weibel, Y. Baer, F. Lévy, Phys. Rev. B **45**, 1462 (1992).
- [17] B. Dardel, M. Grioni, D. Malterre, P. Weibel, Y. Baer, F. Lévy, Phys. Rev. B **46**, 7407 (1992).
- [18] P. Blaha, K. Schwarz, and J. Luitz, **WIEN97**, A Full Potential Linearized Augmented Plane Wave Package for Calculating Crystal Properties (Karlheinz Schwarz, Techn. Universität Wien, Austria), 1999. ISBN 3-9501031-0-4.
- [19] J. P. Perdew, K. Burke, M. Ernzerhof, Phys. Rev. Lett. **77**, 3865 (1996).
- [20] Here, different values for both work function and inner potential were tested; however no relevant changes came out, as a consequence of the quasi-two dimensional character of these materials.
- [21] X. M. Wu, C. M. Lieber, Science **243**, 1703 (1989).

- [22] A. Spijkerman, Jan L. de Boer, Auke Meetsma, Gerrit A. Wiegers and Sander van Smaalen, Phys. Rev. B **56**, 13757 (1997).
- [23] M. Bovet, S. van Smaalen, H. Berger, R. Gaal, L. Forró, L. Schlapbach, P. Aebi, Phys. Rev. B **67**, 125105 (2003).
- [24] J. Voit, L. Perfetti, F. Zwick, H. Berger, G. Margaritondo, G. Grüner, H. Höchst, M. Grioni, Science **290**, 501 (2000).
- [25] N.V. Smith and M.M. Traum, Phys. Rev. B **11**, 2087 (1975).
- [26] Th. Pillo, J. Hayoz, H. Berger, M. Grioni, L. Schlapbach, and P. Aebi, Phys. Rev. Lett. **83**, 3494 (1999).
- [27] M. Bovet, D. Popovic, F. Clerc, C. Koitzsch, U. Probst, E. Bucher, H. Berger, D. Naumovic, and P. Aebi, Phys. Rev. B **69**, 125117 (2004).
- [28] H. W. Myron and A. J. Freeman, Phys. Rev. B **11**, 2735 (1975).
- [29] N.V. Smith, S.D. Kevan, F.J. Di Salvo, J. Phys. C **18**, 3175 (1985).
- [30] P. Fazekas and E. Tosatti, Philos. Mag.B **39**, 229 (1979).
- [31] P. Fazekas and E. Tosatti, Physica B **99**, 183 (1980).
- [32] D. S. Dessau, T. Saitoh, C.-H. Park, Z.-X. Shen, P. Villella, N. Hamada, Y. Moritomo and Y. Tokura Journal of Superconductivity **12**, 273 (1999).
- [33] A. Lanzara, P. V. Bogdanov, X. J. Zhou, S.A. Kellar, D. L. Feng, E. D. Lu, T. Yoshida, H. Eisaki, A. Fujimori, K. Koshio, J.-I. Shimoyama, T. Noda, S. Uchida, Z. Hussain and Z.-X. Shen, Nature **412**, 510 (2001).
- [34] K. Nakanishi and H. Shiba, J. Phys. Soc. Jpn. **53**, 1103 (1984).
- [35] A. M. Woolley and G. Wexler, J. Phys. C **10**, 2601 (1977).
- [36] F. Clerc, M. Bovet, H. Berger, L. Despont, C. Koitzsch, M. G. Garnier and P. Aebi, Physica B **351**, 245 (2004).
- [37] M. Hohenadler, D. Neuber, W. von der Linden, G. Wellein, J. Loos, and H. Fehske, Phys. Rev. B **71**, 245111 (2005).
- [38] T. Holstein, Ann.Phys. **8**, 325 (1959).
- [39] S. Sykora, A. Hübsch, K. W. Becker, G. Wellein, and H. Fehske, Phys. Rev. B **71**, 045112 (2005).
- [40] M. Hohenadler, M. Aichhorn, and W. von der Linden, Phys. Rev. B **68**, 184304 (2003).
- [41] C. Ambrosch-Draxl and J. O. Sofo (2004), cond-mat/0402523.
- [42] A. W. Overhauser, Phys. Rev. B **3**, 3173 (1971).
- [43] C. B. Scruby, P. M. Williams, and G. S. Parry, Philos. Mag **31**, 255 (1975).
- [44] T. Ishiguro and H. Sato, Phys. Rev. B **44**, 2046 (1991).

- [45] R.E.Thomson, B.Burk, A.Zettl, and J.Clarke, Phys. Rev. B **49**, 16899 (1994).
- [46] W. L. McMillan, Phys. Rev. B **14**, 1496 (1976).
- [47] X. L. Wu and C. M. Lieber, Phys. Rev. Lett. **64**, 1150 (1990).
- [48] B. Burk, R. E. Thomson, A. Zettl, and J. Clarke, Phys. Rev. Lett. **66**, 3040 (1991).
- [49] F. Zwick, H. Berger, I. Vobornik, G. Margaritondo, L. Forro amd C. Beeli, M. Onellion, G. Panaccione, A. Taleb, and M. Grioni, Phys. Rev. Lett. **81**, 001058 (1998).
- [50] C. Koitzsch, J. Hayoz, M. Bovet, F. Clerc, L. Despont, C. Ambrosch-Draxl and P. Aebi, Phys. Rev. B **70**, 165114 (2004).
- [51] C. Battaglia, H. Cercellier, F. Clerc, L. Despont, M. G. Garnier, C. Koitzsch, H. Berger, L. Forró and P. Aebi, Phys. Rev. B **72**, (2005) to be published.
- [52] H. W. Myron, J. Rath, and A. J. Freeman, Phys. Rev. B **15**, 885 (1977).
- [53] M. D. Johannes, I. I. Mazin and C. A. Howells (2005), cond-mat/0510390.
- [54] M. R. Norman, H. Ding, M. Randeria, J. C. Campuzano, T. Yokoya, T. Takeuchi, T. Takahashi, T. Mochiku, K. Kadowaki, P. Guptasarma and D. G. Hinks, Nature **392**, 157 (1998).
- [55] J. Mesot, M. Randeria, M. R. Norman, A. Kaminski, H. M. Fretwell, J. C. Campuzano, H. Ding, T. Takeuchi, T. Sato, T. Yokoya, T. Takahashi, I. Chong, T. Terashima, M. Takano, T. Mochiku and K. Kadowaki, Phys. Rev. B **63**, 224516 (2001).
- [56] L. Perfetti, H. Berger, A. Reginaldi, L. Degiorgi, H. Hochst, J. Voit, G. Margaritondo, and M. Grioni, Phys. Rev. Lett. **87**, 216404 (2001).
- [57] L. Perfetti, S. Mitrovic, G. Margaritondo, M. Grioni, L. Forro, L. Degiorgi, and H. Hochst, Phys. Rev. B **66**, 075107 (2002).
- [58] D. Emin, Phys. Rev. B **48**, 13691 (1993).
- [59] Th. Pillo, J. Hayoz, D. Naumovic, H. Berger, L. Perfetti, L. Gavioli, A. Taleb-Ibrahimi, L. Schlapbach and P. Aebi, Phys. Rev. B **64**, 245105 (2001).
- [60] L. Perfetti, T. A. Gloor, F. Mila, H. Berger, and M. Grioni, Phys. Rev. B **71**, 153101 (2005).
- [61] G. Sangiovanni, M. Capone, C. Castellani, and M. Grilli, Phys. Rev. Lett. **94**, 026401 (2005).
- [62] L. V. Gasparov, K. G. Brown, A. C. Wint, D. B. Tanner, H. Berger, G. Margaritondo, R. Gaál and L. Forró , Phys. Rev. B **66**, 094301 (2002).
- [63] M. Grioni, Ch. R. Ast, D. Pacilé, M. Papagno, H. Berger and L. Perfetti, New Journal of Physics **7**, 106 (2005).
- [64] E. Rotenberg, W. Theis, K. Horn and P. Gille, Nature **406**,602 (2000).
- [65] R. Claessen, R. O. Anderson, J. W. Allen, C. G. Olson, C. Janowitz, W. P. Ellis, S. Harm, M. Kalning, R. Manzke and M. Skibowski, Phys. Rev. Lett. **69**, 808 (1992)

- [66] J.-M. Imer, F. Patthey, B. Dardel, W.-D. Schneider and Y. Baer Phys. Rev. Lett. **62**, 336 (1989)
 - [67] C. G. Olson, R. Liu, A.-B. Yang, D. W. Lynch, A. J. Arko, R. S. List, B. W. veal, Y. C. Chang, P. Z. Jiang and A. P. Paulikas, Science **245**,731 (1989).
 - [68] Z.-X. Shen, D. S. Dessau, B. O. Wells, D. M. King, W. E. Spicer, A. J. Arko, D. Marshall, L. W. Lombardo, A. Kapitulnik, P. Dickinson, S. Doniach, J. DiCarlo, A. G. Loeser and C. H. Park Phys. Rev. Lett. **70**, 1553 (1993)
 - [69] M. Hengsberger, D. Parudie, P. Segovia, M. Garnier and Y. Baer, Phys. Rev. Lett. **83**, 592 (1999)
 - [70] S. LaShell, E. Jensen and T. Balasubramanian, Phys. Rev. B **61**, 2371 (2000)
 - [71] T. Balasubramanian, E. Jensen, X. L. Wu and S. L. Hulbert, Phys. Rev. B **75**, R6866 (1998)
 - [72] D. S. Dessau, T. Saitoh, C.-H. Park, Z.-X. Shen, P. Villella, N. Hamada, Y. Moritomo and Y. Tokura, Phys. Rev. Lett. **81**, 192 (1998)
 - [73] N. Mannella, W. L. Yang, X. J. Zhou, H. Zheng, J. F. Mitchell, J. Zaanen, T. P. Devereaux, N. Nagaosa, Z. Hussain and Z.-X. Shen, Nature **438**, 474 (2005).
 - [74] Z.-X. Shen, P. Villella and J. R. Schrieffer, Phys. Rev. Lett. **78**, 1771 (1997)
 - [75] K. M. Shen, F. Ronning, D. H. Lu, W. S. Lee, N. J. C. Ingle, W. Meevasana, F. Baumberger, A. Damascelli, N. P. Armitage, L. L. Miller, Y. Kohsaka, M. Azuma, M. Takano, H. Takagi and Z.-X. Shen, Phys. Rev. Lett. **93**, 267002 (2004)
 - [76] L. Perfetti, H. Berger, A. Reggiani, L. Degiorgi, H. Hochst, J. Voit, G. Margaritondo, and M. Grioni, Phys. Rev. Lett. **87**, 216404 (2001).
 - [77] L. Perfetti, S. Mitrovic, G. Margaritondo, M. Grioni, L. Forro, L. Degiorgi, and H. Hochst, Phys. Rev. B **66**, 075107 (2002).
 - [78] A. Damascelli, Z. Husain and Z.-X. Shen, Rev. Mod. Phys. **75**, 473 (2003).
 - [79] H. Fröhlich, Adv.Phys. **3**, 325 (1954).
 - [80] L. Landau, Z. Phys. **3**, 664 (1933).
 - [81] A. Macridin, *Phonons, Charge and Spin in Correlated Systems*, PhD thesis, University of Groningen, Groningen (2003).
 - [82] G. -H. Gweon, J. W. Allen, J. A. Clack, Y. X. Zhang, D. M. Poirier, P. J. Benning, C. G. Olson, J. Marcus and C. Schlenker Phys. Rev. B **55**, R13353 (1997).
-

Chapter 5

1*T*-TiSe₂, an excitonic insulator?

5.1 Introduction

Among the transition metal dichalcogenides, 1*T*-TiSe₂ exhibits an interesting phase diagram due to the formation of a CDW. Indeed upon cooling down from room temperature, this compound undergoes at $T_C \approx 200$ K a second-order phase transition into a commensurate CDW phase associated with a (2x2x2) superlattice. The three CDW vectors connect the Γ point with the L points of the hexagonal BZ represented in Fig. 5.1 (a) As illustrated in Fig. 5.1 (b), at these high symmetry points, the DFT-calculated electronic structure predicts a Se 4p-derived valence band maximum at Γ and a Ti 3d-derived conduction band minimum at L. Therefore the FS consists of hole pockets at Γ and electron pockets at L (and equivalent points)(Fig. 5.1 (c)). Although 1*T*-TiSe₂ is one of the simplest and most studied transition metal dichalcogenides, the driving force of the CDW formation remains a puzzle after decades of research. In this lively discussion on the origin of the CDW instability in 1*T*-TiSe₂ several mechanisms have been suggested: (i) DiSalvo [1] proposed the simple nesting model, explaining the instability by nesting between Γ -point holes and L-points electrons. However the hole pocket at Γ is different in size and shape from the electron pocket at L and thus no large parallel FS portions are expected. Therefore this model did not receive much support. (ii) In view of the unusual large lattice polarizability of 1*T*-TiSe₂, White and Lucowsky [2] suggested an antiferroelectric transition driving the phonon mode soft. (iii) Hughes [3] proposed a band-type Jahn-Teller mechanism based on the observed atomic displacements during the structural phase transition of 1*T*-TiSe₂: the local coordination of the Ti atom changes from octahedral (1*T*) towards trigonal prismatic (2*H*) and the lowest lying degenerate d-derived bands are split, with a nondegenerate level shifting down in energy. Due to the partial filling of these d levels the system is expected to reduce its total energy through the coordination change. Later Whangbo and Canadell [4] refined this approach of a structural change inducing energy lowering and pointed out that the energy gain is associated with the shortening of the Ti-Se bond and does not occur in the Ti 3d-derived bands but rather in the Se 4p-derived bands. (iv) The last explanation was suggested by Wilson [5] who proposed 1*T*-TiSe₂ to be the first example of an excitonic insulator. Within this model, if the number of carriers is sufficiently small, the screening of the Coulomb interaction between electrons and holes is weak and the system becomes unstable upon the formation of weakly bound electron-hole pairs, called excitons [6].

Among these four scenarios, The last two have attracted much attention. However, despite numerous experimental works [7–11], it appears still difficult to favour one mechanism rather than another. Moreover a combination of these scenarios cannot be ruled out.

The aim of this chapter is to establish the existence or not of excitons in 1*T*-TiSe₂. Thus in the following section, we develop the exciton theory and we study in detail the expected spectral function in presence of an exciton condensate as well as in the case of fluctuating excitons. After

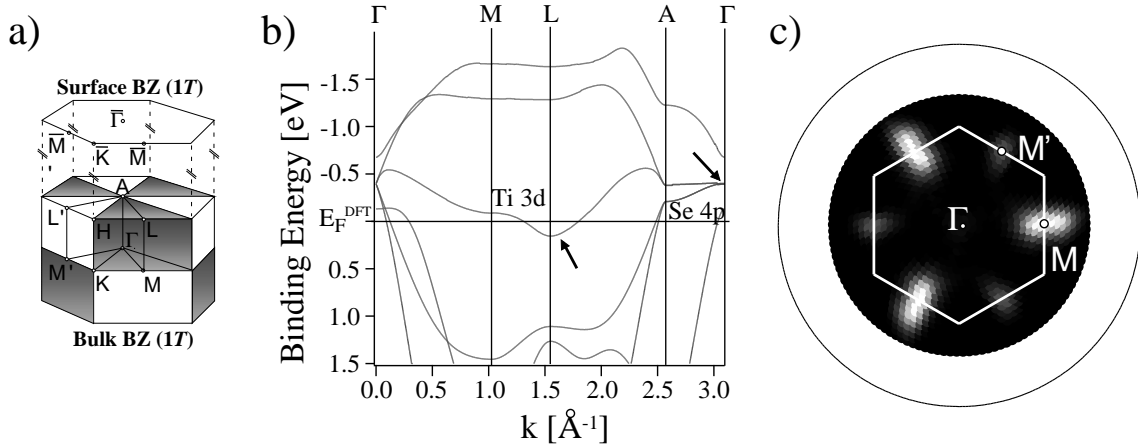


Figure 5.1: (a) Surface and bulk Brillouin zone of the 1T structure. (b) DFT band calculation for the 1T-TiSe₂. (c) Fermi surface mapping of 1T-TiSe₂ at room temperature with high intensity in white. The normal state BZ is superimposed on the FSM.

the presentation of the theory, we confront our ARPES data to the theoretical predictions and track possible traces of excitons.

5.2 Excitons and spectral function

Formation of electron-hole bound pairs was proposed for the first time by Mott for semimetals [12] and by Knox for semiconductors [13]. Mott pointed out that if the number of carriers is sufficiently small the Coulomb interaction between electrons and holes is weakly screened, leading to a nonconducting electron-hole bound state. Knox considered an indirect-band-gap semiconductor and has predicted the spontaneous formation of excitons when the gap energy E_G becomes less than the binding energy of an exciton E_B .

Starting from these observations several works argued in favour of a new possible distorted insulating phase - the excitonic phase - in solids with small energy-band-gaps (positive or negative) and at sufficiently low temperature ($k_B T$ smaller than the electron-hole binding energy). The theory of this excitonic phase was first developed by des Cloizeaux [14] and Keldysh and Kopaev [15]. Further developments have been worked out by Zittartz [16, 17], Jérôme, Rice and Kohn [18] and Halperin [19] where the authors deal with a formalism analogous to the BCS theory of superconductivity. The following of this section, whose aim is to derive the spectral function, is largely inspired from these latest theoretical works.

5.2.1 The electron-hole system

To develop the theory of the excitonic insulator, we assume as a starting point the band structure depicted in Fig. 5.2, which consists in a single valence band centred at Γ ($\mathbf{k}=0$) and a single conduction band with its minimum at M ($\mathbf{k}=\mathbf{w}$). The dispersions for the valence and the conduction bands are respectively:

$$\begin{aligned}\epsilon_a(\mathbf{k}) &= -E_a - \frac{\mathbf{k}^2}{2m_a} \\ \epsilon_b(\mathbf{k}, \mathbf{w}) &= E_b + \frac{(\mathbf{k} - \mathbf{w})^2}{2m_b}.\end{aligned}$$

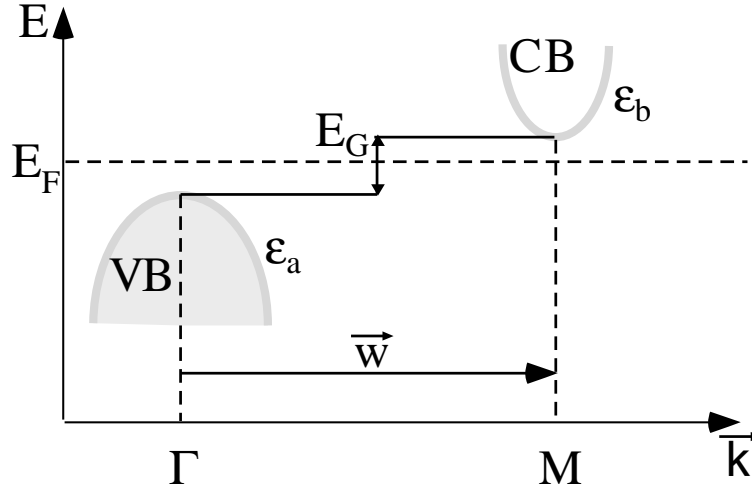


Figure 5.2: Sketch of the two bands model used in our derivation of the excitonic scenario. The valence band (VB) and conduction band (CB) are centred in Γ and M , respectively, and their dispersions are given by ϵ_a and ϵ_b

The indirect gap, positive or negative, is therefore $E_G = E_a + E_b$. We suppose the following Hamiltonian for the electron-hole system:

$$H = H_0 + W$$

where

$$H_0 = \sum_{\mathbf{k}} \epsilon_a(\mathbf{k}) a^\dagger(\mathbf{k}) a(\mathbf{k}) + \sum_{\mathbf{k}, \mathbf{w}} \epsilon_b(\mathbf{k}, \mathbf{w}) b^\dagger(\mathbf{k} + \mathbf{w}) b(\mathbf{k} + \mathbf{w}).$$

Here the $a(\mathbf{k}), a^\dagger(\mathbf{k})$ and $b(\mathbf{k} + \mathbf{w}), b^\dagger(\mathbf{k} + \mathbf{w})$ are annihilation and creation operators of valence and conduction electrons with momentum \mathbf{k} and $\mathbf{k} + \mathbf{w}$, respectively. The interaction part of H contains only the direct Coulomb interaction inbetween electrons in valence or conduction bands. W thus reads

$$W = \sum_{\mathbf{q}, \mathbf{w}} \rho_a(\mathbf{q}) V_c(\mathbf{q}) \rho_{b, \mathbf{w}}^+(\mathbf{q})$$

where $\rho_a(\mathbf{q})$ and $\rho_{b, \mathbf{w}}(\mathbf{q})$ are the usual density operators :

$$\rho_a(\mathbf{q}) = \sum_{\mathbf{k}} a^\dagger(\mathbf{k} + \mathbf{q}) a(\mathbf{k})$$

and

$$\rho_{b, \mathbf{w}}(\mathbf{q}) = \sum_{\mathbf{k}} b^\dagger(\mathbf{k} + \mathbf{w} + \mathbf{q}) b(\mathbf{k} + \mathbf{w}).$$

At this stage we can introduce two Green's functions, one for electrons propagating in the valence band G_a and one for electrons from the conduction band G_b

$$G_a(\mathbf{p}, t, t') = (-i) \langle T a(\mathbf{p}, t) a^\dagger(\mathbf{p}, t') \rangle \quad (5.1)$$

$$G_b(\mathbf{k} + \mathbf{w}, t, t') = (-i) \langle T b(\mathbf{k} + \mathbf{w}, t) b^\dagger(\mathbf{k} + \mathbf{w}, t') \rangle \quad (5.2)$$

We also define here the so-called anomalous Green's functions whose introduction will be justified later

$$F(\mathbf{k}, \mathbf{w}, t, t') = (-i) \langle T b(\mathbf{k} + \mathbf{w}, t) a^\dagger(\mathbf{k}, t') \rangle \quad (5.3)$$

$$F^+(\mathbf{k}, \mathbf{w}, t, t') = (-i) \langle T a(\mathbf{k}, t) b^\dagger(\mathbf{k} + \mathbf{w}, t') \rangle \quad (5.4)$$

5.2. Excitons and spectral function

These two functions combine annihilation and creation operators of distinct bands, and are therefore zero in the normal state of the system. However if excitons appear in the system these functions will not be zero anymore and will carry some information. The electronic operators satisfy the following equations of motion

$$i\frac{\partial}{\partial t}a(\mathbf{p}, t) = \epsilon_a(\mathbf{p})a(\mathbf{p}, t) + \sum_{\mathbf{q}, \mathbf{k}, \mathbf{w}} V_c(\mathbf{q})a(\mathbf{p} + \mathbf{q})b^+(\mathbf{k} + \mathbf{w})b(\mathbf{k} + \mathbf{w} - \mathbf{q}) \quad (5.5)$$

$$i\frac{\partial}{\partial t}b(\mathbf{p} + \mathbf{w}, t) = \epsilon_b(\mathbf{p} + \mathbf{w})b(\mathbf{p} + \mathbf{w}, t) + \sum_{\mathbf{q}, \mathbf{k}} V_c(\mathbf{q})a^+(\mathbf{k} + \mathbf{q})a(\mathbf{k})b(\mathbf{p} + \mathbf{w} + \mathbf{q}) \quad (5.6)$$

5.2.2 Exciton physics

From the field operators $\psi_b^+(\mathbf{x})$ and $\psi_a(\mathbf{x}')$ which create a conduction electron at \mathbf{x} and a hole in the valence band at \mathbf{x}' , respectively, one can construct the exciton creation operator $A^+(\mathbf{x}, \mathbf{x}')$ as

$$\begin{aligned} A^+(\mathbf{x}, \mathbf{x}') &= \psi_b^+(\mathbf{x})\psi_a(\mathbf{x}') \\ &= \sum_{\mathbf{k}_1, \mathbf{k}_2, \mathbf{w}} e^{-i(\mathbf{k}_1 + \mathbf{w})\mathbf{x}} e^{i\mathbf{k}_2\mathbf{x}'} b^+(\mathbf{k}_1 + \mathbf{w})a(\mathbf{k}_2). \end{aligned} \quad (5.7)$$

With introduction of relative and center of mass coordinates $\mathbf{u} = \mathbf{x} - \mathbf{x}'$ and $\mathbf{R} = \alpha\mathbf{x} + \beta\mathbf{x}'$ where $\alpha = \frac{m_b}{M}$, $\beta = \frac{m_a}{M}$ and $M = m_a + m_b$, the exciton creation operator becomes

$$A^+(\mathbf{R}, \mathbf{u}) = \sum_{\mathbf{Q}, \mathbf{p}, \mathbf{w}} e^{-i(\mathbf{Q} + \mathbf{w})\mathbf{R}} e^{-i(\mathbf{p} + \beta\mathbf{w})\mathbf{u}} b^+(\mathbf{p} + \alpha\mathbf{Q} + \mathbf{w})a(\mathbf{p} - \beta\mathbf{Q}) \quad (5.8)$$

where $\mathbf{Q} = \mathbf{k}_1 - \mathbf{k}_2$ is the centre of mass momentum and $\mathbf{p} = \alpha\mathbf{k}_2 + \beta\mathbf{k}_1$. In a similar way, it is possible to write the electron-hole pair operator in term of exciton operator:

$$b^+(\mathbf{p} + \alpha\mathbf{Q} + \mathbf{w})a(\mathbf{p} - \beta\mathbf{Q}) = \sum_{\lambda} \varphi_{\lambda}^*(\mathbf{p}, \mathbf{w})A_{\lambda}^+(\mathbf{Q}, \mathbf{w}) \quad (5.9)$$

The field operator $A_{\lambda}^+(\mathbf{Q}, \mathbf{w})$ creates an exciton of eigenstate λ with centre of mass momentum \mathbf{Q} and with the electron located in the conduction band near \mathbf{w} . The inverse relation of (5.9) leads to:

$$A_{\lambda}^+(\mathbf{Q}, \mathbf{w}) = \sum_{\mathbf{p}} \varphi_{\lambda}^*(\mathbf{p}, \mathbf{w})b^+(\mathbf{p} + \alpha\mathbf{Q} + \mathbf{w})a(\mathbf{p} - \beta\mathbf{Q}) \quad (5.10)$$

$\varphi_{\lambda}(\mathbf{p}, \mathbf{w})$ is the exciton wave function and is a bound eigenstate of the following elementary Schrödinger equation for the electron-hole relative motion in \mathbf{k} space [20]:

$$\left[\frac{p^2}{2\mu} - E_{\lambda}\right]\varphi_{\lambda}(\mathbf{p}, \mathbf{w}) = \sum_{\mathbf{p}'} V_c(\mathbf{p} - \mathbf{p}')\varphi_{\lambda}(\mathbf{p}, \mathbf{w}) \quad (5.11)$$

where E_{λ} is the energy of the relative motion state φ_{λ} and μ is the reduced mass, $\frac{1}{\mu} = \frac{1}{m_a} + \frac{1}{m_b}$. φ_{λ} has the same form as the solution of the hydrogen atom problem.

The dynamics of excitons is described by the equation of motion:

$$i\frac{\partial}{\partial t}A_{\lambda}^+(\mathbf{Q}, \mathbf{w}) = i\frac{\partial}{\partial t} \sum_{\mathbf{p}} \varphi_{\lambda}^*(\mathbf{p}, \mathbf{w})b^+(\mathbf{p} + \alpha\mathbf{Q} + \mathbf{w})a(\mathbf{p} - \beta\mathbf{Q}) \quad (5.12)$$

With help of the time dependence of the electron and hole operators (5.6) and the addition of a reasonable interacting term [20], (5.12) becomes:

$$\begin{aligned}
 i\frac{\partial}{\partial t}A_{\lambda}^{+}(\mathbf{Q}, \mathbf{w}) &= -\sum_{\mathbf{p}}[E_G + \frac{p^2}{2\mu} + \frac{Q^2}{2M}]\varphi_{\lambda}^{*}(\mathbf{p}, \mathbf{w})b^{+}(\mathbf{p} + \alpha\mathbf{Q} + \mathbf{w})a(\mathbf{p} - \beta\mathbf{Q}) \\
 &+ \sum_{\mathbf{p}'}V_c(\mathbf{p} - \mathbf{p}')\varphi_{\lambda}^{*}(\mathbf{p}', \mathbf{w})b^{+}(\mathbf{p}' + \alpha\mathbf{Q} + \mathbf{w})a(\mathbf{p}' - \beta\mathbf{Q})
 \end{aligned} \quad (5.13)$$

Finally with introduction of (5.11) one finds the following result for the exciton equation of motion

$$i\frac{\partial}{\partial t}A_{\lambda}^{+}(\mathbf{Q}, \mathbf{w}) = -[\frac{Q^2}{2M} + E_{\lambda} + E_G]A_{\lambda}^{+}(\mathbf{Q}, \mathbf{w}) \quad (5.14)$$

With this last expression we can easily derive the excitonic Green's function $G_{\lambda}^{ex}(\mathbf{Q}, t, t')$ which will be useful for the rest of this theory

$$\begin{aligned}
 G_{\lambda}^{ex}(\mathbf{Q}, t, t') &= (-i) \langle TA_{\lambda}(\mathbf{Q}, t)A_{\lambda}^{+}(\mathbf{Q}, t') \rangle \\
 G_{\lambda}^{ex}(\mathbf{Q}, z) &= \frac{1}{z - \frac{Q^2}{2M} - \epsilon_{\lambda}}
 \end{aligned} \quad (5.15)$$

where $\epsilon_{\lambda} = E_{\lambda} + E_G$.

5.2.3 Condensate phase

By analogy to the theory of superconductivity, in the excitonic state the excitons behave as a condensate in the lowest energy state, namely the state with zero momentum $\mathbf{Q}=0$. At finite temperature excitons may be described by the thermal average of the electron-hole pair operator (5.9) which for an exciton condensate is

$$\begin{aligned}
 \langle b^{+}(\mathbf{p} + \alpha\mathbf{Q} + \mathbf{w})a(\mathbf{p} - \beta\mathbf{Q}) \rangle &= \delta_{\mathbf{Q},0}\varphi_0^{*}(\mathbf{p}, \mathbf{w}) \langle A_0^{+}(0, \mathbf{w}) \rangle \\
 &= \delta_{\mathbf{Q},0}\varphi_0^{*}(\mathbf{p}, \mathbf{w})\xi_0^{*}(\mathbf{w}).
 \end{aligned} \quad (5.16)$$

The square modulus of $\langle A_0^{+}(0, \mathbf{w}) \rangle = \xi_0^{*}(\mathbf{w})$ is indicative of the intensity of the exciton formation. The change of the initial band structure of Fig. 5.2 due to the presence of an exciton condensate can be revealed by the Green's functions $G_a(\mathbf{p}, t, t')$ and $G_b(\mathbf{k} + \mathbf{w}, t, t')$ defined in (5.2). The equation of motion of the valence band Green's function is derived from the time dependence of the operator $a(\mathbf{p}, t)$ and is

$$[i\frac{\partial}{\partial t} - \epsilon_a(\mathbf{p})]G_a(\mathbf{p}, t, t') = \delta(t - t') - i \sum_{\mathbf{k}, \mathbf{q}, \mathbf{w}} V_c \langle Ta(\mathbf{p} + \mathbf{q}, t)b^{+}(\mathbf{k} + \mathbf{w}, t)b(\mathbf{k} + \mathbf{w} - \mathbf{q}, t)a^{+}(\mathbf{p}, t') \rangle \quad (5.17)$$

Evaluation of the time ordered bracket in (5.17) is accomplished with use of Wick's theorem which states that, for free particle, such a bracket may be evaluated by expanding it into all possible pairings. That gives:

$$\begin{aligned}
 &\langle Ta(\mathbf{p} + \mathbf{q}, t)b^{+}(\mathbf{k} + \mathbf{w}, t)b(\mathbf{k} + \mathbf{w} - \mathbf{q}, t)a^{+}(\mathbf{p}, t') \rangle = \\
 &- \langle b^{+}(\mathbf{k} + \mathbf{w})a(\mathbf{p} + \mathbf{q}) \rangle \langle Tb(\mathbf{k} + \mathbf{w} - \mathbf{q}, t)a^{+}(\mathbf{p}, t') \rangle \\
 &- \langle Ta^{+}(\mathbf{p}, t')a(\mathbf{p} + \mathbf{q}) \rangle \langle b^{+}(\mathbf{k} + \mathbf{w})b(\mathbf{k} + \mathbf{w} - \mathbf{q}) \rangle \\
 &- \langle a(\mathbf{p} + \mathbf{q})b(\mathbf{k} + \mathbf{w} - \mathbf{q}) \rangle \langle Tb^{+}(\mathbf{k} + \mathbf{w}, t)a^{+}(\mathbf{p}, t') \rangle
 \end{aligned} \quad (5.18)$$

5.2. Excitons and spectral function

where the sign in front of each pair is determined by the number of operator permutations, negative for an odd number and else positive. The last combination of pairs in (5.18) is evidently zero and the one before is the usual Hartree-Fock term which will be exactly compensated by the potential of the ions background. Moreover with suitable variable substitution, the equation of motion (5.17) reads

$$[i\frac{\partial}{\partial t} - \epsilon_a(\mathbf{p})]G_a(\mathbf{p}, t, t') = \delta(t - t') + i \sum_{\mathbf{q}, \mathbf{w}} V_c \langle b^+(\mathbf{p} + \mathbf{q} + \mathbf{w})a(\mathbf{p} + \mathbf{q}) \rangle \langle Tb(\mathbf{p} + \mathbf{w}, t)a^+(\mathbf{p}, t') \rangle \quad (5.19)$$

We directly observe by comparison with (5.16) and (5.4) that Wick's theorem makes naturally appear in (5.19) the electron-hole pair operator and the anomalous Green's function. The equation of motion then becomes

$$\begin{aligned} [i\frac{\partial}{\partial t} - \epsilon_a(\mathbf{p})]G_a(\mathbf{p}, t, t') &= \delta(t - t') + i \sum_{\mathbf{q}, \mathbf{w}} V_c \varphi_0^*(\mathbf{p} + \mathbf{q}, \mathbf{w}) \xi_0^*(\mathbf{w}) iF(\mathbf{p}, \mathbf{w}, t, t') \\ &= \delta(t - t') - \sum_{\mathbf{w}} \Delta(\mathbf{p}, \mathbf{w}) F(\mathbf{p}, \mathbf{w}, t, t') \end{aligned} \quad (5.20)$$

where the order parameter Δ is defined by

$$\begin{aligned} \Delta(\mathbf{p}, \mathbf{w}) &= \sum_{\mathbf{q}} V_c \langle b^+(\mathbf{p} + \mathbf{q} + \mathbf{w})a(\mathbf{p} + \mathbf{q}) \rangle \\ &= \sum_{\mathbf{q}} V_c \varphi_0^*(\mathbf{p} + \mathbf{q}, \mathbf{w}) \xi_0^*(\mathbf{w}) \end{aligned} \quad (5.21)$$

In our aim to evaluate the Green's function of the valence band we still have to determine the anomalous Green's function $F(\mathbf{p}, \mathbf{w}, t, t')$. We proceed as above with the equation of motion:

$$[i\frac{\partial}{\partial t} - \epsilon_b(\mathbf{p} + \mathbf{w})]F(\mathbf{p}, \mathbf{w}, t, t') = (-i) \sum_{\mathbf{k}, \mathbf{q}} V_c(\mathbf{q}) \langle Tb(\mathbf{p} + \mathbf{w} + \mathbf{q}, t)a^+(\mathbf{k} + \mathbf{q}, t)a(\mathbf{k}, t)a^+(\mathbf{p}, t') \rangle \quad (5.22)$$

Using Wick's theorem to evaluate the time ordered bracket and introducing the order parameter leads to the following equation of motion:

$$[i\frac{\partial}{\partial t} - \epsilon_b(\mathbf{p} + \mathbf{w})]F(\mathbf{p}, \mathbf{w}, t, t') = -\Delta^*(\mathbf{p}, \mathbf{w})G_a(\mathbf{p}, t - t') \quad (5.23)$$

Solving the differential equations (5.20) and (5.23) is achieved by time Fourier transformation which leads respectively to:

$$(z - \epsilon_a(\mathbf{p}))G_a(\mathbf{p}, z) = 1 - \sum_{\mathbf{w}} \Delta(\mathbf{p}, \mathbf{w})F(\mathbf{p}, \mathbf{w}, z) \quad (5.24)$$

and

$$(z - \epsilon_b(\mathbf{p} + \mathbf{w}))F(\mathbf{p}, \mathbf{w}, z) = -\Delta^*(\mathbf{p}, \mathbf{w})G_a(\mathbf{p}, z) \quad (5.25)$$

If one considers a single \mathbf{w} , one finally obtains for the Green's function of the valence band:

$$G_a(\mathbf{p}, z) = \frac{1}{z - \epsilon_a(\mathbf{p}) - \frac{|\Delta(\mathbf{p}, \mathbf{w})|^2}{z - \epsilon_b(\mathbf{p} + \mathbf{w})}} \quad (5.26)$$

This result has the same form as the one of the BCS theory of superconductivity with the self energy given by $\sigma_a(\mathbf{p}, z) = \frac{|\Delta(\mathbf{p}, \mathbf{w})|^2}{z - \epsilon_b(\mathbf{p} + \mathbf{w})}$. The spectral function for the valence band can be derived from (5.26) with the usual formula

$$A_a(\mathbf{p}, z) = \frac{1}{\pi} |ImG_a(\mathbf{p}, z)| = u_a^2(\mathbf{p})\delta(z - z_+(\mathbf{p})) + v_a^2\delta(z - z_-(\mathbf{p})) \quad (5.27)$$

where the poles $z_{\pm}(\mathbf{p})$ are roots of $(z - \epsilon_a(\mathbf{p}))(z - \epsilon_b(\mathbf{p} + \mathbf{w})) - |\Delta(\mathbf{p}, \mathbf{w})|^2 = 0$ and take the following values

$$z_{\pm}(\mathbf{p}) = \frac{1}{2}[\epsilon_a(\mathbf{p}) + \epsilon_b(\mathbf{p} + \mathbf{w}) \pm \sqrt{(\epsilon_a(\mathbf{p}) - \epsilon_b(\mathbf{p} + \mathbf{w}))^2 + 4|\Delta(\mathbf{p}, \mathbf{w})|^2}] \quad (5.28)$$

$u_a^2(\mathbf{p})$ and $v_a^2(\mathbf{p})$ represent the spectral weight distribution and it can be easily shown that they take the following form:

$$u_a^2(\mathbf{p}) = \frac{z_+(\mathbf{p}) - \epsilon_b(\mathbf{p} + \mathbf{w})}{z_+(\mathbf{p}) - z_-(\mathbf{p})} \quad \text{and} \quad v_a^2(\mathbf{p}) = \frac{z_-(\mathbf{p}) - \epsilon_b(\mathbf{p} + \mathbf{w})}{z_-(\mathbf{p}) - z_+(\mathbf{p})} \quad (5.29)$$

In a similar way the Green's function and spectral function of the conduction band are

$$G_b(\mathbf{k}, \mathbf{w}, z) = \frac{1}{z - \epsilon_b(\mathbf{k}) - \frac{|\Delta(\mathbf{k}, \mathbf{w})|^2}{z - \epsilon_a(\mathbf{k} - \mathbf{w})}} \quad (5.30)$$

and

$$A_b(\mathbf{k}, z) = \frac{1}{\pi} |ImG_b(\mathbf{k}, z)| = u_b^2(\mathbf{k})\delta(z - z_+(\mathbf{k})) + v_b^2\delta(z - z_-(\mathbf{k})) \quad (5.31)$$

Now the poles are located at

$$z_{\pm}(\mathbf{k}) = \frac{1}{2}[\epsilon_a(\mathbf{k} - \mathbf{w}) + \epsilon_b(\mathbf{k}) \pm \sqrt{(\epsilon_a(\mathbf{k} - \mathbf{w}) - \epsilon_b(\mathbf{k}))^2 + 4|\Delta(\mathbf{k}, \mathbf{w})|^2}] \quad (5.32)$$

and the spectral weights are

$$u_b^2(\mathbf{k}) = \frac{z_+(\mathbf{k}) - \epsilon_a(\mathbf{k} - \mathbf{w})}{z_+(\mathbf{k}) - z_-(\mathbf{k})} \quad \text{and} \quad v_b^2(\mathbf{k}) = \frac{z_-(\mathbf{k}) - \epsilon_a(\mathbf{k} - \mathbf{w})}{z_-(\mathbf{k}) - z_+(\mathbf{k})}. \quad (5.33)$$

We can easily verify that for a zero order parameter, our results correspond to the starting band structure $\epsilon_a(\mathbf{p})$ and $\epsilon_b(\mathbf{p})$. On Fig. 5.3 the resulting band structure for a condensate of excitons is drawn. Compared to Fig. 5.2, backfolded valence and conduction bands appear simultaneously with a hump in the conduction band. Moreover, the spectral weight is not uniformly distributed. There is a slight decrease of intensity at the top of the valence band as well as on the hump of the conduction band, as the weight on the backfolded bands has an opposite distribution than the one on the original bands.

5.2.4 Fluctuating excitons

We see above how the electronic structure of a simple two band system is influenced when a Bose condensate of excitons is formed. However at higher temperature we can already expect existence of fluctuating excitons with finite lifetime, that can also interact with electrons of the material. The aim here is to determine which kind of signatures these fluctuating excitons will leave on our ARPES spectra. As discussed in chapter 2, since the contributions of interactions are all contained in the self-energy term, we concentrate our efforts on searching an expression for such a term.

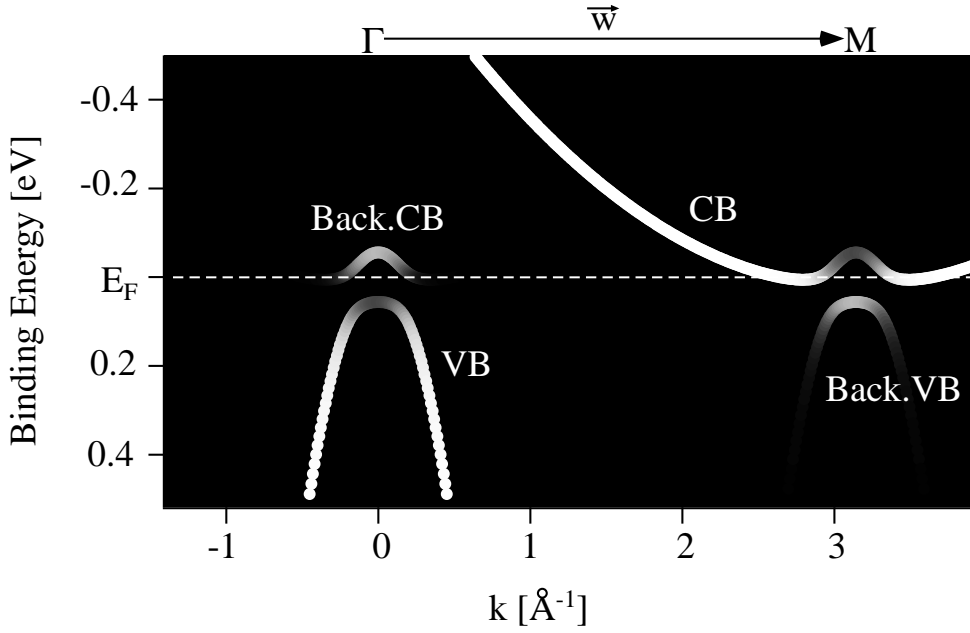


Figure 5.3: Band structure predicted by the 1D two bands condensate model for a gap value of 50 meV and a constant order parameter $\Delta = 0.05$.

To take into account the effects of interaction with a bath of fluctuating excitons, we need to solve the equation of motion (5.17) at finite temperature. The extension to finite temperature was originated by Matsubara. The reader will find a good introduction to this formalism, which implies working with imaginary times, in chapter 3 of ref. [21].

Basically, in the Matsubara formalism the bracket $\langle \rangle$ means that a thermodynamic average is made over all possible configurations of the system and therefore the interacting term on the right of (5.17) becomes after some manipulations :

$$-i \sum_{\mathbf{k}, \mathbf{q}, \mathbf{w}} V_c(\mathbf{q}) \langle T S \hat{a}(\mathbf{p} + \mathbf{q}, t) \hat{b}^+(\mathbf{k} + \mathbf{w}, t) \hat{b}(\mathbf{k} + \mathbf{w} - \mathbf{q}, t) \hat{a}^+(\mathbf{p}, t') \rangle. \quad (5.34)$$

where $\langle \rangle$ indicates that the thermodynamic average is done over states of the unperturbed Hamiltonian, $S = T e^{-i \int_0^{-i\beta} d\tau W(\tau)}$ is the so-called S-matrix which contains all the effects of interactions, and the hats on the operators indicate the use of the interaction representation meaning that the time dependence of these operators is governed only by the unperturbed Hamiltonian. T is now an imaginary time ordering operator. (5.34) is evaluated by expanding the S-matrix to first order:

$$S \simeq T [1 - i \int_0^{-i\beta} d\tau W(\tau)]. \quad (5.35)$$

The first term equal to unity does not give any contribution since it leads to the condensate expression of the previous section which is zero in the present case. Thus, after substitution of W by its correct expression, the interaction term of the equation of motion becomes:

$$- \sum_{\mathbf{k}, \mathbf{k}', \mathbf{k}'', \mathbf{q}, \mathbf{q}', \mathbf{w}} V_c(\mathbf{q}) V_c(\mathbf{q}') \int_0^{-i\beta} d\tau \langle T \hat{a}(\mathbf{p} + \mathbf{q}, t) \hat{b}^+(\mathbf{k} + \mathbf{w}, t) \hat{b}(\mathbf{k} + \mathbf{w} - \mathbf{q}, t) \hat{a}^+(\mathbf{k}', \tau) \hat{a}(\mathbf{k}' - \mathbf{q}', \tau) \hat{b}^+(\mathbf{k}'' + \mathbf{w}, \tau) \hat{b}(\mathbf{k}'' + \mathbf{w} + \mathbf{q}', \tau) \hat{a}^+(\mathbf{p}, t') \rangle. \quad (5.36)$$

As before, we factorize the operators corresponding to particles which are only observers of excitons and we keep together operators which create excitons:

$$\langle Tb(\mathbf{k} + \mathbf{w} - \mathbf{q}, t)b^+(\mathbf{k}'' + \mathbf{w}, \tau) \rangle_0 = iG_b^0(\mathbf{k} - \mathbf{q} + \mathbf{w}, t - \tau)\delta(\mathbf{k} - \mathbf{q}, \mathbf{k}'') \quad (5.37)$$

$$- \langle Ta(\mathbf{k}' - \mathbf{q}', \tau)a^+(\mathbf{p}, t') \rangle_0 = -iG_a^0(\mathbf{p}, \tau - t')\delta(\mathbf{k}' - \mathbf{q}', \mathbf{p}) \quad (5.38)$$

$$\begin{aligned} & \langle Tb^+(\mathbf{k} + \mathbf{w}, t)a(\mathbf{p} + \mathbf{q}, t)a^+(\mathbf{k}', \tau)b(\mathbf{k}'' + \mathbf{w} + \mathbf{q}', \tau) \rangle_0 \\ &= - \langle Tb^+(\mathbf{p} + \mathbf{q} + \mathbf{Q} + \mathbf{w}, t)a(\mathbf{p} + \mathbf{q}, t)a^+(\mathbf{p} + \mathbf{q}', \tau)b(\mathbf{p} + \mathbf{q}' + \mathbf{Q} + \mathbf{w}, \tau) \rangle_0 \\ &= \langle \sum_{\lambda, \lambda'} \varphi_\lambda^*(\mathbf{p} + \mathbf{q} + \beta\mathbf{Q}, \mathbf{w})A_\lambda^+(\mathbf{Q}, \mathbf{w}, t)\varphi_{\lambda'}(\mathbf{p} + \mathbf{q}' + \beta\mathbf{Q}, \mathbf{w})A_{\lambda'}^+(\mathbf{Q}, \mathbf{w}, t) \rangle_0 \end{aligned} \quad (5.39)$$

where for the last bracket we do the substitutions imposed by the delta function, i.e. $\mathbf{k}'' = \mathbf{k} - \mathbf{q}$ and $\mathbf{k}' = \mathbf{p} + \mathbf{q}$, and moreover we settle $\mathbf{k} = \mathbf{p} + \mathbf{q} + \mathbf{Q}$ to find correspondance with (5.9) which allows to express these last two brackets as a function of the exciton operator A^+ . We note that the first two brackets make appear the unperturbed one electron Green's function due to the thermal average over unperturbed configurations. By introducing these expressions in (5.36), we find:

$$\begin{aligned} & \sum_{\mathbf{Q}, \lambda, \lambda', \mathbf{w}} \int_0^{-i\beta} d\tau G_b^0(\mathbf{p} + \mathbf{Q} + \mathbf{w}, t - \tau) \langle TA_\lambda^+(\mathbf{Q}, \mathbf{w}, t)A_{\lambda'}(\mathbf{Q}, \mathbf{w}, t) \rangle_0 G_a^0(\mathbf{p}, \tau - t') \\ & \quad \times \sum_{\mathbf{q}, \mathbf{q}'} V_c(\mathbf{q})V_c(\mathbf{q}')\varphi_\lambda^*(\mathbf{p} + \mathbf{q} + \beta\mathbf{Q}, \mathbf{w})\varphi_{\lambda'}(\mathbf{p} + \mathbf{q}' + \beta\mathbf{Q}, \mathbf{w}) \end{aligned} \quad (5.40)$$

The bracket can be expressed as the excitonic Green's function and is equal to $-i\delta_{\lambda, \lambda'}G_\lambda^{ex}(\mathbf{Q}, \tau - t)$. To be consistent this last Green's function would be the unperturbed one, but since exciton without interactions does not make sense, we artificially include interaction. Moreover by comparison with (5.21) we can substitute the double summation over \mathbf{q} and \mathbf{q}' by an expression with the order parameter Δ . Therefore, the contribution due to the interaction with the field of fluctuating excitons in the equation of motion is given by:

$$-i \int_0^{-i\beta} d\tau \sum_{\mathbf{Q}, \lambda, \mathbf{w}} G_b^0(\mathbf{p} + \mathbf{Q} + \mathbf{w}, t - \tau) |\Delta(\mathbf{p} + \beta\mathbf{Q})|^2 G_\lambda^{ex}(\mathbf{Q}, \tau - t)G_a^0(\mathbf{p}, \tau - t') \quad (5.41)$$

which leads to the following self-energy for the valence electrons:

$$\Sigma_a(\mathbf{p}, t) \sim - \sum_{\mathbf{Q}, \lambda, \mathbf{w}} |\Delta(\mathbf{p} + \beta\mathbf{Q})|^2 G_b^0(\mathbf{p} + \mathbf{Q} + \mathbf{w}, t - \tau)G_\lambda^{ex}(\mathbf{Q}, \tau - t) \quad (5.42)$$

In an analogous way we can derive the self-energy for the electrons of the conduction band and we obtain:

$$\Sigma_b(\mathbf{k}, t) \sim \sum_{\mathbf{Q}, \lambda} |\Delta(\mathbf{p} - \alpha\mathbf{Q})|^2 G_a^0(\mathbf{k} - \mathbf{Q}, t - \tau)G_\lambda^{ex}(\mathbf{Q}, t - \tau) \quad (5.43)$$

The time Fourier transform leads to *:

*The Fourier transform is evaluated by using the properties of fermions and bosons Green's functions which can be expanded as $f(\tau) = \frac{1}{-i\beta} \sum_n e^{-iz_n\tau} f(z_n)$ with $z_n = \frac{2n\pi}{\beta}$ for bosons and $z_n = \frac{(2n+1)\pi}{\beta}$ for fermions

$$\begin{aligned}
 \Sigma_a(\mathbf{p}, z_\mu) &\sim -i \int_0^{-i\beta} dt e^{iz_\mu t} \Sigma_a(\mathbf{p}, t) \\
 &= -i \sum_{\mathbf{Q}, \lambda, \mathbf{w}} |\Delta(\mathbf{p} + \beta\mathbf{Q})|^2 \int_0^{-i\beta} dt e^{iz_\mu t} \sum_{\alpha, \gamma} \frac{e^{i(z_\alpha - z_\gamma)t}}{(-i\beta)^2} G_b^0(\mathbf{p} + \mathbf{Q} + \mathbf{w}, z_\gamma) G_\lambda^{ex}(\mathbf{Q}, z_\alpha) \\
 &= -i \sum_{\mathbf{Q}, \lambda, \mathbf{w}} |\Delta(\mathbf{p} + \beta\mathbf{Q})|^2 \sum_{\alpha} \frac{1}{-i\beta} G_b^0(\mathbf{p} + \mathbf{Q} + \mathbf{w}, z_\mu + z_\alpha) G_\lambda^{ex}(\mathbf{Q}, z_\alpha) \quad (5.44)
 \end{aligned}$$

and

$$\Sigma_b(\mathbf{k}, z_\nu) \sim i \sum_{\mathbf{Q}, \lambda} |\Delta(\mathbf{k} - \alpha\mathbf{Q})|^2 \sum_{\alpha} \frac{1}{-i\beta} G_a^0(\mathbf{k} - \mathbf{Q}, z_\nu - z_\alpha) G_\lambda^{ex}(\mathbf{Q}, z_\alpha) \quad (5.45)$$

for the valence and conduction electrons, respectively. In the aim to evaluate the frequency sum, we first express each Green's function as a frequency integral over its respective spectral function:

$$\Sigma_a(\mathbf{p}, z_\mu) \sim -i \sum_{\mathbf{Q}, \lambda, \mathbf{w}} |\Delta(\mathbf{p} + \beta\mathbf{Q})|^2 \frac{1}{-i\beta} \sum_{\alpha} \int \frac{d\omega}{2\pi} \int \frac{d\omega'}{2\pi} \frac{A_b^0(\mathbf{p} + \mathbf{Q} + \mathbf{w}, \omega')}{z_\mu + z_\alpha - \omega'} \frac{E_\lambda^{ex}(\mathbf{Q}, \omega)}{z_\alpha - \omega}. \quad (5.46)$$

Then we evaluate the sum, which leads to[†]:

$$\begin{aligned}
 \Sigma_a(\mathbf{p}, z_\mu) &\sim i \sum_{\mathbf{Q}, \lambda, \mathbf{w}} |\Delta(\mathbf{p} + \beta\mathbf{Q})|^2 \int \frac{d\omega}{2\pi} \int \frac{d\omega'}{2\pi} A_b^0(\mathbf{p} + \mathbf{Q} + \mathbf{w}, \omega') E_\lambda^{ex}(\mathbf{Q}, \omega) \\
 &\quad \times \frac{N_B(\omega) + N_F(\omega')}{z_\mu + \omega - \omega'} \quad (5.47)
 \end{aligned}$$

Similarly for the self-energy of the conduction electrons:

$$\begin{aligned}
 \Sigma_b(\mathbf{k}, z_\nu) &\sim i \sum_{\mathbf{Q}, \lambda} |\Delta(\mathbf{k} - \alpha\mathbf{Q})|^2 \int \frac{d\omega}{2\pi} \int \frac{d\omega'}{2\pi} A_a^0(\mathbf{k} - \mathbf{Q}, \omega') E_\lambda^{ex}(\mathbf{Q}, \omega) \\
 &\quad \times \frac{N_B(\omega) + 1 - N_F(\omega')}{z_\nu - \omega - \omega'} \quad (5.48)
 \end{aligned}$$

To obtain a first evaluation of these self-energies, one proceeds to a series of approximations: (i) As for small ω the Bose-Einstein distribution diverges, we consider only the bosonic contribution

[†]The frequency sum is evaluated by a contour integration thanks the following identity: $\frac{1}{-i\beta} \sum_{\alpha} f(z_\alpha) = \oint dz N_B(z) f(z) = -i \sum_l R_l$ where R_l is a residue of $N_B(z) f(z)$ at pole z_l of $f(z)$ and $N_B(z)$ is the Bose-Einstein distribution which generates poles at $\frac{i2n\pi}{\beta}$ for all integers n . In our example $f(z_\alpha) = \frac{1}{(z_\alpha - \omega)(z_\mu + z_\alpha - \omega')}$ has a pole originating from the exciton Green's function at $z_\alpha = \omega$ and one originating from the electron Green's function at $z_\alpha = \omega' - z_\mu$. The residues for these poles are $-i \frac{N_B(\omega)}{z_\mu + \omega - \omega'}$ and $\frac{N_B(\omega' - z_\mu)}{z_\mu + \omega - \omega'}$, respectively. Moreover $N_B(\omega' - z_\mu)$ with z_μ fermionic is equal to $-N_F(\omega')$, N_F being the Fermi distribution

$N_B(\omega)$ and we neglect the fermionic part ($1-N_F(\omega')$) in the integration. (ii) We admit the following delta function for the exciton spectrum:

$$E_\lambda^{ex}(\mathbf{Q}, \omega) = 2\pi\delta(\omega - \frac{\mathbf{Q}^2}{2M} - \eta_\lambda) \quad (5.49)$$

with $\eta_\lambda = E_\lambda - \mu_B$ [‡]. (iii) we simplify drastically the physics concerning the excitons by assuming that they follow a Boltzman distribution instead of the Bose-Einstein one and that only the $\mathbf{Q}=0$ and $\lambda=0$ ground state is occupied. (iv) Finally, we assume an order parameter Δ independent of wave vector for small \mathbf{k} . All that leads to the following simplified self-energies for only one w:

$$\Sigma_a(\mathbf{p}, z) \sim |\Delta|^2 \frac{1}{z - \epsilon_b(\mathbf{p} + \mathbf{w}) + \eta_0} \quad (5.50)$$

$$\Sigma_b(\mathbf{k}, z) \sim |\Delta|^2 \frac{1}{z - \epsilon_a(\mathbf{k}) - \eta_0} \quad (5.51)$$

and, therefore to the Green's functions:

$$G_a(\mathbf{p}, z) = \frac{1}{z - \epsilon_a(\mathbf{p}) - \frac{|\Delta|^2}{z - (\epsilon_b(\mathbf{p} + \mathbf{w}) - \eta_0)}} \quad (5.52)$$

$$G_b(\mathbf{k}, z) = \frac{1}{z - \epsilon_b(\mathbf{k}) - \frac{|\Delta|^2}{z - (\epsilon_a(\mathbf{k} - \mathbf{w}) + \eta_0)}}. \quad (5.53)$$

These expressions for the Green's functions are very similar to the one found for the condensat ((5.26) and (5.30)), the only difference being the presence of the additional term η_0 in the denominator of the self-energy. Although these results are obtained by use of very crude approximations, we will see that they imply already interesting effects that will be discussed in the experimental section.

5.3 Experimental results and confrontation with the exciton model

The adoption of the excitonic scenario as mechanism for the occurrence of the CDW in 1T-TiSe₂ is strongly dependent on the relative position of the Se 4p and Ti 3d derived bands (Fig. 5.4). As pointed out by band structure calculations and ARPES experiments of Anderson et al. [8] three-dimensional effects have a non-negligible influence on the electronic structure of this material. Indeed as shown in Fig. 5.5 DFT band structure calculations predict a considerable dispersion of the Ti 3d band from M to L and of the Se 4p bands from A to Γ , which leads to an overlap of more than 0.5 eV between the metallic and the chalcogen derived bands. In the aim to verify these predictions, using synchrotron radiation, we have performed ARPES experiment as a function of photon energy. The obtained dispersions along Γ -A and M-L for the Se 4p and Ti 3d derived bands are superimposed to the DFT calculations in Fig. 5.5. As DFT reproduces badly the position of the Fermi level, we shift our experimental spectra by a constant energy to correct for this. A remarkable good correspondence between the experimental and calculated Se 4p derived band dispersion is found. The topmost Se 4p occupied band located at a binding energy of ~ 100 meV is only slightly dispersive (less than 30 meV) but nevertheless has a maximum at Γ as well as the two lowest more dispersive Se 4p derived bands. On the other hand, the measured position and behaviour of the Ti 3d derived band differs considerably from the DFT predictions. ARPES

[‡]Here, the exciton energy is given relatively to the chemical potential μ_B . Note that, as we consider fluctuating excitons, η_λ is always larger than zero

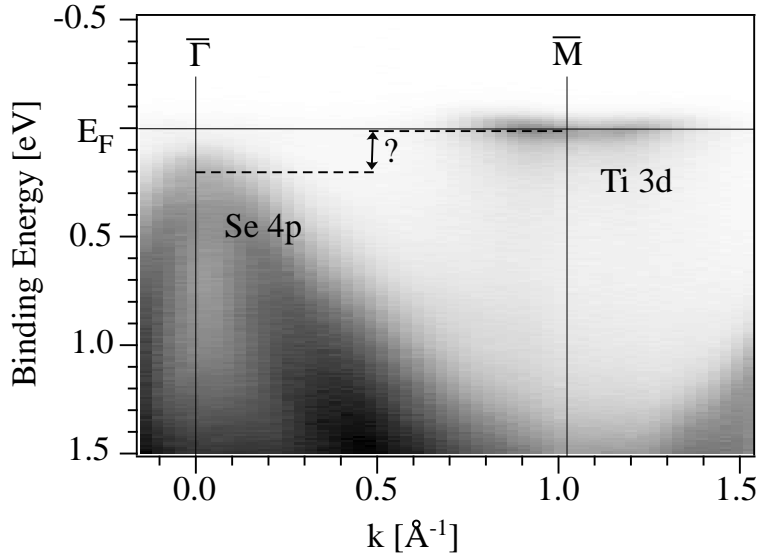


Figure 5.4: ARPES measurement along the $\bar{\Gamma} - \bar{M}$ direction, taken with 21.2 eV at room temperature. A key value for the excitonic scenario is the energy distance between the Se 4p and Ti 3d derived bands.

measures the Ti 3d band at the Fermi level and with a very small dispersion of less than 20 meV. Therefore, instead of a semimetallic character with a Se 4p and Ti 3d band overlap of ~ 500 meV predicted by DFT, we obtain experimentally a semiconducting character with an indirect gap of the order of 50 meV.

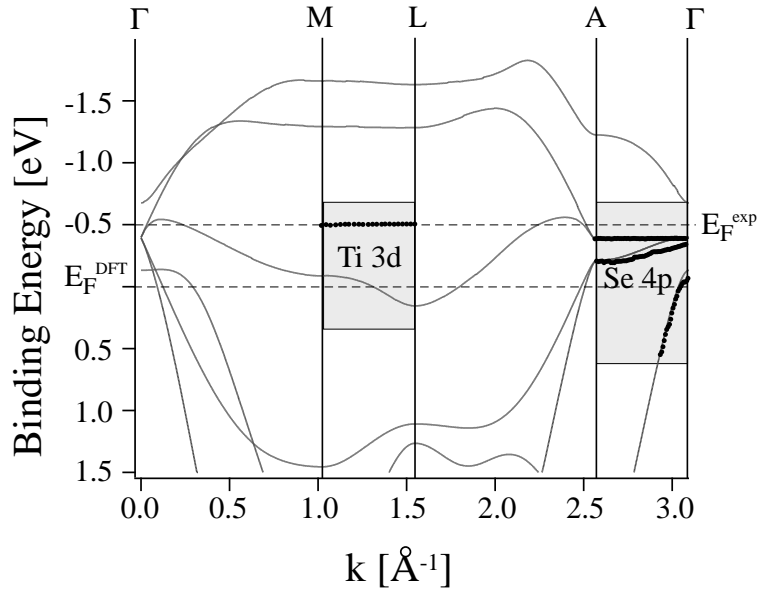


Figure 5.5: Comparison between DFT band structure calculations and band dispersion derived from ARPES measurements along the k_{\perp} directions. ARPES peak positions are the black large dots superimposed to the DFT results.

Although correlation effects can explain the discrepancies between DFT and ARPES data, the question if this small Ti 3d dispersion feature could also be an artefact of the photoemission process remains open. Nevertheless the magnitude of the indirect gap and the width of the bands, which tends to narrow the distance between states, allow to consider the possible formation of excitons.

On Fig. 5.6 a comparison between the band structure found in section 5.2.3 in case of the

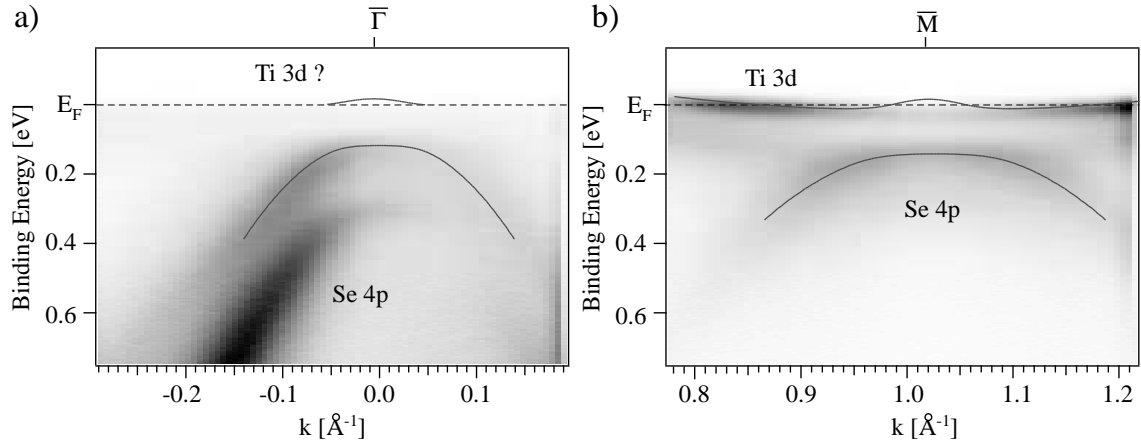


Figure 5.6: Comparison between ARPES measurements taken with 21 eV photons at 160 K in the vicinity of $\bar{\Gamma}$ (a) and \bar{M} (b), and the excitons condensate band structure. The fine lines depict the dispersion predicted by the condensate model.

condensation of excitons and the ARPES spectrum measured near $\bar{\Gamma}$ and \bar{M} at 160 K (temperature below the transition) is drawn. We observe several similarities: first, as predicted by the condensate model a Se 4p backfolded band appears at \bar{M} and this band is flattened compared to its shape at room temperature; the concentration of the spectral weight on the top of this Se 4p band is also observed. Then, for the Ti 3d band at \bar{M} , one notes the intensity reduction around \bar{M} , that we interpret as a consequence of the conduction band bending as well as of the intensity loss at this k position predicted by the condensate model. Moreover, the absence of the Ti 3d backfolded band at $\bar{\Gamma}$ can also be explained by the prediction that most of the spectral weight concentrates on the top of the hump which lies above the Fermi level.

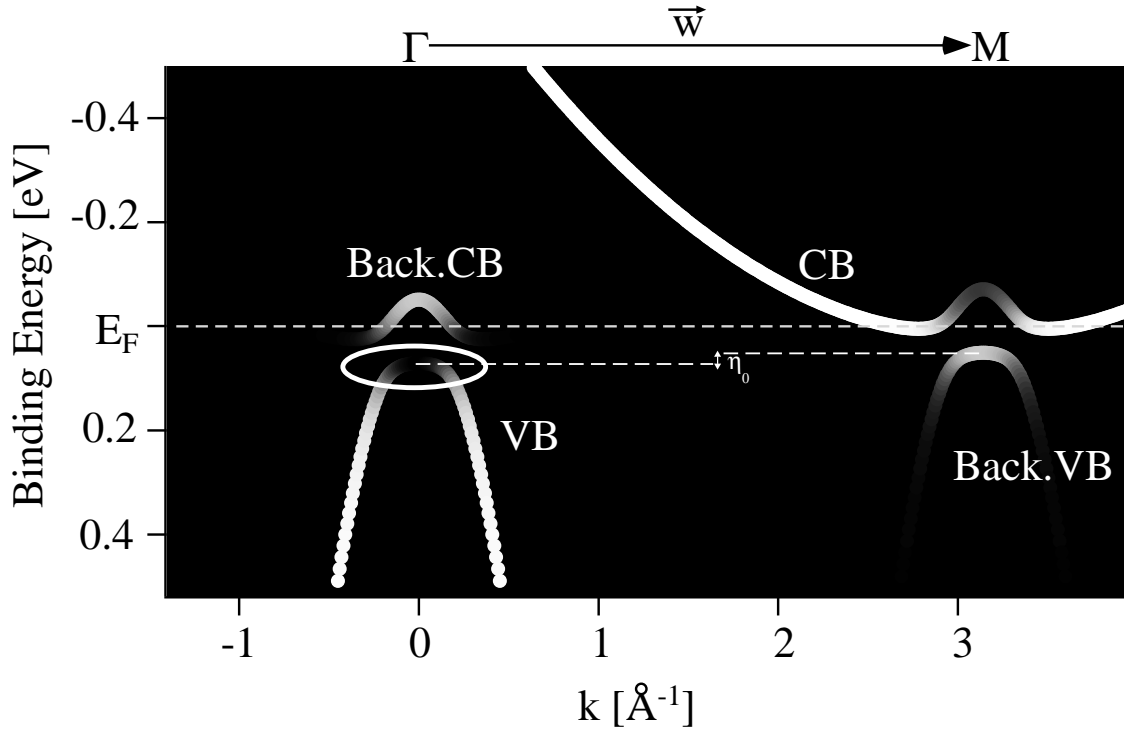


Figure 5.7: Band structure predicted for the 1D fluctuating exciton model using the simplified self-energies (5.50) and (5.51). The same parameters as in Fig. 5.3 are used and a value of 0.02 is chosen for η_0 .

Furthermore, if we include the changes induced by fluctuating excitons, we observe, according

5.4. Summary

to calculations of section 5.2.4, the following interesting modifications represented in Fig. 5.7. First, the backfolded bands are shifted by η_0 compared to the position of the original conduction and valence bands. Second, the spectral weight at the top of the original valence band is considerably reduced. These two features are also present in our ARPES data. Fig. 5.8 shows a comparison between EDCs measured at $\bar{\Gamma}$ (in Black) and at \bar{M} (in gray), where, indeed, we observe a small difference between the position of the topmost original Se 4p band and the backfolded one. The intensity loss at the top of the original Se 4p band is also observed in some series of measurements. Therefore, it is still unclear if we can attribute this to the fluctuation of excitons or to others effects such matrix element effects or dependance on the cleave.

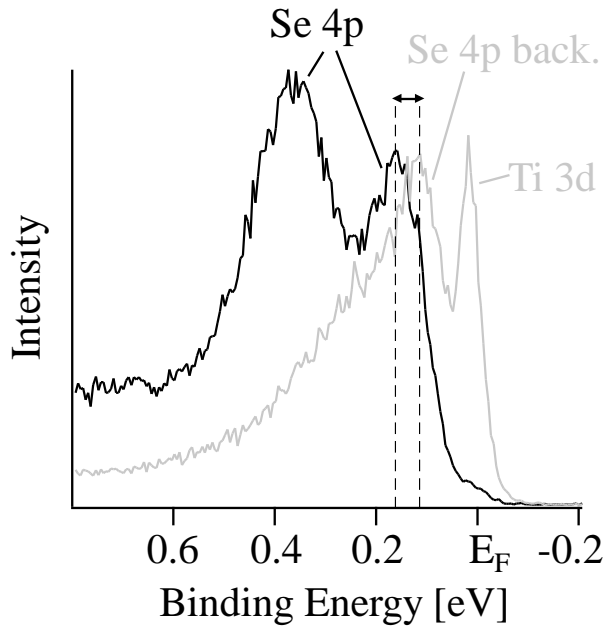


Figure 5.8: EDCs measured at $\bar{\Gamma}$ (in black) and \bar{M} (in gray) with photon energy of 21.2 eV at 160 K.

From these comparisons between the theoretical excitonic model and our ARPES data, we can claim that there is some traces tending to support this exciton scenario as a cause for the occurrence of CDW in $1T$ -TiSe₂. However all these features are not sufficient to exclude other models. More information could be gained from the understanding of additional features present at low temperature near the Ti 3d band at \bar{M} and indicated by arrows in Fig. 5.9 which represents a waterfall of EDC's obtained from vertical cuts of the carpets of Fig. 5.6 (b). This additional shoulder has an interesting temperature dependent behaviour opposed to the behaviour of the intensity of the backfolded Se 4p derived band at \bar{M} , since the shoulder intensity decreases from room temperature to low temperature well below the transition. There is a strong hope that this behaviour could be explained thanks to the self-energy derived from the fluctuating excitons model. However for a fine analysis, we need to evaluate more exactly the expressions (5.47) and (5.48) by considering, for exemple, a correct distribution of the occupied exciton states as well as including finite life time for excitons. This refinement will lead to a more complicated function than the delta function used for the exciton spectral function.

5.4 Summary

Using high resolution ARPES as a function of photon energy, we are able to confirm the 3D character of some electronic states, but, in contrast to previous works [8], our results reveal an

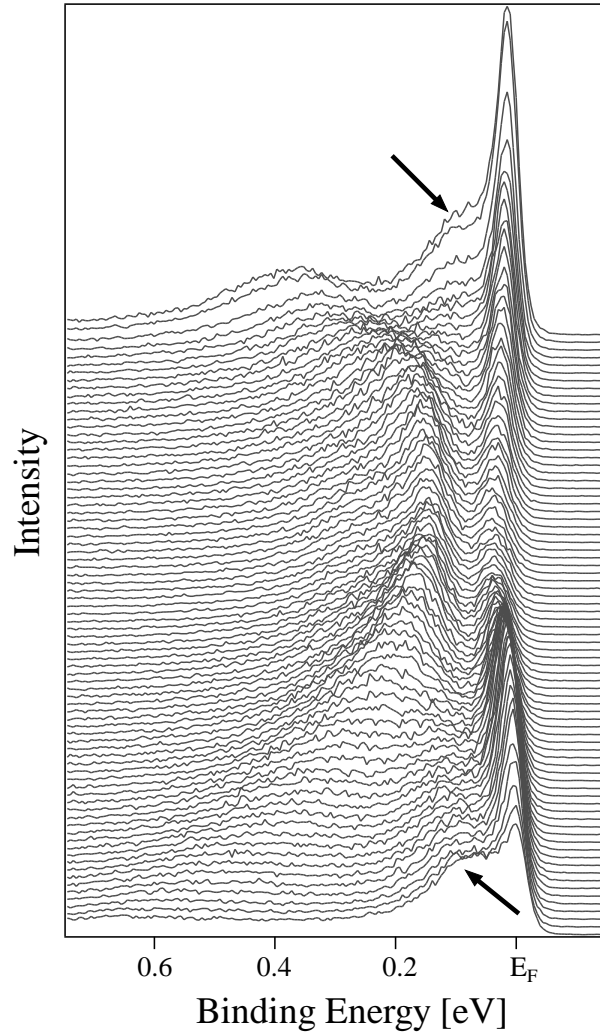


Figure 5.9: EDCs extracted from vertical cuts of Fig. 5.6. The arrows point to unusual spectral features.

indirect gap of ~ 50 meV. Among the proposed scenarios to explain the CDW phase in $1T$ - TiSe_2 , we focus our attention on the exciton mechanism deriving model band structure for two cases: The exciton condensate and the fluctuating excitons. At this stage of comparison between these models and photoemission data, our ARPES results are consistent with the scenario of an excitonic phase. However further refinements of the fluctuating excitons model band structure are needed to explain additional spectral features observed in data at low temperature as well as to understand the temperature dependent behaviour of excitons. A final remark is to note the importance to characterize each cleave used for ARPES measurements. Indeed, we note a dependence of our results as function of the cleave. An explanation can arise from the presence of Ti excess which strongly influences the relative energy positions of the valence and conduction bands. STM measurements (not shown) demonstrating local Ti excess tend to support this view.

References for chapter 5

- [1] F. J. DiSalvo, D. E. Moncton and J. V. Waszczak, *Phys. Rev. B* **14**, 4321 (1976).
- [2] R. M. White and G. Lucowsky, *Nuovo Cimento* **38 B**, 280 (1977).
- [3] H. P. Hughes, *J. Phys. C* **10**, L319 (1977).
- [4] M.-H. Whangbo and E. Canadell, *J. Am. Chem. Soc* **114**, 9587 (1992).
- [5] J. A. Wilson, *Solid State Commun.* **22**, 551 (1977).
- [6] W. Kohn, *Phys. Rev. Lett* **19**, 439 (1967).
- [7] K. Motizuki, N. Suzuki, Y. Yoshida and Y. Takaoka, *Solid State Commun.* **40**, 995 (1981).
- [8] O. Anderson, R. Manzke and M. Skibowski, *Phys. Rev. Lett* **55**, 2188 (1985).
- [9] Th. Pillo, J. Hayoz, H. Berger, R. Fasel, L. Schlapbach and P. Aebi, *Phys. Rev. B* **61**, 16213 (2000).
- [10] T. E. Kidd, T. Miller, M. Y. Chou and T.-C. Chiang, *Phys. Rev. Lett* **88**, 226402 (2002).
- [11] K. Rossnagel, L. Kipp and M. Skibowski, *Phys. Rev. B* **65**, 235101 (2002).
- [12] N. F. Mott, *Phil. Mag.* **6**, 287 (1961).
- [13] R. S. Knox, *Solid State Phys. Suppl.* **5**, 100 (1963).
- [14] J. desCloizeaux, *J. Phys. Chem. Solids* **26**, 259 (1965).
- [15] L. V. Keldysh and Y. V. Kopaev, *Soviet Phys. Solid State* **6**, 2219 (1965).
- [16] J. Zittartz, *Phys. Rev.* **162**, 752 (1967).
- [17] J. Zittartz, *Phys. Rev.* **164**, 575 (1967).
- [18] D. Jérôme, T. M. Rice and W. Kohn, *Phys. Rev.* **158**, 462 (1967).
- [19] B. I. Halperin and T. M. Rice, *Rev. Mod. Phys.* **40**, 755 (1968).
- [20] V. S. Babichenko and M. N. Kiselev, *J. of the Moscow Phys. Soc.* **2**, 311 (1992).
- [21] G. D. Mahan, *Many-Particle Physics*(Plenum Press, New York, 1981)

Chapter 6

Spin-orbit coupling in $1T$ -TaS₂ and $1T$ -TaSe₂, a group theory study

6.1 Introduction

This chapter is devoted to the determination of the dispersion, along the Γ -A high symmetry direction, of the highest occupied chalcogen level of the two isostructural compounds $1T$ -TaS₂ and $1T$ -TaSe₂. This determination of the \mathbf{k}_{\perp} dispersion of the chalcogen p-derived bands represents a nice application of synchrotron radiation, which offers the unique advantage of the choice of the incident photon energy over a wide range.

Despite the surface sensitivity of the photoemission process the experimental band structure we have found is in good agreement with the one predicted by density functional theory (DFT) for the bulk indicating that only a weak perturbation is induced by the surface for these chalcogen states. Although it is not necessary to justify the power of DFT band calculations, this method can appear as a black box and therefore we have applied group theory tools in parallel in order to get a better understanding of the band behaviour along the various \mathbf{k} -directions. Indeed group theory provides methods for obtaining qualitative information about degeneracies of electron energy levels only from symmetry considerations. This triple combination of ARPES, DFT and group theory tools has allowed identification of a spin-orbit splitting of the chalcogen valence bands. This is detailed in the following section which consists in an article published in the Journal of Physics:Condensed Matter.

6.2 Spin-orbit splitting in the valence bands of 1T-TaS₂ and 1T-TaSe₂

F. Clerc,¹ M. Bovet,¹ H. Berger,² L. Despont,¹ C. Koitzsch,¹ O. Gallus,¹ L. Patthey,³ M. Shi,³ J. Krempasky,³ M. G. Garnier¹ and P. Aebi¹

¹ *Institut de Physique, Université de Neuchâtel, CH-2000 Neuchâtel, Switzerland*

² *Institut de Physique Appliquée, EPFL, CH-1015 Lausanne, Switzerland*

³ *Swiss Light Source, Paul Scherrer Institut CH-5232 Villigen*

Published in J. Phys. C **16**, 3271-3278 (2004)

We perform angle-resolved photoemission spectroscopy on 1T-TaS₂ and 1T-TaSe₂ using synchrotron radiation. We observe a characteristic splitting of the chalcogen p-derived valence bands along high symmetry directions. Density functional theory calculation and group theory strongly suggest that this splitting is due to spin-orbit interaction along one direction, and to symmetry along the other direction. We note that, according to the Kramers degeneracy, the spin-orbit interaction leaves every state doubly degenerate. Furthermore, this study allows to identify a mixing between bands with Ta 5d and Se 4p character possibly relevant for the different temperature behaviours of the two compounds.

6.2.1 Introduction

Spin-orbit (SO) interaction is well known to be responsible for splitting of degenerate electron energy levels in atoms, molecules and solids. It has played in the past an important role in describing the band structure of semiconductors [1, 2] and more recently in explaining various splittings of surface states [3–7]. Its physical origin is relativistic and can be explained by the interaction of the magnetic momentum of the electron (spin) with the magnetic field viewed by this electron because of its movement in the electrostatic field of the proton. This gives an additional term to the Schrödinger equation which takes the form $H_{SO} = (\hbar/4m^2c^2)(\nabla V \times \mathbf{p}) \cdot \sigma$, where V is the external potential, \mathbf{p} is the momentum and σ is the Pauli spin operator. It can also be written in the more friendly form $H_{SO} \sim \mathbf{L} \cdot \mathbf{S}$ where \mathbf{L} and \mathbf{S} are the orbital and spin angular momenta, respectively [8].

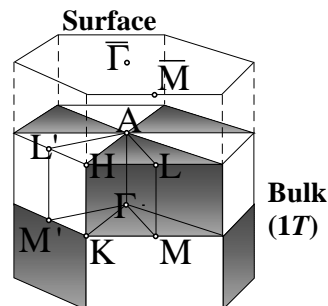


Figure 6.1: Surface and bulk Brillouin zones of the 1T structure.

Here we report high resolution angle-resolved photoemission (ARPES) measurements performed on 1T-TaS₂ and 1T-TaSe₂ at room temperature. ARPES is a powerful tool for studying the energy and momentum distribution of electrons. The technical progress made constantly to

improve the resolution of the measurements continues to refine the information, allowing a better understanding of the physics behind materials. 1T-TaS₂ and 1T-TaSe₂ have attracted much attention because of their quasi-two dimensionality and the presence of charge density waves (CDW) [9]. The comparison between these two compounds has also been largely investigated because despite their similar crystal structure and CDW symmetry they exhibit different physical properties [10–12]. Indeed, 1T-TaS₂ shows two successive first order transitions, from incommensurate CDW (ICCDW) to nearly commensurate CDW (NCCDW) at about 350K and from NCCDW to commensurate CDW (CCDW) at about 180K. In particular, it appears that this latter transition is closely related to a Mott localization within the Ta 5d band [13]. On the other hand 1T-TaSe₂ undergoes an ICCDW to CCDW transition at about 430K but does not exhibit a bulk metal-insulator transition at low temperature. In this article we focus our discussion on the chalcogen (S,Se) p-derived valence bands where a characteristic double peak is visible in the ARPES spectra. To explain this splitting we compare self consistent full potential linearized augmented plane wave (FLAPW) calculations performed with and without considering spin-orbit coupling (SOC). The calculations strongly suggest that SOC is at the origin of the splitting but only in the centre of the Brillouin zone (BZ) (Γ), and along Γ -A (see Fig. 6.1). We complete our investigation with group theory. Group theory provides methods for obtaining qualitative information about degeneracies of electron energy levels and crystal wave functions only from symmetry considerations [14, 15]. This study confirms and allows a better understanding of the results from FLAPW calculations.

6.2.2 Experiment and calculation

Photoemission measurements were carried out at room temperature using a high resolution angle-resolved photoemission spectrometer (SES-2002) at the SIS beamline X09LA of the Swiss Light Source. The energy and angular resolutions were below 10meV and $\pm 0.3^\circ$, respectively. Pure 1T-TaS₂ and 1T-TaSe₂ samples were prepared by vapour transport [16, 17] and cleaved *in situ* at pressures in the lower 10^{-10} mbar region. The quality and the orientation of the crystal structure were checked by low energy electron diffraction (LEED). The electronic structure calculations are made using the WIEN package [18] implementing the FLAPW method within the framework of density functional theory (DFT). The generalized gradient approximation was used for the exchange-correlation potential [19]. SOC has been included in the calculations in a second variational step as explained in [20]. For both samples the calculations are performed for the non-reconstructed (without CDW) crystallographic structure with space group $P\bar{3}m1$. The lattice parameters are $a=b=3,36\text{\AA}$, $c=5,85\text{\AA}$ and $a=b=3,48\text{\AA}$, $c=6,27\text{\AA}$ for the 1T-TaS₂ and 1T-TaSe₂, respectively.

6.2.3 Results and discussion

Fig. 6.2 (a) and (b) show carpets, (sets of energy distribution curves (EDCs) plotted in gray scale with high intensity in black) measured within the Γ ALM plane along the high symmetry direction $\bar{\Gamma} - \bar{M}$ of the hexagonal surface BZ, for 1T-TaS₂ and 1T-TaSe₂ with photon energies of 21.5 eV and 19.5 eV, respectively. In the 1T-TaS₂ the chalcogen p-derived bands are largely separated from the Ta 5d-derived bands which lie near the Fermi level in contrast to what we see for the 1T-TaSe₂ where the Se p-derived bands and the Ta 5d-derived bands are very close. It is clear from these data that both S 3p and Se 4p derived bands are split. This splitting is minimal at normal emission (0°) but still visible as can be seen on the fits of the normal emission spectra shown in Fig. 6.2 (c) and (d) (vertical cuts across the carpet). To explore the evolution of these bands along the Γ -A direction the measurements are repeated for different photon energies. The results are presented in Fig. 6.3 (a) and (b) where we show the peak positions obtained from the

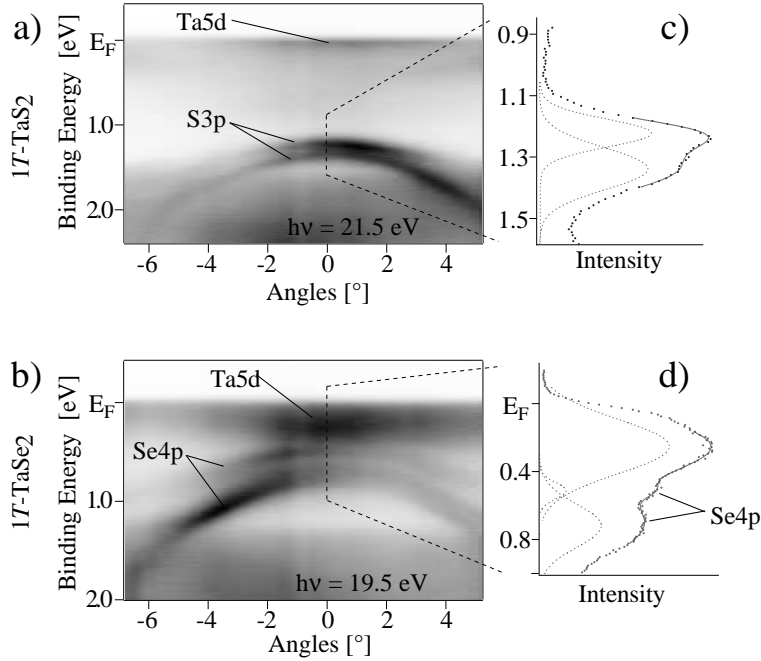


Figure 6.2: Carpets for $1T$ -TaS₂ (a) and $1T$ -TaSe₂ (b). (c) and (d) EDCs extracted at Γ from the carpet. The black lines correspond to the fit function resulting of the sum of the gaussians in dotted gray lines.

fit functions of the vertical cuts at normal emission (e.g., the white circles on the curves (Fig. 6.3 (a) and (b)) correspond to the peak positions found in Fig. 6.2 (c) and (d)). A free electron photoemission final state, as plotted in Fig. 6.3 (c) and (d), is assumed to determine the k-point within the BZ*. For the split S 3p-derived bands (Fig. 6.3 (a)) we obtain two parallel bands over the whole measured region and a constant splitting of the order of 100meV. For the Se 4p-derived bands (Fig. 6.3 (b)), the upper band position passes through a maximum whereas the lower band position increases constantly. This results in a change of the magnitude of the splitting from 200meV near A to 100meV near Γ .

Band structure calculations performed without considering the SOC are presented in Fig. 6.4 (a) and (b). In gray are represented the Ta 5d-derived bands near the Fermi level in the Γ -A region and in black at 1eV, respectively 0.2eV binding energy, the S and Se p-derived bands.

The most interesting observation is that the calculated S and Se p-derived bands are split along Γ -M but not along Γ -A, indicating that the measured splittings of the chalcogen p-bands have different physical origin and we can already say that the splitting along Γ -M is due to the crystal field and has its origin in the symmetry. However, the splitting along Γ -A observed in our measurements is reproduced by the calculations of Fig. 6.4 (c) and (d) where was accounted for the SOC. Indeed, for the two materials, as we can see in the region delimited by the gray rectangles, the calculations reproduce well the behaviour of the bands measured in Fig. 6.3 (a) and (b). The magnitude of 100 meV and 360 meV for the splitting predicted by the calculations is in good agreement for the $1T$ -TaS₂ but exaggerated in the case of $1T$ -TaSe₂. For $1T$ -TaSe₂ an additional effect of the introduction of SOC in the calculation is the crossing between the upper Se 4p-derived band and the lower Ta 5d-derived band. Therefore, the upper measured band in Fig. 6.3 (b) is the upper Se 4p-derived band from $k_{\perp}=2.64\text{\AA}^{-1}$ to $k_{\perp}=2.88\text{\AA}^{-1}$ (the crossing

*The k-point positions are calculated using the usual photoemission formula $k=\sqrt{0.263(\hbar\omega - E_B - \phi + V_0)}$ with $\hbar\omega$, E_B , ϕ and V_0 denoting the photon energy, the binding energy, the sample work function and the inner potential, respectively. We assume the following reasonable values $V_0=13$ eV, $\phi=3.5$ eV and $E_B=1.3$ eV for $1T$ -TaS₂ and $V_0=11$ eV, $\phi=3.5$ eV and $E_B=0.5$ eV for $1T$ -TaSe₂.

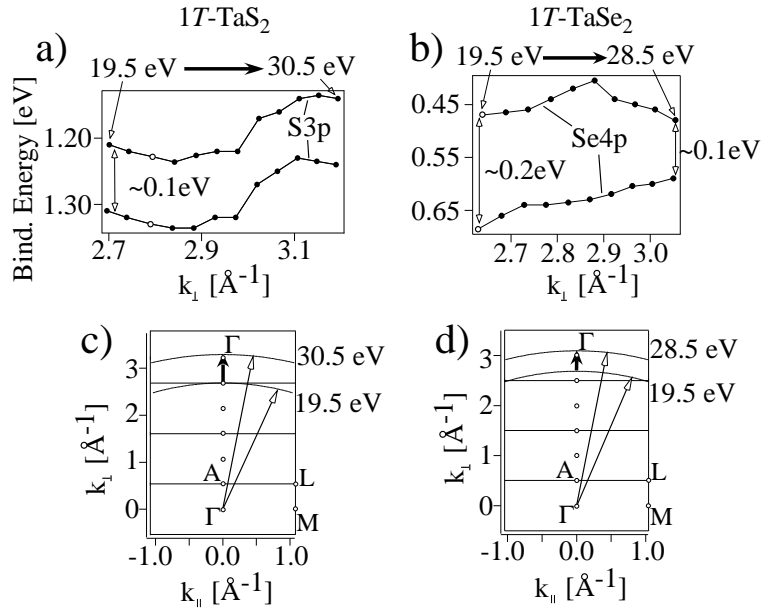


Figure 6.3: Dispersion of the split chalcogen p-derived bands along the Γ -A direction for $1T$ -TaS₂ (a) and $1T$ -TaSe₂ (b). The white circles correspond to the peak positions found from the fit in figure 6.2 c and d. The other peak positions are determined in the same manner but from EDCs taken at different photon energies. Cut in reciprocal space for the $1T$ -TaS₂ (c) and $1T$ -TaSe₂ (d) with free electron final state wave vectors for various photon energies. The black arrows show the region measured by changing the photon energy.

point) and the lower Ta 5d-derived band from $k_{\perp}=2.88\text{\AA}^{-1}$ to $k_{\perp}=3.05\text{\AA}^{-1}$. Thus we measure a splitting only up to this crossing point then the upper Se band is no more visible. This mixing or hybridization (confirmed here by the measurement) between Ta and Se derived bands has played an important role to explain differences in physical properties of the isostructural $1T$ -TaS₂ and $1T$ -TaSe₂ [11].

For quantitative information, as shown for the study of SOC in semiconductors [1], the atomic splitting is a good indicator for the magnitude of the SO splitting in valence bands. The atomic splitting of the 3p level in S is 95meV [21]. This value is of the same order than the magnitude measured for the S 3p-derived valence band, which confirms the isolated character of the S atoms in $1T$ -TaS₂. The splitting of the 4p level in Se is 418meV [21], approximately twice larger than the measured SO splitting. This reduction of the splitting in the Se 4p valence band may be a consequence of the mixing with the Ta 5d bands, where the electrons do not only feel the Se nuclei but are also influenced by the Ta nuclei. A similar anomaly in SO splitting has already been seen in semiconductors [22].

Therefore, the comparison between band structure calculation and ARPES measurements immediately suggests that the splitting along Γ -M is the result of symmetry whereas the SO interaction causes the splitting along Γ -A. The major difference between the two compounds lies in the interaction of the chalcogen atoms with the Ta. Whereas we can neglect this interaction for $1T$ -TaS₂, there is a strong mixing between Ta 5d and Se 4p-derived bands. This can explain in part the relatively weak splitting found in TaSe₂. The discrepancy between calculation and measurements for the magnitude of the Se 4p-derived band splitting can be explained by the introduction of SOC as a perturbative calculation in the Wien code.

Now we will show that the same conclusions about the origin of these splittings can be obtained with only few considerations using group theory. Group theory gives us tools to deduce some of the properties of the energy levels of electrons in the crystal without solving the corresponding

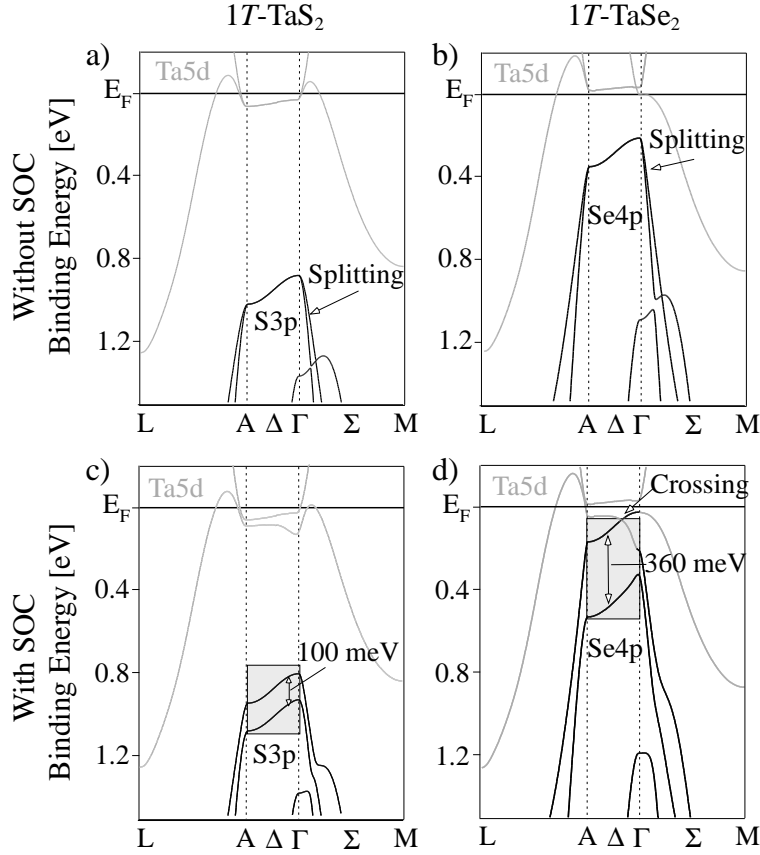


Figure 6.4: (a)-(d) Calculated band structures. In the calculations with SOC (c) and (d) the regions corresponding to Fig. 6.3 (a) and (b) are shaded in gray.

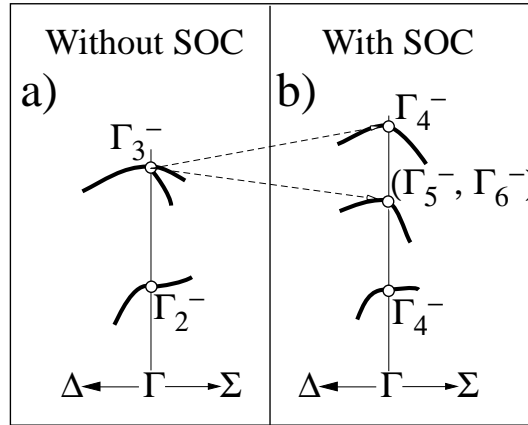


Figure 6.5: Schematic band structure obtained from group theory (see text).

Schrödinger equation. To understand how the symmetry properties of a solid help us to extract some information about the solutions of the Schrödinger equation $H\psi=E\psi$, we just give a short reminder below. Consider a set of degenerate solutions ψ_i^μ of the Schrödinger equation. We have $H\psi_i^\mu = E_\mu\psi_i^\mu$, for $i=1, \dots, n_\mu$. This set of eigenfunctions forms a function space associated with the eigenvalue E_μ . Now the key point, as H is invariant under all the transformation operators \mathfrak{R} corresponding to the symmetry operations R of the considered symmetry group ($[H, \mathfrak{R}] = 0$), $\mathfrak{R}\psi_j^\mu$ is also an eigenfunction of H with eigenvalue E_μ . It follows that $\mathfrak{R}\psi_j^\mu$ is a member of the function space for energy E_μ . We can then write $\mathfrak{R}\psi_j^\mu = \sum_{i=1}^{n_\mu} D_{ij}^\mu(R)\psi_i^\mu$, $j=1, \dots, n_\mu$. In this manner a

set of matrices $D^\mu(R)$ is built which is homomorphic with the symmetry group. This set of matrices forms a representation of the symmetry group and the linearly independent degenerate wavefunctions ψ_i^μ for energy level E_μ form a basis for the representation called Γ^μ . Since we know all the irreducible representations of the symmetry group we can deduce some information about the possible solutions of the Schrödinger equation. As a matter of fact each energy level corresponds to an irreducible representation and the dimension of this representation gives the degree of degeneracy of this level. How to build these irreducible representations without knowing the solutions ψ_i ? Group theory with the use of mathematical rules, allows to construct character tables of the symmetry group and to extract from these tables the properties of the irreducible representations. In the case of a crystal, all the symmetry information is contained in the space group which is, according to the international notation, $P\bar{3}m1$ for 1T-TaS₂ and 1T-TaSe₂. The tables for single and double groups (the ones necessary for SOC) of this space group are not displayed here but are available in reference [23]. To denote the representations of the group of vector \vec{k} we follow the notation of reference [23]. We assume that the p chalcogen valence bands are derived only from the three S and Se p_x, p_y, p_z orbitals. This is an approximation but we might expect that for \vec{k} vectors of high symmetry these orbitals give a reasonable description of the wave functions. First, we begin by neglecting the spin of the electron (study without SOC) and we restrict the study of the degeneracy to the three \vec{k} vectors Γ (centre of BZ), Δ (any intermediate point on the line Γ -A) and Σ (point along Γ -M). The results obtained from this study (without SOC) in the framework of the group theory are summarized in Fig. 6.5 (a) and, for the case with SOC, in Fig. 6.5 (b). The irreducible character table of the group of Γ [23] shows directly that the orbital p_z belongs to the irreducible representation Γ_2^- (1), where the number in parenthesis (i.e.(1)) indicates the dimension of the representation, and that the orbitals p_x and p_y form a basis of the irreducible representation Γ_3^- (2). Hence, there are two "bands" in Γ , one no-degenerate and one doubly degenerate. The use of the compatibility rule shows that the degeneracy stays the same along Δ but that the doubly degenerate Γ_3^- level is split along Σ in two no-degenerate states. This corresponds exactly to the behaviour observed in the calculations (Fig. 6.4 (a) and (b)) and confirms that the splitting along Γ -M is a consequence of the lowering of symmetry from Γ to Σ .

Now we observe the effect of introducing SOC. First we note that adding spin simply doubles the degeneracy of every state. But when SOC is turned on more dramatic changes in the bands can occur such as the lifting of degeneracies. If this is the case, inspection of the character table has to predict these effects. In terms of group theory, introduction of SOC implies that we have to work with the double groups introduced by Bethe [24]. In other words the eigenfunctions of the hamiltonian containing the SOC term ($H+H_{SOC}$) form a basis for the irreducible representations of the double group. To find these irreducible representations we proceed as follows. We start from the irreducible representations (Γ_{SG}) of the single group found in the previous study without SOC (i.e. for the k-point Γ : Γ_2^- (1) and Γ_3^- (2)). To each of these representations (Γ_{SG}) corresponds an irreducible representation (Γ_{DG}) of the double group which can be identified straightforwardly by comparing the characters. For the k-point Γ , the representation $\Gamma_{SG}=\Gamma_2^-$ induces the representation of the double group $\Gamma_{DG}=\Gamma_2^-$ and $\Gamma_{SG}=\Gamma_3^-$ induces $\Gamma_{DG}=\Gamma_3^-$. As we introduce the spin, the eigenfunctions are no more linear combinations of only the p_x, p_y, p_z orbitals but the product of these orbitals with the spin functions α and β . Thus we have to identify for which irreducible representation Γ_S (S for spin) of the considered double group the spin functions α and β form a basis. For the double group of the k-point Γ , $\Gamma_S=\Gamma_4^+$. Finally the irreducible representations of the double group for which the eigenfunctions of the hamiltonian $H+H_{SOC}$ form a basis result from the reduction (if necessary) of the representation obtained by the direct product $\Gamma_{DG} \otimes \Gamma_S$. For the k-point Γ we get the following : $\Gamma_2^- \otimes \Gamma_4^+ = \Gamma_4^-$ (2) and $\Gamma_3^- \otimes \Gamma_4^+ = \Gamma_5^-$ (1) + Γ_6^- (1) + Γ_4^-

(2)

These results show that the introduction of SOC doubles the degeneracy of the band Γ_2^- and splits the band Γ_3^- into two doubly degenerate bands. Indeed the representation Γ_5^- is the complex conjugate of the representation Γ_6^- and therefore they are degenerate by the time inversion symmetry. We use again the compatibility rule to show how the degeneracy evolves when moving from Γ to Σ or Δ . Along Σ SOC simply doubles the degeneracy of the three distinct bands and along Δ the behaviour is similar as at Γ . To summarise the most important effect of SOC is the splitting at Γ and Δ of the level Γ_3^- into two bands (Γ_5^-, Γ_6^-) and Γ_4^- . The origin of this SO splitting is even more clearly illustrated by calculating, using the projection method, the basis functions of these representations obtained from the six p orbitals (taking into account spin) and changing the basis in the more adapted JM_J basis (total angular momentum, projection of this angular momentum). This shows that the basis functions of $\Gamma_5^- + \Gamma_6^-$ are pure $J=3/2$ states, whereas the basis functions of Γ_4^- are a mixing of $J=1/2$ and $J=3/2$ states.

6.2.4 Conclusion

Our ARPES measurements exhibit a splitting of the chalcogen p-derived valence bands along the high symmetry directions Γ -M in 1T-TaS₂ and 1T-TaSe₂. Based on density functional theory calculations we attribute this splitting to the symmetry along Γ -M and to the SO interaction along Γ -A. The introduction of SOC has a considerable effect on the band structure, in particular, it splits the degenerate bands along the k_{\perp} direction (Γ -A) of the S-Se p-derived bands, the splitting along Γ -M being already reproduced by a non-relativistic calculation. For completeness and understanding we have studied the effect of SO within the framework of group theory. This has the advantage of describing the evolution of the degeneracies of the chalcogen bands which, for simplicity, are constructed purely from p orbitals. We note that although the SO interaction lifts one degeneracy, it still leaves all states doubly degenerated due to the presence of inversion symmetry. It is a well known fact that the SO interaction does not separate states of opposite spin if the lattice potential has a centre of inversion [8]. This is not the case at the crystal surface and, for example, it has been observed that SOC is responsible for a spin splitting of surface state bands leading to non-degenerate states. [3, 7] Finally, this study allows to identify a key difference between 1T-TaS₂ and 1T-TaSe₂, namely the strong mixing between the Ta 5d and Se 4p derived bands.

Acknowledgements

Skillful technical assistance was provided by O. Raetzo, E. Mooser, R. Schmid, O. Zosso, Ch. Neururer, and F. Bourqui. This project has been supported by the Fonds National Suisse de la Recherche Scientifique.

6.3 Complement

In this complement the reader will find the character tables of the space group $P\bar{3}m1$ used in the previous section as well as additional informations about group theory tools. Below the three single group character tables of the points and lines of symmetry Γ/A , Δ and Σ are represented as they can be build with help of ref. [23]. We recall here that the character $\chi^\mu(R)$ of the symmetry operation R in the representation Γ^μ is equal to the trace of the representative matrix of the operation R in the same representation Γ^μ , $\chi^\mu(R) = \sum_i D_{ii}^\mu(R)$.

Γ/A	E	$2C_3$	$3C_2$	I	$2S_6$	$3\sigma_v$
Γ_1^+	1	1	1	1	1	1
Γ_2^+	1	1	-1	1	1	-1
Γ_3^+	2	-1	0	2	-1	0
Γ_1^-	1	1	1	-1	-1	-1
Γ_2^-	1	1	-1	-1	-1	1 z
Γ_3^-	2	-1	0	2	1	0 (x,y)

$\Delta(\Gamma A)$	E	$2C_3$	$3\sigma_v$
Γ_1	1	1	1 z
Γ_2	1	1	-1
Γ_3	2	-1	0 (x,y)

$\Sigma(\Gamma M)$	E	σ_v
Γ_1	1	1 y,z
Γ_2	1	-1 x

The representations are labelled with the Γ notation introduced by Bouckaert, Smoluchowski and Wigner [25]. We note that these tables satisfy a certain number of rules: (i) the number of irreducible representations of a group is equal to the number of classes (number of rows = number of columns) (ii) the sum of the square of the dimension of the irreducible representation l_μ is equal to the number of symmetry operations of the group h , $\sum_\mu l_\mu^2 = h$ (iii) and the characters are orthogonal, this means that $\sum_R \chi^\mu(R) \chi^{\mu'}(R) = h \delta_{\mu\mu'}$. In the last column of the tables above, we mention only the basis functions or symmetry types related to the p-states since in the analysis of the previous section we consider only the p_x , p_y and p_z . This can be verified by the application on these functions p_x , p_y and p_z of the projection operator $P^\mu = (l_\mu/h) \sum_R \chi^\mu(R) R$, which generates basis functions. According to the first table of the point symmetry Γ/A , the orbital p_z belongs to the irreducible representation Γ_2^- of dimension one whereas the orbital p_x and p_y form a basis of the irreducible representation Γ_3^- of dimension two. The evolution along the lines of symmetry is dictated by the compatibility rule which says that the sum of the characters of the compatible representations along the line must be equal to the character of the representation of the end point of symmetry. This equality must hold for every class in common. For example in our case the representations of the line of symmetry Σ compatible with the representation Γ_3^- of the point of symmetry Γ/A are the representation Γ_1 and Γ_2 because $\chi^{\Gamma_3^-}(R) = \chi^{\Gamma_1}(R) + \chi^{\Gamma_2}(R)$ for $R = E$ and σ_v .

As mentioned in the previous section introduction of the SOC implies that we have to deal with the double group whose character tables are represented below for the points and lines of symmetry Γ/A , Δ and Σ .

6.3. Complement

Γ / A	E	\bar{E}	$2C_3$	$2\bar{C}_3$	$3C_2$	$3\bar{C}_2$	I	\bar{I}	$2S_6$	$2\bar{S}_6$	$3\sigma_v$	$3\bar{\sigma}_v$
Γ_1^+	1	1	1	1	1	1	1	1	1	1	1	1
Γ_2^+	1	1	1	1	-1	-1	1	1	1	1	-1	-1
Γ_3^+	2	2	-1	-1	0	0	2	2	-1	-1	0	0
Γ_4^+	2	-2	1	-1	0	0	2	-2	1	-1	0	0
Γ_5^+	1	-1	-1	1	i	-i	1	-1	-1	1	i	-i
Γ_6^+	1	-1	-1	1	-i	i	1	-1	-1	1	-i	i
Γ_1^-	1	1	1	1	1	1	-1	-1	-1	-1	-1	-1
Γ_2^-	1	1	1	1	-1	-1	-1	-1	-1	-1	1	1
Γ_3^-	2	2	-1	-1	0	0	-2	-2	1	1	0	0
Γ_4^-	2	-2	1	-1	0	0	-2	2	-1	1	0	0
Γ_5^-	1	-1	-1	1	i	-i	-1	1	1	-1	-i	i
Γ_6^-	1	-1	-1	1	-i	i	-1	1	1	-1	i	-i

$\Delta(\Gamma A)$	E	\bar{E}	$2C_3$	$2\bar{C}_3$	$3\sigma_v$	$3\bar{\sigma}_v$
Γ_1	1	1	1	1	1	1
Γ_2	1	1	1	1	-1	-1
Γ_3	2	2	-1	-1	0	0
Γ_4	2	-2	1	-1	0	0
Γ_5	1	-1	-1	1	i	-i
Γ_6	1	-1	-1	1	-i	i

$\Sigma(\Gamma M)$	E	\bar{E}	σ_v	$\bar{\sigma}_v$
Γ_1	1	1	1	1
Γ_2	1	1	-1	-1
Γ_3	1	-1	i	-i
Γ_4	1	-1	-i	i

The rules i), ii) and iii) described above for the single group are valid for the double group as well as the projection method to find the basis functions and the compatibility rule to deduce the evolution along the lines of symmetry.

References for chapter 6

- [1] E. O. Kane, J. Phys. Chem. Solids **1**, 82 (1956).
- [2] R. Braunstein and E. O. Kane, J. Phys. Chem. Solids **23**, 1423 (1962).
- [3] S. LaShell, B. A. McDougall and E. Jensen, Phys. Rev. Lett. **77**, 3419 (1996).
- [4] L. Petersen and P. Hedegard, Surf. Sci. **459**, 49 (2000).
- [5] G. Nicolay *et al.*, Phys. Rev. B **65**, 033407 (2002).
- [6] J. Henk, A. Ernst and P. Bruno, Phys. Rev. B **68**, 165416 (2003).
- [7] E. Rotenberg, J. W. Chung and S. D. Kevan, Phys. Rev. Lett. **82**, 4066 (1999).
- [8] J. M. Ziman, *Principles of the Theory of Solids* (Cambridge University Press, Cambridge, 1979).
- [9] J. A. Wilson, F. J. Di Salvo and J. Mahajan, Adv. Phys. **24**, 117 (1975).
- [10] N. V. Smith and M. M. Traum, Phys. Rev. B **11**, 2087 (1975).
- [11] K. Horiba *et al.*, Phys. Rev. B **66**, 073106 (2002).
- [12] M. Bovet *et al.*, Phys. Rev. B accepted.
- [13] P. Fazekas and E. Tossati, Phil. Mag. B **39**, 229 (1979).
- [14] L. P. Bouckaert, R. Smoluchowski and E. Wigner, Phys. Rev. **50**, 58 (1936).
- [15] S. L. Altmann, *Band theory of solids: an introduction from point of view of symmetry* (Oxford University Press, Oxford, 1994).
- [16] B. Dardel *et al.*, Phys. Rev. B **45**, 1462 (1992).
- [17] B. Dardel *et al.*, Phys. Rev. B **46**, 7407 (1992).
- [18] Blaha P, Schwarz K and Luitz J *WIEN97 A Full Potential Linearized Augmented Plan Wave Package for Calculating Crystal Properties (Karlheinz Schwarz, Techn. Universitt Wien, Austria), 1999. ISBN 3-9501031-0-4*
- [19] J. P. Perdew, S. Burke and M. Ernzerhof, Phys. Rev. Lett. **77**, 3865 (1996).
- [20] D. Singh, *Plane waves, pseudopotentials and the LAPW method* (Kluwer Academic, Dordrecht, 1994).
- [21] F. Herman and S. Skillman, *Atomic Structure Calculations* (Prentice-Hall, Englewood Cliffs NJ, 1963)
- [22] M. Cardona and N. E. Christensen, Solid State Commun. **116**, 421 (2000).
- [23] C. J. Bradley and A. P. Cracknell, 1972 *The Mathematical Theory of Symmetry in Solids* (Clarendon Press, Oxford, 1972).
- [24] H. A. Bethe, Annln Phys. **3** 133-208 (1929)

6.3. References for chapter 6

- [25] L. P. Bouckaert, R. Smoluchowski and E. Wigner, *Phys. Rev* **50**, 58 (1936).
-

Chapter 7

Conclusion

This thesis is principally devoted to the high resolution ARPES study of CDW occurring in quasi-2D TMDCs compounds, particularly in $1T$ -TaS₂ and $1T$ -TiSe₂. Our main conclusion is that the standard Peierls scenario is not sufficient to explain the CDW instability and that a renewed glance on complex correlations is therefore needed for understanding this class of materials. The occurrence of CDW in the two samples measured during this thesis can be explained by two different scenarios: the measured $1T$ -TaS₂ spectra can be analyzed in the frame of electron-phonon interaction, with the introduction of polarons, while the spectra measured for $1T$ -TiSe₂ are compatible with the presence of excitons, which reflect the electron-hole interaction. We are fully aware that these scenarios are maybe only part of the truth; nevertheless this study shows that it is necessary to consider alternative scenarios to the widespread Peierls model.

After looking at these results two more general remarks are worth being made: first the ARPES tool has now become so powerful in terms of energy and angular resolution (as well as on flexibility thanks to the development of modern synchrotrons), that very detailed spectral information can be obtained. However, in some cases the interpretation of the data is hampered by misunderstood intensity variations, illustrating the necessity for a refined theoretical investigation of the photoemission process and notably of the influence of matrix elements. Second, the complexity of quasi-2D systems points out once more the need for combining different methods to investigate solid state materials. For a full understanding of the electronic structure it appears more and more that material inhomogeneities such as structural defects or local doping have to be taken into account. Therefore, a tool like STM appears as an essential instrument complementary to the ARPES tool.

Remerciements

Il est temps de remercier toutes les personnes qui m'ont soutenu tout au long de mon travail de thèse, que ce soit en pensée ou en action.

Avant tout je remercie mon superviseur de thèse, le Prof. Philipp Aebi, qui m'a initié aux joies de la photoémission. Je lui suis très reconnaissant tant pour son suivi scientifique que pour ses qualités humaines.

Je remercie également les membres du jury, Hans Beck, Daniel Malterre et Luc Patthey pour avoir accepté de juger mon travail et ainsi de me consacrer une partie de leur temps.

Je voudrait remercier encore plus particulièrement le Prof. Hans Beck, sans qui le monde des excitons serait resté un mystère pour moi. Je lui dois notamment la partie théorique du chapitre 5.

Un grand merci bien sûr à tous les membres du groupe " 10^{-11} ". Notamment, notre cher maître assistant, Gunnar Garnier, dont j'ai pu apprécier les multiples compétences. Laurent Despont avec qui j'ai eu le plaisir de partager de nombreux moments de bonne humeur et de détente. Corsin Battaglia, Hervé Cercellier et Claude Monney qui tous contribuent quotidiennement à une excellente atmosphère de travail. Je ne voudrais évidemment pas oublier les anciens du groupe, Marc Bovet, Christian Koitzsch, Oliver Gallus et Pavel Starowicz.

Encore une fois merci à Gunnar pour sa lecture attentive du manuscrit et ses précieuses corrections.

Merci aux membres des ateliers de mécanique et d'électronique, leurs compétences et disponibilité furent d'une aide inestimable au développement et au maintien de nos infrastructures. Je joins à ces remerciements Francis Bourqui pour le développement du programme d'acquisition ainsi que pour son initiation à la programmation orientée objet.

Merci à l'administration et au secrétariat qui veillent à la bonne marche de l'institut.

Merci à ma famille source d'un intarissable bonheur. A mes parents qui, sans jamais me pousser, ont su comme une main invisible me guider jusqu'ici. Et enfin, à toi Marjorie, pour tout...

Curriculum vitae

Personal details

Family name	Clerc
First name	Florian
Date of birth	March 19, 1977
Place of birth	Fribourg, Switzerland
Citizen of	Corpataux FR
Marital status	single

Studies

1992 - 1996	High school in Fribourg, Collège Sainte-Croix Baccalauréat et maturité fédérale, type C (scientifique)
1996 - 1997	Studies in geology, Université de Fribourg
1997 - 2001	Studies in physics, Université de Fribourg
2001 - 2002	Diploma work in solid state physics “Multicouches de C_{60} déposées sur Cu(111)” under the direction of Prof. Ph. Aebi
since 2002	Ph.D. student in solid state physics, Université de Neuchâtel
since 2004	Master of advanced studies in energy, EPFL lausanne

List of Publications

- **Growth of thin Bi films on W(100)**
C. Koitzsch, M. Bovet, F. Clerc, Naumović, L. Schlapbach, P. Aebi, *Surf. Sci.* **527**, 51-56 (2003).
- **Pseudogapped Fermi surfaces of 1T-TaS₂ and 1T-TaSe₂: a charge density wave effect**
M. Bovet, D. Popović, F. Clerc, C. Koitzsch, U. Probst, E. Bucher, H. Berger, D. Naumović, P. Aebi, *Phys. Rev. B* **69**, 125117 (2004)
- **Fermi Surface Topology of Rare Earth Dihydrides**
C. Koitzsch, J. Hayoz, M. Bovet, F. Clerc, L. Despont, C. Ambrosch-Draxl, P. Aebi, *Phys. Rev. B* **70**, 165114 (2004)
- **Excited states mapping by secondary photoemission**
M. Bovet, V. N. Strocov, F. Clerc, C. Koitzsch, D. Naumović, P. Aebi, *Phys. Rev. Lett.* **93**, 107601 (2004)

- **Spin-orbit splitting in the valence bands of 1T-TaS₂ and 1T-TaSe₂**
 F. Clerc, M. Bovet, H. Berger, L. Despont, C. Koitzsch, O. Gallus, L. Patthey, M. Shi, J. Krempaski, M. G. Garnier, P. Aebi, *J. of Physics C* **16**, 3271-3278 (2004)
- **Charge density waves in 1T-TaS₂: An angle-resolved photoemission study**
 F. Clerc, M. Bovet, H. Berger, L. Despont, C. Koitzsch, M. G. Garnier, P. Aebi, *Physica B* **351**, 245-249 (2004)
- **Fermi surface induced lattice distortion in NbTe₂**
 C. Battaglia, H. Cercellier, F. Clerc, L. Despont, M. G. Garnier, C. Koitzsch, H. Berger, L. Forró, C. Ambrosch-Draxl, P. Aebi, *Phys. Rev. B* **72**, 195114 (2005)
- **Photoemission of a Quantum Cavity with a Nonmagnetic Spin Separator**
 C. Koitzsch, C. Battaglia, F. Clerc, L. Despont, M. G. Garnier, P. Aebi, *Phys. Rev. Lett.* **95**, 126401 (2005)
- **Direct evidence for ferroelectric polar distortion in ultrathin lead titanate perovskite films**
 L. Despont, C. Lichtensteiger, C. Koitzsch, F. Clerc, M. G. Garnier, F. J. Garcia de Abajo, E. Bousquet, Ph. Ghosez, J.-M. Triscone, P. Aebi, *Phys. Rev. B* **73**, 094110 (2006)
- **X-ray photoelectron diffraction study of Cu(111): Multiple scattering investigation**
 L. Despont, D. Naumović, F. Clerc, C. Koitzsch, M. G. Garnier, F. J. Garcia de Abajo, M. A. Van Hove, P. Aebi, *Surf. Sci.* **600**, 380-385 (2006)
- **X-ray photoelectron diffraction study of ultrathin PbTiO₃**
 L. Despont, C. Lichtensteiger, F. Clerc, M. G. Garnier, F. J. Garcia de Abajo, M. A. Van Hove, J.-M. Triscone, P. Aebi, *Eur. Phys. J. B* **49**, 141-146 (2006)
- **Lattice-distortion enhanced electron-phonon coupling and Fermi surface nesting in 1T-TaS₂**
 F. Clerc, C. Battaglia, M. Bovet, L. Despont, C. Monney, H. Cercellier, M. G. Garnier, H. Berger, L. Forró, P. Aebi, *Phys. Rev. B*, submitted (2006)
- **Fermi surface of layered compounds and bulk charge density wave systems**
 F. Clerc, C. Battaglia, C. Monney, H. Berger, L. Despont, M. G. Garnier, P. Aebi, *J. Phys. C*, submitted (2006)